GEOMAR
Helmholtz Centre for Ocean Research Kiel

Southern Annular Mode response to volcanic eruptions in the MPI-ESM

Master Thesis of Stephanie Gleixner

June 24, 2012

Faculty of Mathematics and Natural Sciences
Christian-Albrechts-University, Kiel
-Maritime Meteorology-

Abstract

Large explosive volcanic eruptions represent a natural external forcing on climate with the strongest direct radiative impact in the stratosphere. This study examines the indirect circulation response to such eruptions in the Southern Hemisphere (SH), by analyzing the Southern Annular Mode (SAM) in ERA-40 reanalysis data and the simulation ensemble of the CMIP5 historical experiment of the Max-Planck Institute Earth System Model (MPI-ESM). In contrast to earlier modeling studies on the volcanic impact on SAM, this high-top coupled atmosphere-ocean model has a well resolved stratosphere and mesosphere. The CMIP5 historical experiment are hindcasts, which include observed anthropogenic and natural forcing.

A surface SAM based on sea level pressure and a stratospheric SAM based on geopotential height at 50hPa are defined using EOF analysis. The SAM response to 10 volcanic eruptions with global aerosol optical depth (AOD) of more than 0.02 within the time period of 1850 to 2000 is investigated in three ensemble simulations, while only the latest 5 eruptions are covered by the ERA-40 data. For hemispheric comparison, Northern Annular Mode (NAM) after volcanic eruptions is also examined.

A comparison of temperature and wind climatologies and their seasonal evolution showed good agreement between MPI-ESM and ERA-40. The first spatial EOF pattern at the surface and in the stratosphere in the SH, which the SAM indices are based on, also agree well between the model and the reanalysis data. The MPI-ESM CMIP5 historical runs successfully captured the observed positive SAM trend reported in previous publications.

As a case study temperature changes after the eruption of Mount Pinatubo are analyzed. Model and reanalysis both show a warming of the lower stratosphere in the subtropical latitudes due to the increased aerosol loading. In contrast to the MPI-ESM, in the reanalysis the warming of the equatorial stratosphere is delayed by approximately one year due to the easterly phase of the Quasi-biennial Oscillation (QBO). The surface cooling is stronger in the MPI-ESM than in ERA-40.

In general, it is difficult to identify volcanic signals in the annular modes due to their strong unforced variability. In the reanalysis data a shift to a negative stratospheric SAM can be found after all 5 eruptions except for Agung, but only after the eruption of Fuego and Mount Pinatubo these changes are significant. In the first winter after all eruptions the surface SAM is negative, leading to a significantly negative SAM in the composite mean. These "observed" SAM changes are in sharp contrast to the simulated SAM changes. A significant positive stratospheric SAM is found in the SH spring seasons after the eruptions of El Chichon in 1982 and Mount Pinatubo in 1991. These two eruptions showed the largest AOD forcing in the 20^{th} century and the SAM responses to these eruptions in the MPI-ESM integrations support findings of previous modeling studies. Composites of post-volcanic SAM changes with regard to the strength of the eruptions' AOD signals highlight the fact, that only the composite mean of the strongest eruptions considered in this study evoke a significant SAM response. There is no significant surface SAM response after the eruptions in the MPI-ESM.

In the Northern Hemisphere (NH), the positive NAM responses to large volcanic eruptions, that have been found in reanalysis data in previous publications, are strongly underestimated in the ERA-40 results in this study. The NAM is positive in the first winter after 4 of the 5 observed eruptions, but the signals are not significant. This result highlights the sensitivity

of volcanic response studies to the anomaly calculation. In contrast to the SH, in the NH no significant volcanic impact on the annular mode can be detected in the MPI-ESM CMIP5 historical runs.

Overall, the findings about the simulated SAM response to large volcanic eruptions of this study are very similar to previous modeling studies, suggesting that the inability of models to simulate observed annular mode changes after volcanic eruptions is not only due to an insufficiently resolved model stratosphere. The eruptions considered in this study are likely to be too weak to cause extra-tropical circulation changes that exceed unforced variability. The differences between ERA-40 and MPI-ESM results are assumed to be due to non-volcanic forcing terms, since the MPI-ESM CMIP5 historical experiment runs do not include the observed El Niño/Southern Oscillation (ENSO) phases, QBO or inter-annual ozone variability. These effects need to be investigated in future studies.

Zusammenfassung

Starke, explosive Vulkanausbrüche stellen einen natürlichen, externen Antrieb des Klimas dar. Den stärksten direkten Strahlungseffekt haben sie in der Stratosphäre. In dieser Studie wird der indirekte Einfluss solcher Vulkanausbrüche auf die Zirkulation auf der Südhemisphäre (SH) untersucht, indem der Southern Annular Mode (SAM) in ERA-40 Reanalysedaten und in dem Simulationsensemble des CMIP5 historical experiment des Max-Planck Institute Earth System Model (MPI-ESM). Im Gegensatz zu bisherigen Modellstudien zum vulkanischen Einfluss auf SAM hat dieses gekoppelte Ozean-Atmosphären Modell mit High-Top eine hoch aufgelöste Stratosphäre und Mesosphäre. Das CMIP5 historische Experiment sind historische Simulationen, die beobachtete anthropogene und natürliche Antriebe beinhalten.

Ein Boden-SAM, der auf Druck auf Meeresspiegelhöhe basiert, und ein stratosphärischer SAM, der auf geopotentieller Höhe auf 50 hPa basiert, werden mittels der EOF-Analyse definiert. Die SAM-Reaktion auf 10 Vulkanausbrüche mit einer globalen, durch Aerosole getrübten, optischen Dicke (AOD) von mehr als 0.2 im Zeitraum von 1850 bis 2000 wird in drei Ensembleläufen untersucht, während nur die letzten 5 von den ERA-40 Daten abgedeckt werden. Zum Vergleich der Hemisphären wird auch der Northern Annular Mode (NAM) nach Vulkanausbrüchen untersucht.

Ein Vergleich der Temperatur- und Windklimatologien und deren saisonaler Entwicklung zeigt eine gute Übereinstimmung zwischen MPI-ESM und ERA-40. Auch die ersten räumlichen EOF Muster auf der SH am Boden und in der Stratosphäre, auf welchen die SAM Indizes basieren, stimmen gut zwischen Modell und Reanalyse überein. Die MPI-ESM Läufe des CMIP5 historischen Experiments haben den beobachteten positiven SAM Trend, der in früheren Veröffentlichungen gezeigt wurde, erfolgreich erfasst.

Als Fallbeispiel wurden Temperaturveränderungen nach dem Ausbruch des Mount Pinatubo im Juni 1991 analysiert. Modell und Reanalyse weisen beide eine Erwärmung der unteren Stratosphäre in subtropischen Breiten aufgrund erhöhter Aerosolbelastung auf. Im Gegensatz zum MPI-ESM ist die Erwärmung der äquatorialen Stratosphäre in den Reanalysedaten aufgrund der Ostphase der quasi-zweijährigen Schwingung (QBO) um ungefähr ein Jahr verzögert. Die Abkühlung der Bodentemperatur ist im MPI-ESM stärker als in ERA-40.

Es ist allgemein schwierig vulkanische Signale in den Annularen Modi zu identifizieren, da deren natürliche Variabilität stark ist. In den Reanalysedaten findet man eine Verschiebung zu negativem Stratosphären-SAM nach allen 5 Vulkanausbrüchen außer Agung. Nur nach den Ausbrüchen von Fuego und Mount Pinatubo sind diese Veränderungen signifikant. Im ersten Winter nach allen Ausbrüchen ist der Boden-SAM negativ, was zu einem signifikant negativen Boden-SAM führt, wenn man das Mittel der Ausbrüche betrachtet. Diese "beobachteten" SAM-Veränderungen stehen in starkem Kontrast zu den simulierten SAM-Veränderungen. Es wurden signifikant positive stratosphärische SAM-Indizes im SH Frühling nach den Ausbrüchen von El Chichon, 1982, und Mount Pinatubo, 1991, gefunden. Diese beiden Ausbrüche weisen das stärkste AOD-Signal im 20. Jahrhundert auf und die SAM-Reaktionen auf diese Ausbrüche in den MPI-ESM Simulationen bestätigen die Ergebnisse früherer Modellstudien. Gemittelte SAM-Veränderungen nach Vulkanausbrüchen, sortiert nach der Stärke der AOD-Signale, unterstreichen die Tatsache, dass nur das Mittel der stärksten der in dieser Studie berücksichtigten Ausbrüche eine signifikante SAM-Reaktion hervorruft. In den MPI-ESM

Integrationen gibt es keine signifikanten SAM-Reaktionen auf die Vulkanausbrüche auf dem Boden.

In der NH werden die positiven NAM-Reaktionen auf starke Vulkanausbrüche, die in früheren Studien in Reanalysedaten gefunden wurden, in den ERA-40 Ergebnissen dieser Studie stark unterschätzt. Der NAM ist nach 4 der 5 Ausbrüche im folgenden Winter positiv, aber die Signale sind nicht signifikant. Dieses Ergebnis betont die Abhängigkeit von Studien über Vulkaneffekte von der Berechnungsmethode der Anomalien. Im Gegensatz zur SH kann auf der NH kein signifikanter Einfluss von Vulkanausbrüchen auf den Annular Mode in den MPI-ESM Simulationen gefunden werden.

Allegemein ähneln die Ergebnisse dieser Studie zu den simulierten SAM Veränderungen nach starken Vulkanausbrüchen früheren Modellstudien. Das weist darauf hin, das die Unfähigkeit von Modellen, beoachtete Veränderungen der Annular Modes nach Vulkanausbrüchen zu simulieren, nicht alleine an einer ungenügend hochaufgelöste Stratosphäre liegt. Die Vulkanausbrüche, die in dieser Studie betrachtet werden, sind wahrscheinlich zu schwach um Signale in der extra-tropischen Zirkulation hervorzurufen, die stärker als die Schwankungen ohne vulkanischen Einfluss sind. Die Unterschiede zwischen ERA-40 und MPI-ESM sind vermutlich auf nicht-vulkanische Antriebsterme zurückzuführen, da die MPI-ESM historical experiment Läufe weder die beobachteten El Niño/Southern Oscillation (ENSO) Phasen, noch die QBO oder beobachtete inter-annuale Ozonvariabilität beinhalten. Diese Effekte müssten in zukünftigen Studien untersucht werden.

Contents

Chapter 1

Introduction

The Earth's climate system is a complex and chaotic system with strong internal variability. The natural variability of the subsystem atmosphere is influenced by numerous factors as solar forcing, oceanic forcing like the coupled atmosphere-ocean oscillation pattern El Niño/Southern Oscillation (ENSO) or even geological forcing like volcanic eruptions.

Large, explosive volcanic eruptions disturb the radiative balance of the Earth's atmosphere. Their sulfur injections into the stratosphere lead to enhanced absorption of radiation and thus heating at layer and have a global cooling effect on the surface on timescales of up to 3 years (Robock and Mao, 1995; Robock, 2000; Hegerl et al., 2003). In addition to those direct radiative effects, volcanic eruptions can have an indirect dynamical effect on the atmosphere. The question of how these radiative changes affect the circulation in the atmosphere is still under investigation and is addressed in this study.

During all seasons, the variability of the Southern Hemisphere (SH) extra-tropical circulation is dominated by a mass see saw between the mid-latitudes and the polar cap. The corresponding, approximately zonally symmetric fluctuation pattern in surface pressure has been labeled Antarctic Oscillation (Gong and Wang, 1999) or Southern Annular Mode (SAM) (Thompson and Wallace, 2000) with regard to an equivalent mode in the Northern Hemisphere (NH). Similarly structured variability of the zonal wind and geopotential height dominate the variability of these fields throughout the whole SH troposphere and stratosphere on intra-seasonal to inter-annual time scales (Kidson, 1988; Hartmann and Lo, 1998; Karoly, 1990; Thompson and Wallace, 2000). A positive SAM is defined as an equator-ward shift of the atmospheric mass and a corresponding strengthening of the mid-latitude westerlies.

SAM variability is mostly the result of internal or unforced variability of the atmosphere-ocean system, but a contribution of volcanic forcing has been assumed. An example is the negative peak in the surface SAM in 1964, which has been attributed to the eruption of Agung (Marshall, 2003). Roscoe and Haigh (2007) regressed an observational SAM index to a volcanic aerosol index from 1957 to 2005 and found an anti-correlation of the two indices, which states that volcanic eruptions are mostly occurring simultaneously to a negative SAM phase. Crooks and Gray (2005) tried to isolate the volcanic signal in zonal wind in ERA-40 reanalysis after the eruptions of El Chichon (1982) and Mount Pinatubo (1991). They found a significant weakening of the tropospheric mid-latitude westerlies, which corresponds to a negative SAM anomaly. However, they emphasized the possible interference of volcanic signals with effects of the Quasi-Biennial Oscillation (QBO). Robock et al. (2007) examined

SH circulation anomalies in the SH winter seasons after the eruption of Mount Pinatubo in NCEP/NCAR reanalysis data. They also found a slightly negative SAM in the seasons following the eruption. However, the signal was not significant and the observed pressure pattern has been related to the simultaneously occurring El Niño. These studies illustrate the difficulty of relating post-volcanic SAM changes to the influence of volcanic aerosols.

Although present-day climate models have successfully simulated the perturbed radiative forcing following volcanic eruptions, climate models have failed to reproduce observed conditions of the SAM after volcanic eruptions. Robock et al. (2007) simulated the SH circulation response to the eruption of Mount Pinatubo using the model of Goddard Institute for Space Studies (GISS). They found no volcanic signal in the stratospheric or surface circulation. Karpechko et al. (2010) expanded the investigation of SH circulation responses to volcanic eruptions in climate models to an ensemble of 9 coupled ocean-atmosphere models that are part of the World Climate Research Programme's Coupled Model Intercomparison Project phase 3 (CMIP3). In contrast to the observed volcanic responses, the models simulated a significantly strong stratospheric vortex and negative surface pressure anomalies in the polar cap, i.e. a positive SAM, in spring and autumn following the eruptions of El Chichon and Mount Pinatubo.

The strongest radiative effects of volcanic aerosols in the atmosphere are found in the stratosphere. Therefore the reasons for the discrepancies between observed and simulated SAM conditions might be related to insufficient representation of stratospheric mechanisms in many models. Although the GISS model includes the complete vertical extend of the stratosphere, the vertical resolution is somewhat coarse with only 18 layers between the surface and 0.1 hPa (approximately 65 km altitude). In addition, the study by Robock et al. (2007) only examined SH winter conditions. The CMIP3 models include both high-top and low-top models of various resolution, but only few of them have a highly resolved stratosphere.

In contrast to the SH, the response of the Northern Hemisphere (NH) circulation to volcanic eruptions has been studied extensively. A significantly high positive phase of the Northern annular mode (NAM) has been observed for one to two years following volcanic eruptions (Stenchikov et al., 2002; Christiansen, 2008). The NH tropospheric circulation changes after volcanic eruptions can also be observed in the surface temperature pattern in winter. In contrast to the global mean surface cooling observed after volcanic eruptions, the so-called "winter warming" pattern shows warm anomalies over the NH continents during winter and has been linked to a strengthening of the mid-latitude westerlies, i.e. a positive NAM (Groisman, 1992; Robock and Mao, 1995; Robock, 2000, Fischer et al., 2007). The post-volcanic positive surface NAM has been related to a strong polar vortex (Perlwitz and Graf, 1995, Kodera and Koide, 1997), which has been found in reanalysis data (Stenchikov et al., 2002, 2006, Graf et al., 2007). As in the SH, reproducing the observed NH circulation changes with climate models poses a big challenge and models tend to underestimate the NAM response to volcanic forcing. Stenchikov et al. (2006) used the CMIP3 model simulations to analyze the NH circulation response after 9 volcanic eruptions in the 19^{th} and 20^{th} century and found no agreement between the models and observations. However, some model studies have successfully simulated a strengthening of the polar vortex due to volcanic forcing and the winter warming at the surface (Stenchikov et al., 2002; Shindell et al. 2004). Shindell at al. (2004) claim that only models with a high vertical resolution in the middle atmosphere are able to capture the effects that produce the positive NAM response to volcanic eruptions.

To test this hypothesis, a state-of the art high-top coupled ocean-atmosphere model with a highly resolved stratosphere is used to study the volcanic impact on the extra-tropical circulation. The Max-Planck-Institute Earth System Model (MPI-ESM) belongs to the generation of CMIP5 models, the follow-up project to CMIP3. The main questions addressed in this study are: 1.) Is this model with a high vertical resolution in the stratosphere able to simulate the observed SAM variability following volcanic eruptions? 2.) Did the model performance regarding this response improve compared to earlier model studies? 3.) Is there a comparable effect of volcanic eruptions on the annular modes on the two hemispheres.

This work is structured as followed. Chapter 2 provides information about the physical basis to understand the atmospheric processes after volcanic eruptions, describing the general circulation in the atmosphere and theoretical aspects of the volcanic forcing. The data and methods used in this study are described in chapter 3. Chapter 4 shows the results, starting with an evaluation of the model climatology. In the second part of chapter 4, the actual SAM response to volcanic eruptions and a comparison between SH and NH responses is shown. In chapter 5, the most important results are discussed and possible non-volcanic effects that interfere with volcanic signals are addressed.

Chapter 2

Fundamentals

2.1 Radiation

The main driver for motion of the atmosphere lies in the uneven distribution of the Earth's heat budget, due different radiative forcing. Heat is a form of energy and the exchange between the terrestrial system and space takes place via the spreading of spectrum of electromagnetic waves (radiation).

To understand radiative processes in the atmosphere, the basic laws of radiation should be kept in mind:

Every body with a temperature higher than 0 Kelvin emits radiation. The expansion of the Stefan-Boltzmann law to gray bodies states that the power of the emitted energy P depends on the body's surface temperature T, its emissivity ε, and the Stefan-Boltzmann constant σ ($\sigma = 5.67 \cdot 10^{-8} \frac{\mathrm{W}}{\mathrm{m^2 K^4}}$):

$$P = \sigma \varepsilon T^4 \tag{2.1}$$

All bodies radiate energy of different wavelengths, but which wavelength holds the biggest fraction of power of the emitted spectrum is solely dependent on temperature. Wien's displacement law shows an indirect proportionality between surface temperature T and the wavelength of maximal radiation λ:

$$\lambda_{max} = \frac{b}{T} \tag{2.2}$$

b is the Wien-constant and has a value of $2,8977721 \cdot 10^{-3} \mathrm{m} \cdot \mathrm{K}$.

The hot sun (mean temperature of 5777 Kelvin) emits maximal power at small wavelengths (visible and ultraviolet), while the considerably cooler earth (mean surface temperature of 287 Kelvin) emits a higher fraction of long-wave radiation (infrared). Therefore the Earth's system gains energy via solar short-wave radiation and loses it through outgoing long-wave radiation.

On the global average, these two terms are approximately in balance, but regionally those two terms show a large variety.

Solar radiation provides energy input into the system. There is a strong meridional gradient in its strength, since the amount of energy reaching a surface is a function of the angle between the incoming solar radiation and the surface (projection effect). Therefore the polar regions gain much less energy on annual average, while the tropics are strongly heated. Also of great

importance is the transparency of the atmosphere. Clouds, small floating particles (aerosols) and gases reflect, scatter or absorb solar radiation, which results in a cooling of the surface. In higher atmospheric layers absorption of sunlight by gases and aerosols has a heating effect (details in sections 2.2 and 2.5).

The planet's surface heat loss follows the Stefan-Boltzmann law. Due to the strong temperature dependence more thermal energy is emitted in warm tropical regions, while emission is lower in the much colder polar regions. Only a fraction of this terrestrial radiation leaves the system directly. So-called greenhouse gases (GHG) interact strongly with the long-wave radiation and absorb a large part of it, heating the atmosphere. The most abundant GHGs in the Earth's atmosphere are water vapor, carbon dioxide, methane, nitrous oxide, and ozone. Following equation (2.1) this energy is emitted again, partly into space, partly back to the surface. Since water vapor is one of the most dominant GHGs, energy loss via long-wave radiation is smallest in areas of high evaporation, which are the tropics due to the sea surface temperatures (SST).

The meridional dependence of solar radiation is higher than that of outgoing long-wave radiation (see figure 2.1). Therefore there is an overall heat gain in the lower latitudes and a heat loss in polar regions. The resulting horizontal temperature gradients and related pressure gradients drive horizontal and vertical motion in the atmosphere at the surface as well as in higher layers.

Vertical temperature gradients due to differences in the heating rates are the reason the layering of the atmosphere.

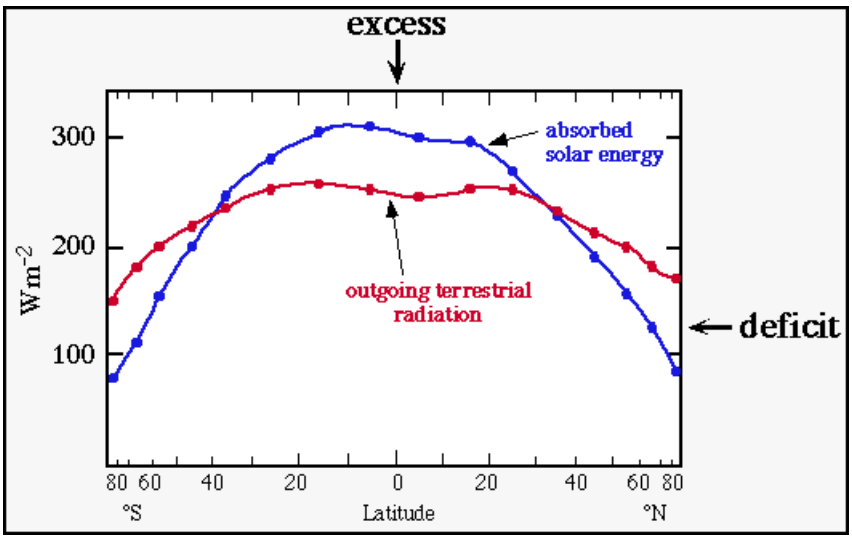

Figure 2.1: The annual mean, average around latitude circles, of the balance between the solar radiation absorbed at the ground (in blue) and the outgoing infrared radiation from Earth into space (in red). Source: Kushnir (2000)

2.2 Structure of the Atmosphere

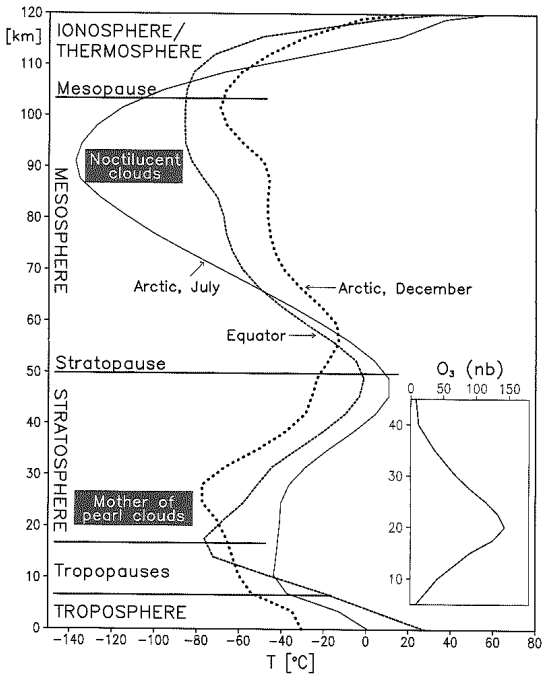

Figure 2.2: Temperature profile of the atmosphere under consideration of season and latitude. The vertical distribution of ozone (nb) at 50 °N is shown on the lower right-hand of the figure. (Labitzke and van Loon, 1999).

The Earth's atmosphere consists of different layers, which are defined by the vertical temperature profile (figure 2.2). In the layer closest to the Earth's surface, the troposphere, temperature decreases with increasing height. The coldest temperature are reached in altitudes of 6 to 18 km, depending on latitude and season. They mark the tropopause, which is the boundary layer between the troposphere and the stratosphere above. In the stratosphere temperature increases with height. It has an approximate vertical extent of 35 km and is confined by the stratopause in 50-60 km height. Above the stratopause, in the mesosphere, the vertical temperature gradient is reversed again.

Volcanic eruptions can provide dust and aerosol input in the two lowest layers of the atmosphere, the troposphere and stratosphere. To understand the climatic impact of volcanic eruptions the average state of those atmospheric layers is described in more detail.

2.2.1 Troposphere

The troposphere is the most dynamic layer, since the heating of the surface by the sun causes turbulence and convection. The troposphere is the the weather sphere. Processes in this layer have a direct influence on human life. The vertical temperature gradient in the troposphere is the result of radiative heating of the surface and convective processes. Upward motion of air masses needs energy to overcome gravitation. This energy is available in form of heat. Thus convection results in adiabatic (no heat exchange between air parcel and surroundings) cooling of the ascending air. The intensity of the upward motion depends on the heat energy of the air masses and therefore on the surface temperatures. Near the equator high surface temperatures cause an band strong convection, called inner-tropical convergence zone (ITCZ), which pushes the tropopause to maximal heights. Since the resulting adiabatic heating is also strongest in

these regions, the tropopause is coldest in the tropics. In higher latitudes tropopause heigth is lower, minimal altitudes are found at the pole of the winter hemisphere.

2.2.2 Stratosphere

Above the tropopause conditions are considerably calmer, due to the dynamically stable stratification in the stratosphere with warmer layers above cooler layers. The reason for the positive vertical temperature gradient in the stratosphere can be found in the ozone concentrations. The stratosphere has the highest ozone content in the atmosphere, with maximum concentrations in approximately 20-25 km altitude (figure 2.2). Ozone molecules interact strongly with solar radiation in the ultra-violet spectral range. Absorption of UV-radiation by ozone in the stratosphere heats the air masses in this layer, while it prevents a large fraction of the UV-radiation from reaching the surface.

Since volcanic aerosols have an impact on ozone chemistry, the basic principles of ozone depletion are described. Under non-volcanic conditions, the splitting of ozone molecules is limited to the polar stratosphere. This is due to the nature of the chemical processes that break up ozone molecules. Ozone is mostly depleted by a series of catalytic reactions with chlorine and bromine radicals. Figure 2.3 illustrates the example of chlorine. To finally react with ozone molecules, chlorine has to undergo a series of chemical reactions, of which the first takes place at the surface of polar stratospheric clouds (2). Since the stratosphere has very low water vapor concentrations, such clouds can only form under the extremely cold conditions in the polar night (1). The next series of reactions are photochemical, forming chlorine monoxide radicals (ClO_x) (3). Therefore the actual ozone depletion takes place in spring, when sunlight returns to polar latitudes. The ClO_x drives a catalytic ozone destruction cycle (4), which leads to high ozone depletion rates and thereby has a cooling effect on the polar stratosphere in spring.

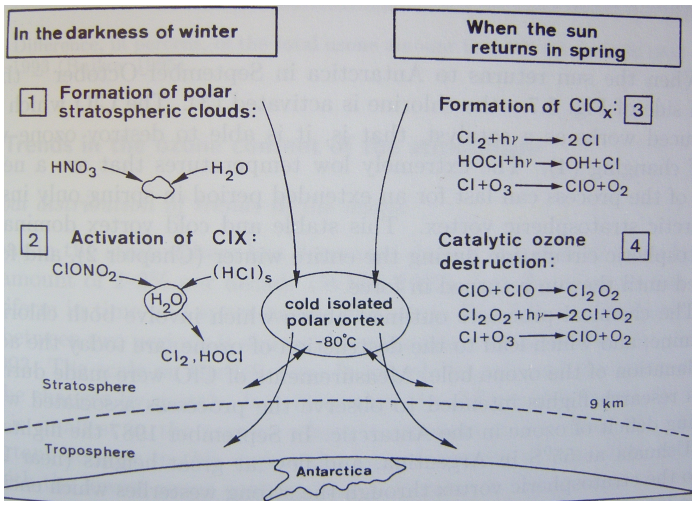

Figure 2.3: Illustration of the chemistry of ozone depletion in the Antarctic stratosphere (Enquete Kommission, 1992)

2.3 Atmospheric circulation

The described temperature conditions are the source of the mean atmospheric circulation. As already mentioned, the motion of the atmosphere is driven by the horizontal temperature gradients. The most important concepts to understand the mean circulation in the troposphere and stratosphere are geostrophic and thermal wind.

2.3.1 Geostrophic and thermal wind

Geostrophy is an idealized concept of atmospheric and oceanic dynamics. It describes the balance between two forces: One is the force that results from horizontal pressure gradients and acts from high to low pressure. It is proportional to horizontal pressure gradient, which is equivalent to the slope of surfaces of constant pressure. The second is the Coriolis force, which act only on bodies (or air masses) in rotating systems. It is proportional to the body's velocity and perpendicular to the rotation axes of the system and the movement. The flow that is described by the geostrophic balance is the geostrophic wind v_g and defined as:

$$v_g = \frac{1}{fg}\frac{\triangle p}{\triangle x} \tag{2.3}$$

It is a function of the horizontal pressure gradient $\frac{\triangle p}{\triangle x}$, gravitational acceleration g ($g = 9,81\frac{\mathrm{m}}{s^2}$) and the Coriolis factor f. The Coriolis factor is the product of the Earth's rotation speed ω ($7.292 \cdot 10^{-5}\frac{1}{s}$) and the sine of the latitude. Therefore it includes the dependence on the latitude in the definition of the geostrophic wind. Geostrophic motion on the NH will occur parallel to isobars (lines of constant pressure) with high pressure on the right and low pressure on the left (see figure 2.4a). It is the opposite for the SH.

Thermal wind is not an actual wind, but the vertical shear of geostrophic wind. In the case of a horizontal temperature gradient the thickness of the layers between isobaric surfaces is not even, but higher in warm regions. Therefore the slope of the upper surface will differ from the lower layer and with it the geostrophic wind. This shear is the thermal wind u_{th} and it is defined as:

$$u_{th} = -\frac{R_L}{f}(\frac{\partial T}{\partial n})ln(\frac{p_l}{p_u}) \tag{2.4}$$

It is a function of the pressure at the lower edge of the layer p_l and at the upper edge of the layer p_u. R_L is the gas constant of dry air and has a value of 287 $\frac{\mathrm{J}}{kg \cdot K}$. Due to the indirect proportionality of thermal wind and the Coriolis factor, thermal wind is stronger in high latitudes. The thermal wind is proportional to the temperature gradient perpendicular to the isotherms (lines of constant temperatures) $\frac{\partial \mathrm{T}}{\partial n}$. In the NH the direction of the thermal wind is directed to the left of the $\frac{\partial \mathrm{T}}{\partial n}$-vector. This means thermal wind "blows" around cold centers anticlockwise (see figure 2.4b) . Due to the change of sign of the Coriolis factor f, conditions are reversed in the SH.

These concepts are very idealized and don't hold for small scale weather phenomena. However, they provide the explanation for the general large scale circulation that is described in section 2.3.2.

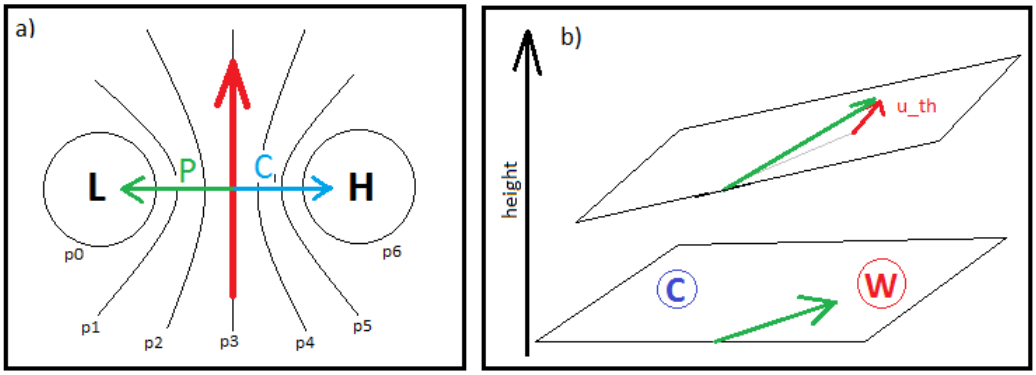

Figure 2.4: Schematic of geostrophic wind (a) and thermal wind (b)

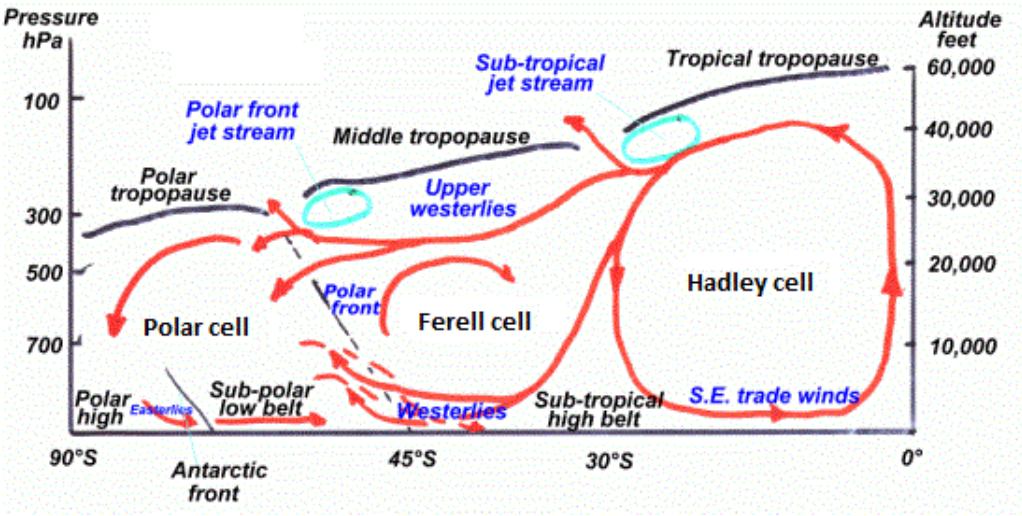

Figure 2.5: Schematic cross section of tropospheric circulation, modified from Pilotfriend

2.3.2 Tropospheric circulation

Meridional air movement in the troposphere is a structure of three cells per hemisphere (figure 2.5). The tropical cell (Hadley cell) and the polar cell are thermally driven. The Hadley cell by the upward motion within the ITCZ, leading to convergence of air masses at the surface (resulting in low pressure at the surface) and divergence near the tropopause. The thermal loop is closed around 30 °N/S, where the poleward moving air masses in high altitudes are cooled down so much, that they sink back to the surface inducing a high pressure belt. The polar cell is driven by subsidence in the polar regions. Due to the low temperature in these latitudes, the cold and therefore heavy air sinks downward from the tropopause layers, leading to high

pressure at the surface. Equivalently to the Hadley cell, the cold air masses at the surface move south and rise in the regions of low pressure around 60 °N/S. The third cell (Ferrell cell) is a thermally indirect cell, resulting from the polar and Hadley cell. It is constituted in poleward flow near the surface and equator-ward flow in higher levels.

In the lower atmosphere the main bands of zonal wind follow the concept of geostrophy. Due to the Coriolis force the horizontal flow within the circulation cells have zonal components. Thus, as part of the Hadley cell, around the equator the trade winds are directed to the West. The mid-latitudes are dominated by westerlies and easterlies surround the polar regions of high pressure. Due to the land distribution, zonal flow in the SH is far more symmetric and reaches higher wind speeds in the belt of mid-latitude westerlies.

2.3.3 Stratospheric circulation

The horizontal circulation in the stratosphere is basically geostrophic. Due to the absence of solar heating, there is a temperature minimum at the winter pole, while high UV-absorption at the summer pole increases temperatures there. This causes a temperature gradient that spans both hemispheres. The strongest gradients are in high latitudes and induce strong zonal flow, following the equation of thermal wind (2.4). Therefore in winter strong westerlies can be found throughout the troposphere and stratosphere.

This large cyclonic circulation around the pole is called the polar vortex. Within the polar vortex large-scale downward motion, connected to adiabatic warming, balances the strong radiative cooling. The polar vortex is significantly stronger and more symmetric in the SH compared to the NH. This is due to lower temperatures in the SH and higher generation of planetary waves, which disturb the vortex, in the NH (section 2.3.4.). A strong polar vortex with very low temperatures during early and mid-winter increases the ozone depletion rates in the following spring. Especially when the temperature drops below approximately -80 °C, the abundance of chlorine oxides is significantly elevated (WMO, 2006). On average the polar vortex exists until spring, when solar radiation reaches the polar regions and warms the stratospheric layers. In summer the zonal circulation in the stratosphere is reversed, since the trans-hemispheric temperature gradient is reversed. Easterly wind speeds dominate the polar stratosphere, but wind speeds are considerably lower than in winter.

In contrast to the troposphere, the meridional circulation in the stratosphere consists of only one circulation cell per hemisphere. The so-called Brewer-Dobson-Circulation (BDC) manifests in upward motion in the tropics, poleward flow in the stratosphere and descending air masses in the polar and sub-polar regions. The BDC is driven by wave breaking in the stratospheric high and mid-latitudes, which draws air downward in the polar stratosphere (Holton et al., 1995). This mechanism is often named the “extra-tropical pump” or “downward control” (Holton et al., 1995; Haynes et al., 1991). The following section will provide more information about wave-induced circulation changes in the stratosphere.

2.3.4 Dynamical interaction of troposphere and stratosphere

Due to the large differences in composition and dynamics troposphere and stratosphere are usually considered two separated layers. The thermal stratification inhibits most vertical motion across the tropopause layer. However since anthropogenic substances, emitted at the surface, are the main cause for catalytic ozone depletion in the stratosphere, the air mass

exchange between troposphere and stratosphere is of importance. The key region of tropospheric input into the stratosphere is located in the tropics, where the main mass transfer via deep convection takes place, while in the polar regions downward mass transports dominates (Holton et al., 1995).

An important coupling mechanism between troposphere and stratosphere is given by atmospheric waves, namely Rossby and gravity waves. Those waves are generated in the troposphere due to disturbances of the flow by topography or localized heating or cooling. These waves can propagate upward, transporting energy into the stratosphere. There are different theories for this wave propagation, one of the most accepted is the Charney-Drazin theory (Charney and Drazin, 1961). The often quoted Charney-Drazin criterion states that waves can only propagate vertically when wind speeds are westerly and below the critical value of 38 $\frac{\mathrm{m}}{s}$. This means the waves will only propagate in case of weak westerly winds, but not in case of a strong polar vortex or during the summer circulation. Therefore the strongest wave activity in the polar stratosphere can be found in winter in the NH and in spring and autumn in SH.

The details of the wave induced coupling of stratosphere and troposphere are not understood completely, but mainly two mechanisms are assumed: wave reflection and wave breaking (Perlwitz and Harnik, 2004, Graf et al., 2007). Wave reflection can take place in the lower stratosphere and upper troposphere, when high wind speeds prevent upward propagation of the waves. Another possibility is the reflection near the stratopause due to a strong negative wind shear. The reflected signal influences the phase and amplitude of tropospheric waves (Perlwitz and Harnik, 2003). When the zonal flow has moderate wind speeds and fulfills the Charney-Drazin criterion, vertically propagating waves can reach the upper stratosphere, where their amplitude increases until they break. This breaking disturbs the zonal mean flow and weakens the polar vortex. The meridional circulation is accelerated this case, since the breaking of the waves adds momentum in the respective layers. Therefore the BDC is stronger in the winter hemisphere, when westerly wind speeds allow for enhanced wave breaking in the stratosphere and the "extra-tropical" pump is strong.

A stratospheric impact on the surface circulation has been found in zonally symmetric surface anomalies in the polar NH by Thompson and Wallace (1998). They linked the dominating pattern of surface pressure variability (Arctic Oscillation) to changes in the zonal flow at 50 hPa (lower stratosphere). Such downward propagation of the anomalous zonal mean flow signals exists on various intra-annual time scales (Baldwin and Dunkerton, 1999, 2001; Christiansen, 2001, Nikulin and Lott, 2010). In a model study by Graversen and Christiansen (2003) the differences in the coupling of stratosphere and troposphere on the two hemispheres were compared. They found downward propagation of zonal mean zonal wind anomalies on both hemisphere, but a slight shift in the seasonality. While the coupling is most pronounced in spring on the SH, in the NH is is present throughout the winter half-year. In addition they found that the coupling is in general weaker, but faster in the SH.

2.4 The annular modes

Due to the approximately zonally symmetric circumpolar structure of the Arctic Oscillation pattern and its SH equivalent, those modes of variability have been labeled annular modes, the Northern Annular Mode (NAM) and the Southern Annular Mode (SAM) (Thompson and Wallace, 2000). The annular mode indices are used to quantify changes of the extra-tropical

zonal flow after large, explosive volcanic eruptions.

At the annular modes can be considered as the ratio between the subtropical belt of high pressure and the sub-polar low pressure systems, which are strongly anti-correlated. They are defined as the first mode of variability (section 3.3.3) in the extra-tropical field of sea level pressure (SLP) and a fraction of 20% (NH) and 27% (SH) of the SLP field (Thompson and Wallace, 2000). The annular modes are defined such, that a positive index means a shift of the atmospheric mass to lower latitudes, higher pressure in subtropical regions and lower pressure in the region of sub-polar low pressure. According to the theory of geostrophy, the increase of the horizontal pressure gradient in the mid-latitudes results in a strengthening of the mid-latitude westerlies.

In the stratosphere the annular modes mainly describe the variability of the polar vortices. A positive stratospheric NAM or SAM is equivalent to a strong cold polar vortex. Throughout the whole troposphere and stratosphere each mode explains between 30 and 50 % of the total variance of the geopotential height and wind fields in the respective hemispheres (Thompson and Wallace, 2000).

Since this study focuses on the SH the SAM index is described in more detail.

2.4.1 SAM

The pattern of anti-correlating surface pressure in the SH mid-latitudes and polar regions was first discovered by Gong (1992). Gong and Wang (1999) carried on those studies and developed an index for the Antarctic Oscillation (section 3.3.2). The name SAM was chosen for comparability to the NH (Thompson and Wallace, 2000). Figure 2.6 a) shows the SLP pattern associated with a positive SAM index in reanalysis data. It shows a almost annular pattern of very low SLP centered on the South Pole and increased SLP in the mid-latitudes. The resulting steepening of the surface pressure gradient does not only lead to increased wind speeds in the belt of sub-polar westerlies, but also to a poleward shift of those westerlies. In addition, the surface temperature is closely linked to the SAM, a positive index meaning lower temperatures over Antarctica (see Figure 2.6 b).

Variations in the SAM index have the largest impact on the climate of Antarctica, but also affects the atmosphere and ocean of the whole SH. Rainfall measurements in South America, Africa, Australia and New Zealand have shown significant correlation with the SAM index (Hendon et al., 2007, Silvestri, 2009). The ocean is affected via changes in the surface winds. Studies have shown connections between the SAM index and changes in the circulation and biology of the Antarctic Ocean and the formation of deep water and sea ice near the Antarctic continent (Lovenduski and Gruber, 2005, Gordon et al., 2006, Yuan and Li, 2008).

Since the mid-1960s a positive trend in the SAM index has been observed in the stratosphere (Hurrell and van Loon, 1994; Zhou et al. 2000) as well as in the troposphere (Thompson et. al., 2000; Marshall, 2003). The stratospheric trend is linked to a delayed breakup of the polar vortex and therefore strongest in SH spring (Randel and Wu, 1999; Zhou et al., 2000; Thompson and Solomon, 2002). Due to the downward propagation of these signals, the maximum tropospheric changes are slightly delayed and most pronounced in summer (Thompson and Solomon, 2002).

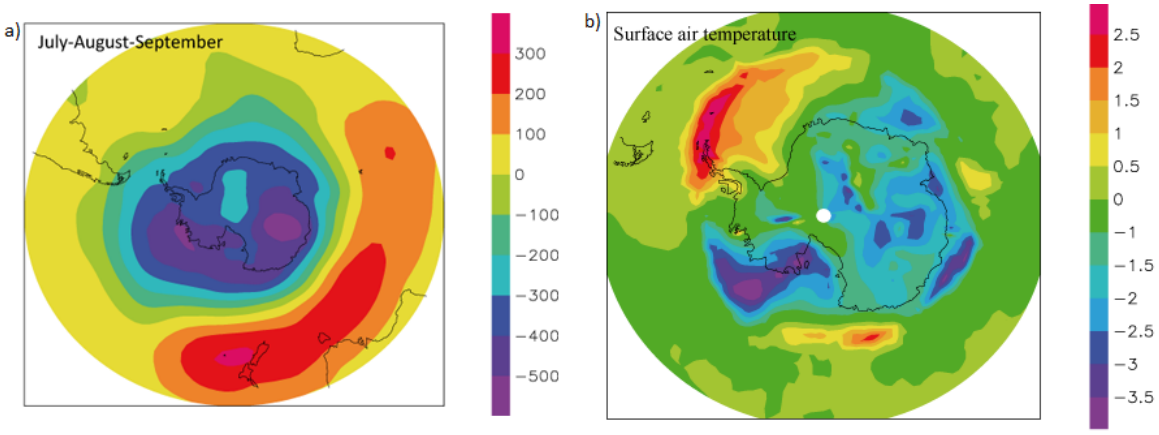

Figure 2.6: Regression pattern between SAM-index and surface pressure (a) and the SAM index and surface temperature (b) in NCEP/NCAR reanalysis data averaged for the months April to June from 1980-1999 in Pa (Goosse et al., 2012)

These trends have been linked to temperature changes in the polar cap. Most model studies agree that the driving forces are ozone depletion and the increase of greenhouse gases (Thompson et al., 2000, Shindell and Schmidt, 2004, Miller et al., 2006, Sigmond et al. 2011).

Ozone loss affects the stratospheric circulation via a decrease in temperature (less UV-absorption), strengthening the polar vortex. Those signals can migrate downward and be observed in a positive surface SAM. Randel and Wu (1999) name two possible positive feedbacks: a) A cold polar vortex favors ozone depletion. b) In case of a strong polar vortex, wave activity is reduced (see Charney-Drazin-criterion), weakening the BDC, and therefore the transport of ozone into the polar regions.

Fyfe et al. (1999) simulated a positive surface SAM trend with greenhouse gas forcing only. Surface heating due to an increase in tropospheric greenhouse gases is stronger in tropical regions, where more long-wave radiation is emitted. This increases the latitudinal temperature gradient and strengthens the sub-polar westerlies, hence the surface SAM index.

2.4.2 NAM

Due to more land masses and thereby stronger wave activity, the annular mode of the NH has a less annular structure. The NAM basically describes the same pattern of variability as the Arctic Oscillation and correlates strongly with the North Atlantic Oscillation (Thompson, 2007). The impacts of these modes have been studied more extensively than the SH equivalent, since the effects on human life are more direct due to the dense population in the Northern high and mid-latitudes (e. g. de Beurs and Henebry, 2008; Archambault et al. 2008). Also in the NH a positive trend in the annular mode has been observed with most significant changes in the season of January to March (Thompson et al., 2000). General circulation models have managed to simulate this trend when allowing for GHG and ozone-related forcing (Shindell, 1999; Langematz et al., 2003; Miller et al., 2006). In contrast to observational studies (Thompson et al., 2000), model studies indicate that the impact of ozone changes is negligible for the NAM trend. Instead the increase of GHGs are the dominant driver of the shift towards positive NAM indices. (Miller et al., 2006).

2.4.3 Natural influences on SAM variability

In addition to the anthropogenic influences on the SAM index, there are also natural impacts on the extra-tropical circulation.

2.4.3.1 ENSO

The first one that that usually comes to mind would be the El Niño/Southern Oscillation (ENSO), since it is the most dominate mode of variability at the surface on a global scale. ENSO describes a complex coupled ocean-atmosphere phenomenon in the tropical Pacific Ocean with an oscillation period between 2 and 7 years. In the ocean a positive ENSO phase (El Niño) is characterized by a weakening of coastal upwelling at the west shore of South America and a warming of the tropical Eastern Pacific. In the atmosphere the trade winds, subsidence over the Eastern Pacific and convection over the Western Pacific are weakened. Several studies showed the global impact of ENSO, but the effects on the extra-tropical circulation are not fully understood yet.

The earliest studies examined the relation between the NH extra-tropical circulation and ENSO and found no significant influence of ENSO on the polar vortex (van Loon and Labitzke, 1987; Hamilton, 1993). More recent studies showed a weakening effect of El Niño on the NH polar vortex due to increased vertical wave propagation (Manzini et al., 2006; Metzner, 2008). Only recently, similar investigations were made about the SH extra-tropical circulation.

In most observational studies El Niño is related to a negative surface SAM (Ribera and Mann, 2003; Gong et al., 2010; Fogt et al., 2011). The suggested mechanisms are related to preconditioning of the zonal circulation due to horizontal wave forcing. In La Nina years the breaking of anticyclonic waves on the equator-ward side of the westerlies is favored. Those waves accelerate the zonal flow. L'Heureux and Thompson (2006) examined the seasonality of and ENSO index and the SAM index in NCEP/NCAR reanalysis data from 1979 to 2004 and found the strongest anti-correlation in austral summer. When averaged over 4 months the ENSO explained 25% of the summer SAM variability.

The impact of ENSO on the stratospheric SH circulation is less clear and has not been included in most studies about impact of ENSO on SAM. Gong et al. (2010) also assumed the SH polar vortex to be affected by ENSO. They found strong stratospheric SAM anomalies prior to coinciding surface SAM/ENSO events and consider these stratospheric anomalies to excite tropospheric circulation anomalies. They suggested a possibly ENSO related modification of vertical wave propagation is responsible for changes in the stratospheric circulation. A recent study by Xie et al. (2012) distinguished between the classical Eastern Pacific El Niño (EPE) and a Central Pacific El Niño (CPE). They analyzed ERA-interim data from 1978 to 2019 and found a cooling of the SH polar stratosphere and a decrease in upward wave activity flux during EPE years, which would result in a strong polar vortex. In CPE there is a warming throughout the whole polar troposphere and stratosphere, that would result in a weakening of the polar vortex and a negative SAM at the surface and in the stratosphere.

2.4.3.2 QBO

Another source of SAM variability, the Quasi-Biennial Oscillation (QBO), can be found in the tropical stratosphere. Zonal wind in the tropical stratosphere alternates between easterlies and westerlies with time periods between 22 to 34 months (on average 28 months). The

signal of this oscillating mean flow can be found from the stratopause at 1 hPa (approximately 48 km altitude) to pressure levels of approximately 100 hPa (approximately 18 km altitude) propagating downward. Maximal amplitudes have been observed near 20 hPa with the average westerlies at 15 $\frac{\mathrm{m}}{s}$ and average easterlies at 30 $\frac{\mathrm{m}}{s}$ (Labitzke and van Loon, 1999). The source of the QBO lies in the tropical troposphere. A broad spectrum of equatorial waves propagating upwards is the driving force of this stratospheric oscillation. The QBO has been shown to affect the stratospheric polar circulation by altering the wave guide of planetary waves (Holton and Tan, 1980). Following the Charney-Drazin criterion, waves can only propagate when the wind direction is eastward. Thus if the QBO is in a westerly phase planetary waves can spread into tropical regions, while an easterly phase restricts wave activity to mid-latitudes and polar areas. In the case of the easterlies wave activity in the polar regions is stronger and planetary waves weaken the annular structure of the polar vortex.

Baldwin and Dunkerton (1998) showed that the influence of the QBO on the SH polar vortex is strongest in SH spring, when wave activity is highest. The same seasonality had been observed in the NH, where the strongest impact of the QBO on polar vortex is found in the NH winter months (Baldwin and O'Sullivan, 1995).

2.4.3.3 Solar cycle

Also the strength of the solar radiation influences the SAM. The sun's radiance follows a cycle with periods between 10 and 12 years (11-year-sunspot cycle). In years of many sunspot, the sun's radiation is stronger and the radiative heating of the stratosphere increases. However the impact of the solar cycle on the polar circulation seems to be modulated the QBO. Labitzke (1987) found the effect of the amount of sunspots on temperature in the NH polar stratosphere to be stronger during westerly QBO phases. More recent studies found such a relationship for the SH. Labitzke (2004) used NCEP/NCAR reanalysis data and showed that depending on the phase of the QBO a solar maximum has opposite effect on the Brewer-Dobson Circulation and therefore on the polar vortex. In years of an easterly QBO regime plus a solar maximum, they found an the warming of the stratosphere is mostly restricted to the tropics and subtropics, increasing the horizontal temperature gradient. The warming pattern in the tropical stratosphere implied a decrease in upward motion and a weakening of the BDC. The following decrease in down-welling (adiabatic warming) in polar regions plus the stronger temperature gradient lead to a colder stronger vortex. During the westerly phase the warming is spread throughout the whole stratosphere and a warm and weak vortex is found. Haigh and Roscoe (2006) and Roscoe and Haigh (2007) showed that the product of indices of the QBO and the solar cycle correlate significantly with the SAM index all throughout the atmosphere.

2.5 The impact of volcanic eruptions on climate

Since the impact of volcanic eruptions on the SAM index is the topic of this study, the volcanic effects on the atmosphere are described in more detail. The strength of volcanic eruptions related to the amount of particles and gases it ejects and can be expressed in different indices. Common indices are the Volcanic explosivity index (Newhall and Self, 1982) or the Dust Veil Index (Lamb, 1970). However, such an index does not necessarily relate to the eruption's impact on climate. The location of the volcano and the composition of the volcanic material

injected into the atmosphere is of great importance for a possible effect on climate. The reasons for that are explained in the following.

Due to the turbulent nature of the troposphere, the lifetime of particles is short in this layer. Also background concentration of emitted gases are too high in this layer to allow for a volcanic impact on climate. Therefore a significant climatic effect is only given when the volcanic eruption reaches the stratosphere. Due to the nature of the large-scale meridional circulation (BDC), volcanic material injected in the high-latitudes is transported out of the stratosphere quickly. Therefore strong tropical volcanic eruption are the most effective in regard of global climate forcing.

The main components of the volcanic material injected into the atmosphere are ash, water vapor, nitrogen and carbon dioxide (Robock, 2000). The emitted greenhouse gases have very little effect, since their concentrations are small in comparison to the background levels. Ash particles are washed out of the atmosphere quickly because of their size and weight and have a small impact on climate (Robock, 2000). The most relevant volcanic element for the Earth's climate are sulfur compounds (Rampino and Self, 1984). The most common form is Sulfur dioxide (SO_2). As an example, the eruption of Mount Pinatubo produced about 17 million tons of stratospheric SO_2 (Guo et al., 2004). Such sulfur compounds react with hydroxide (OH) or water vapor (H_2O) and form liquid sulfuric acid (H_2SO_4) aerosols, which strongly interact with solar radiation (Robock, 2000).

These aerosols are not restricted to the area of the eruption. If the eruption is strong enough to reach the stratosphere and takes place in lower latitudes, the aerosols are first advected zonally by the strong band of zonal wind above the equator (QBO), circling the globe in a matter of weeks. On time scales of several months, they are transported into polar regions (Trepte et al., 1993). The meridional distribution of aerosols depends on the seasonality of the volcanic eruption, due to the strong seasonal cycle of the BDC (Toohey et al., 2011).

2.5.1 Radiative effects

The radiative responses to a volcanic eruption are summarized in figure 2.7. One of the main effects is the increase of the planetary albedo. H_2SO_4- aerosols interact strongly with sunlight, since their radius is of similar size as the wavelengths of visible light. Part of the incoming sunlight is reflected at the aerosol clouds, thus less direct solar radiation reaches the Earth's surface and temperatures in the troposphere drop. This effect has already been observed early in history, early records mention strong cooling after the eruption of Mount Etna 44 B.C. (Forsyth, 1988). Another fraction of the incoming sunlight is scattered forward, meaning more diffusive radiation reaches the surface. This reduces the strong cooling effect. The aerosols do not only scatter radiation but also absorb it. Solar near infra-red radiation as well as terrestrial infra-red radiation is absorbed, leading to a warming of the layers of the aerosol cloud. Following equation (2.1), higher temperatures lead to stronger emission of long-wave radiation back to the surface. Therefore a heating of the upper layers has a reducing effect on the surface cooling.

However, the total downward radiation is reduced, since the cooling effect of the blocked sunlight is dominant. Robock and Mao (1995) investigated composites of the 6 eruptions with the highest VEI and DVI within the 19^{th} and 20^{th} and have found global surface cooling of 0.1-0.2 °C for two years after the eruptions.

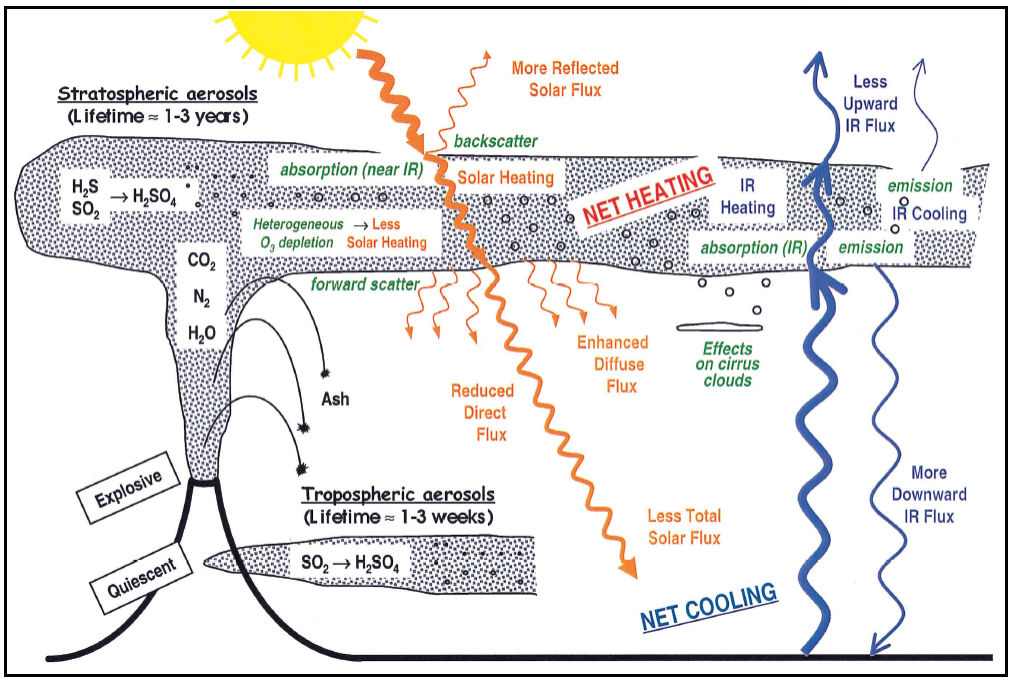

Figure 2.7: Schematic of volcanic input to the atmosphere and their effects (Robock, 2000)

2.5.2 Dynamical response

The warming of the stratosphere after a strong tropical volcanic eruption is most prominent in the tropics, where the aerosol input takes place. In this region solar forcing is the strongest and due to the large-scale circulation the aerosol have a longer life-time. This leads to an enhanced meridional temperature gradient in these layers. According to the thermal wind equation, that temperature gradient results in a strengthening of the westerly winds, the polar vortex and a positive annular mode in the stratosphere.

An the surface, the cooling effect of aerosols is strongest in tropical regions, reducing the meridional temperature gradient. Therefore the surface zonal mean flow in the mid-latitudes and the surface SAM weaken. Since the horizontal temperature gradients in the troposphere are a source of planetary wave development, the weak gradient can be expected to reduce wave generation in the troposphere and hence lead to a strong cold polar vortex in the winter hemisphere. However, Graf et al. (2007) examined polar wave activity on the NH in reanalysis data and found an enhanced wave activity in the stratosphere in years of strong volcanic eruptions, but also identified a stronger polar vortex than in other years.

A curiosity has been observed on the NH. In winters following strong volcanic eruptions, temperatures above the continents of Northern Europe and North America increased in a pattern similar to positive NAO conditions (Robock and Mao, 1995, Kelly et al., 1996). This winter warming shows that an advective effect is stronger than the radiative in the extra-tropical troposphere. Heat advection to the continents in the post-volcanic NH winters has been related to a positive phase of the surface NAM. The circulation anomalies have been suggested to be linked to a strong polar vortex due to the downward coupling (section 2.3.4). Wave reflection influences the planetary waves in the troposphere, possibly leading to the

stationary wave pattern in the middle troposphere with high pressure anomalies above North America and Europe, that causes heat advection to the continents (Graf et al., 1993).

2.5.3 Chemical effects

Another impact of volcanic eruptions on climate has only become of interest since the 20^{th} century. As already mentioned, the depletion of stratospheric ozone includes a series of chemical reactions on the surface of cloud. H_2SO_4- aerosol clouds, produced by volcanic injections into the atmosphere, can also serve as catalyst for those reactions. In contrast to the polar stratospheric clouds, which form during extremely cold conditions in the polar vortex, the sulfate clouds also exist in higher temperatures. Therefore the activation of chlorine (section 2.2.2) is expanded into lower layers of the polar stratosphere as well as to the mid-latitudes (Solomon, 1999).

This volcanic effect has been observed after the eruption of Mount Pinatubo in 1991 (Solomon et al., 1993). In SH autumn of 1992 high concentrations of Cl_2, the result of chlorine activation, have been found, although the activation processes are restricted to winter months in non-volcanic years. Portmann et al. (1996) suggested volcanic aerosols to be the reason for the pronounced SH ozone holes in the early 1980s and the early 1990s following the eruptions of El Chichon and Pinatubo in 1982 and 1991 respectively. The reduced ozone concentrations after volcanic eruptions have a cooling effect on the polar and mid-latitude stratosphere, but the net effect is still a heating in the stratosphere.

Duggen et al. (2007) suggested that also ash could have an effect on climate, that exceeds a local short-lived cooling. When ash particles are washed out of the atmosphere, they could provide nutrients and act as a fertilizer in seawater. An increased biological productivity in the ocean would mean higher photosynthesis rates and remove carbon dioxide from the atmosphere. Reduced carbon dioxide concentrations are linked to reduced absorption of longwave radiation and an atmospheric cooling (section 2.1).

Chapter 3

Data and methods

In this chapter the data and methods to analyze the SAM are introduced. To investigate the dynamical response to volcanic aerosol loading, simulations of a state-of-the-art coupled ocean middle atmosphere model are analyzed.

Due to the chaotic nature of the climate system, small disturbances in the initial conditions of a climate simulation, can have a vast effect on the resulting state of the system. To take those uncertainties into account, model simulations are often carried out as an ensemble of runs with slightly different initial conditions. Here an ensemble of three runs, covering the time period from 1850 to 2000, is investigated. All following figures show the ensemble mean of those three runs.

3.1 Model data

The model data were provided by the Max-Planck-Institute Earth System Model (MPI-ESM). The simulations are part of the Coupled Model Intercomparison Project Phase 5 (CMIP5). Daily and monthly model output is used.

3.1.1 Atmospheric component

The atmospheric component of the model is the 6th generation version of the ECHAM (European Center Hamburg Atmosphere Model) series: ECHAM6. This model has its origin in the weather forecast model of the European Centre of Medium-ranged weather forecast (ECMWF) and was modified for climate research at MPI in Hamburg (ECHAM). Detailed description of this most recent version of the model is not available, but the formulation of the dynamics are similar to the precursor ECHAM5 (Roeckner, 2003). The main changes are the implementation of a vegetation model (JSBACH), improvements in the parametrization of the carbon cycle and the increase of the vertical resolution from 39 to 47 levels (Giorgetta, 2011).

As previous generations of the ECHAM model, most prognostic variables are calculated and truncated in a series of spherical harmonics (Roeckner, 1996). The model version, that provided the data for this study, operates with a horizontal resolution of T63 (triangular truncation at wave number 63), which corresponds approximately to 140 x 210 km grid boxes in mid-latitudes with smaller boxes in high latitudes and biggest boxes at the equator. The vertical levels are determined by a hybrid sigma-pressure coordinate (Simmons and Burridge,

1981). The sigma coordinate follows the surface slopes in the lowest levels and pressure levels near the model's top of the atmosphere (TOA). The vertical resolution is highest near the surface, allowing the model to better resolve processes of the atmospheric boundary layer. The vertical resolution has been increased in comparison to ECHAM5 and reaches an upper level of 0.01 hPa (approximately 80 km) with 47 layers. Therefore it includes the whole stratosphere and most of the mesosphere.

The prognostic variables are vorticity, divergence, surface pressure, temperature, specific humidity, mixing ratio of water vapor and total cloud water as well as optionally trace gases and cloud aerosols. In consideration of the effect of volcanic eruptions, the parametrization of radiation is of special interest. Shortwave and long-wave radiative forcing are calculated separately and depend mainly on the incoming solar radiation and the composition of the atmosphere. The atmosphere's composition includes the prognostic variables as water vapor and cloud water as well as prescribed trace gases, such as ozone and greenhouse gases.

The radiation schemes are parametrized with 14 spectral bands for the solar radiation and 16 bands for the outgoing long-wave radiation (Rack, 2011). The radiative fluxes in ECHAM5 have already shown good agreement with observational data at the surface as well as on top of the atmosphere (Wild and Roeckner, 2006) suggesting that the radiative forcing in ECHAM6 should be simulated quite realistically.

The stratospheric aerosols are prescribed. Since this is the dominant link between volcanic eruptions and radiative forcing of the atmospheric circulation, the aerosol data set will be introduced in more detail further on.

3.1.2 Ocean component

ECHAM6 is coupled to the most recent version of the ocean model MPI-OM (Max-Planck-Institute ocean model). Technical details and a description of the mean ocean circulation in the MPI-OM can be found in Marsland et al. (2003) and Junglaus et al. (2006). The main improvement in comparison to older versions is the integration of the ocean-biochemistry model HAMMOC (Giorgetta, 2011). It is a global ocean model with an embedded dynamical sea ice model. The horizontal grid is based on a bipolar orthogonal spherical coordinate system with the two poles located over Greenland and the Weddell Sea. This improves the resolution in the areas of deep water formation, which is the driving force of the model's thermohaline circulation. The horizontal resolution is 1.5°x1.5°. In the vertical direction a z-coordinate (following the geopotential) is used. Surface elevation is given by adjustment of the surface layer. There are 40 layers and the vertical resolution is highest near the ocean surface.

The coupling frequency of the atmospheric and oceanic component is 24 hours. The coupler used here is the OASIS 3 (Valcke, 2006). It is the latest version of the OASIS couplers, developed at the European Centre for Research and Advanced Training in Scientific Computation (CERFACS, Toulouse, France). Table 3.1 gives an overview over the variables that are exchanged between the two model components.

This coupling of ocean and atmosphere allows oceanic or coupled ocean-atmosphere phenomena to develop and influence each other. The most dominant phenomena would be ENSO. Since the sea surface temperature is not prescribed, this mode of variability can impact the simulated atmosphere and explain differences to observations.

ECHAM6 receives	MPI-OM receives
sea surface temperature	total heat flux over water
sea ice cover	downward short wave heat flux
sea ice thickness	conductive heat flux sea ice
snow thickness on sea ice	residual heat flux sea ice
	wind stress over water and ice
	wind speed
	precipitation (solid and liquid)

Table 3.1: Overview of variables exchanged between the coupled ECHAM6 atmosphere general circulation model and MPI-OM oceanic circulation model.

3.1.3 CMIP5 historical experiment

The MPI-ESM integrations examined in this study are part of the CMIP5 long-term historical integrations (experiment NR. 3.2 according to Taylor et al., 2009). The CMIP project aims to investigate the reasons for differences between various climate models and examine the predictability of future simulation with a multi-model approach. Results are to be evaluated in the IPCC (Intergovernmental Panel on Climate Change) Fifth Assessment Report in 2013. The historical experiments (hindcasts) are climate simulations forced with historic boundary conditions, in this case from 1850 to at least 2005. 20 models are included and for a better comparison, all models have the same forcing.

The greenhouse gases are prescribed using observations. Also the solar forcing is changing with time and contains spectral resolved solar irradiance based on parametrized observation data. For years after 1882, monthly means are available. For earlier years annual means are used to drive the model atmosphere (Lean, 2009).

Ozone is prescribed using the historical data of the AC&C/SPARC ozone database. It is described in detail by Cionni et al. (2011). The stratospheric ozone data set has been generated using a multiple linear regression analysis of satellite and ozone sonde measurements from 1979 to 2009. This data was extrapolated to cover the whole time period of the hindcast using Chemistry Climate Models. The regression includes the annual cycle of ozone concentrations, changes due to the solar cycle and the trend due to increased chlorine loading. The chemical effect of volcanic eruptions is not included.

A summary of all forcing terms can be found on the CMIP5 website (<http://cmip-pcmdi.llnl.gov/cmip5/>).

Due to the nature of this study, the volcanic forcing is described in more detail.

3.1.4 Volcanic forcing

The influence of volcanic eruptions on the climate system is given by the distribution, particle size and concentration of the sulfur acid aerosols. In the MPI-ESM CMIP5 historical simulations these attributes are prescribed using a data set developed by Stenchikov, which covers optical properties of volcanic sulfur aerosols. Details about this data set can be found in Rast (2011). It was originally derived from satellite data and extended using astronomical observations. All parameters are given as zonal means, under the assumption that strong zonal

winds in the stratosphere spread aerosols evenly in East-West direction. The data set includes the variables aerosol extinction coefficient, single scattering albedo, asymmetry factor of the aerosols and the vertically integrated aerosol optical depth (AOD). The first three variables are given on 40 vertical levels.

Optical depth (OD) gives information about the transparency of a medium and is defined by the ratio of radiation entering and leaving the medium. The OD of the atmosphere τ is a function of the radiation arriving at the TOA I_{toa} and the radiation reaching the Earth's surface I_{surf}:

$$\frac{I_{surf}}{I_{toa}} = e^{-\tau} \tag{3.1}$$

An optical depth of zero means there is no scattering or absorption of radiation, while higher values mean a blocking of $\frac{1}{\tau}$ % of the incoming radiation. One contributor to the atmosphere's total OD is the OD due to aerosol loading. Depending on the size of the particles, radiation of different wavelengths interacts with the aerosols. Therefore the AOD varies for different wavelengths.

The AOD forcing, used for the CMIP5 runs, covers 30 spectral bands between 200 and 250000 nm wavelengths. In the solar spectrum the radiation that is scattered and absorbed most by the stratospheric aerosols is the visible light. (Robock, 2000). A comparison of the AOD for different spectral bands (see appendix, figure A1) has shown, that the strongest effect of the volcanic aerosols after the three eruptions with the strongest AOD signal within the time series (Krakatau, El Chichon, Mount Pinatubo) can be found in the spectral band from 442 nm to 625 nm. Therefore in this study the AOD of this spectral band is used to categorize the volcanic eruptions due to their atmospheric impact. Figure 3.1 shows the AOD for the whole time period averaged over the whole globe (blue line) and over the SH (red line) separately. Due to the focus on the SAM, only those eruptions are considered that show an AOD signal in the SH.

Distinguishable peaks of global AOD that reach at least a value of 0.02 have been labeled with the names of volcanoes that erupted during that time and most likely to have caused the opacity of the atmosphere. In table 3.2 the 10 eruptions that have been picked are listed with the month the AOD started to increase and the location of the volcano. Except for the eruption of Cotopaxi, all identified eruptions have a VEI ≥ 4. For this study, three arbitrary categories of eruptions are defined by the strength of the AOD signal:

Eruptions that do not show a AOD signal higher than 0.05 are the "weak" eruptions. AOD peaks between 0.05 and 0.1 are labeled "moderate" . The "strong" eruptions are Krakatau, El Chichon and Pinatubo, with global AOD maxima of more than 0.1. These categories do not agree with a classification due to the VEI.

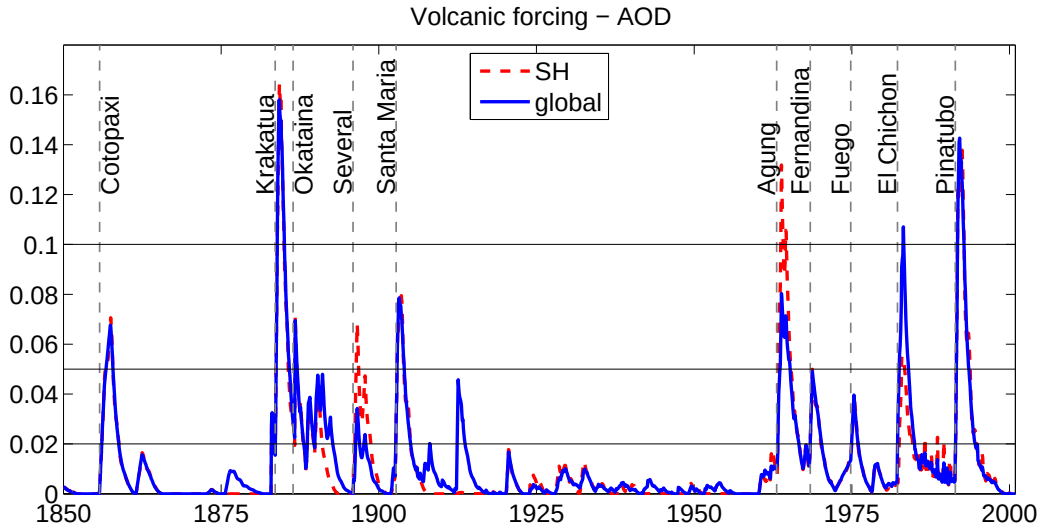

Figure 3.1: Globally (blue) and SH (red) averaged AOD of spectral band 4 (wavelengths between 442 and 625 nm) during 1850 and 2000 in the MPI-ESM CMIP5 historical experiment.

Volcano	initial AOD increase	Location	AOD	VEI	Category
Cotopaxi	10/1855	Ecuador (0°S)	0.07		weak
Krakatau	08/1883	Indonesia (6°S)	0.16	6	strong
Okataina	06/1886	New Zealand (38°S)	0.07	5	weak
Several	12/1895		0.03		moderate
Santa Maria	10/1902	Guatemala (14 °N)	0.08	6	weak
Agung	02/1963	Indonesia (6°S)	0.08	5	weak
Fernandina	06/1968	Galapagos Islands (0°S)	0.05	4	moderate
Fuego	11/1974	Guatemala (14 °N)	0.04	4	moderate
El Chichon	04/1982	Mexico (17 °N)	0.11	5	strong
Pinatubo	06/1991	Philippines (15 °N)	0.14	6	strong

Table 3.2: List of volcanic eruptions that are considered in this study. The month of the initial AOD increase in the forcing used in the MPI-ESM CMIP5 historical simulations, the location (and the latitude) of the volcano, the maximal AOD and VEI (source: Smithsonian, 2011) after the eruption and the category they are sorted into for this study.

3.2 ERA-40 reanalysis data

To evaluate the simulated atmospheric conditions, it is useful to compare it to observations. However, since measurements are inhomogeneously distributed, especially in the SH, global reanalysis data are produced. Reanalysis combines the available observations with physical understanding (a model) to produce the best estimate of the historical state of the climate system. In this study the data set ERA-40 is used, the second generation global reanalysis

data set from ECMWF, which is described in detail by (Uppala et al., 2005).

The reanalysis data are produced by a complex three dimensionally variable (3D-Var) data assimilation system, that fills gaps in the observations using a version Integrated Forecasting System (IFS) of ECMWF. To ensure the continuity of the data set, the same assimilation model was used for the whole time period, despite improvements of the IFS. The IFS is used to forecast a background state of the atmosphere. Those forecast are very short-term (6 hours) and initialized with the previous result of the reanalysis. This background state is then combined with numerous data sets of quality-tested observation data in order to minimize errors and used to initiate a new forecast.

The ERA-40 assimilation system is run with a spectral resolution of T159 (grid boxes of approximately 1.25 °). Data are available in 60 vertical levels, covering the atmosphere until 0.1 hPa pressure level. This resolution is considerably higher than in the comparable reanalysis data set of National Centers for Environmental Prediction (NCEP) and the National Center for Atmospheric Research (NCAR), which has a spectral resolution of T62 and 28 vertical levels (Kalnay et al., 1996). Therefore ERA-40 is suited best for studying stratospheric processes.

The ERA-40 data set covers the time period from September 1957 to August 2002. For the intercomparison of MPI-ESM CMIP5 historical simulations and ERA-40 data, data from 1958 to 2000 is shown. The quality of reanalysis data depends strongly on the quality of the forecast model and the observation data. The ERA-40 observations include aircraft measurements, radiosonde profiles, ship measurements, surface synoptic reports and since 1973 satellite data (Uppala et al., 2004). Especially on the SH, where the observational coverage is very poor, 1973 marks an important threshold of reanalysis quality.

ERA-40 date has exhibited a few problems (Uppala et al., 2005). The assimilation system was not run chronologically for the whole time period, but the time period was divided into 5 chunks and 5 simultaneous runs were started to speed up the production of the reanalysis data. The results of this method are inconsistencies at the transition dates. Other problems of the ERA-40 data are overestimated precipitation over tropical ocean and artificial temperature oscillations in the stratosphere in the daily data. Also the BDC has been found to be too strong, which results in an overestimation of mass transport into the polar regions. The error in the BDC is of interest when it comes to the distribution of trace gases and aerosols. Van Noije et al. (2004) estimated the transport of ozone into the lower stratosphere and troposphere to be a factor of two or three stronger in the ERA-40 reanalysis than in observations(van Noije et al., 2004).

Despite those issues, Marshall (2003) found ERA-40 data to be preferable in comparison to NCEP/NCAR data when it comes to examining the SAM. Comparisons to observed pressure data showed that ERA-40 provides a more reliable representation of the circulation of the SH atmosphere and especially data after 1973 can be trusted.

3.3 The annular mode indices

There are different definitions for the annular mode indices. In this study the EOF-based indices (Thompson and Wallace, 2000) are used. In order to get an impression of the tropospheric and stratospheric circulation and its changes, two SAM indices are defined: The surface SAM index is calculated from sea level pressure (SLP). The stratospheric SAM index is defined using geopotential height (GPH) on the 50 hPa level, which corresponds to a height

of approximately 22 km and represents the lower stratosphere. To examine the troposphere stratosphere coupling, a daily SAM index was calculated on levels between 1000 hPa (surface) and 1 hPa (stratopause) based on GPH as well.

3.3.1 Calculation of anomalies

The basis for calculating the indices are anomalies of SLP or GPH. Isolating volcanic signals is a challenge and different approaches have been used in previous studies. Stenchikov et al. (2006) examined the effect of 9 volcanic eruptions with VEI≥4 in the 19th and 20th century on the Arctic Oscillation and calculated anomalies as the difference from reference periods prior to the eruptions. Those reference periods are chosen as the longest possible time periods with low aerosol loading and vary between 5 and 21 years. However this method could include long-term trends and possibly overestimate the effect of volcanic eruptions. Karpechko et al. (2010) analyzed the SH circulation response to El Chichon and Mount Pinatubo and calculated anomalies by subtracting the linear trend from 1979 to 1999. Before the seasonal cycle is accounted for by identifying a trend for each month separately.

In this study for the monthly values two different ways of calculating the necessary anomalies are used:

1.) The first method includes long-term trends in order to validate the model's ability to simulate a realistic SAM index. To remove the seasonal cycle of the investigated variables, monthly anomalies $\mathrm{X_{anom}}(\mathrm{year, month})$ are defined as the difference between the pressure or geopotential of the particular month $\mathrm{X_{abs}}(\mathrm{year, month})$ and the average of the same month of all other years:

$$X_{anom}(year, month) = X_{abs}(year, month) - \frac{1}{151} \sum_{n=1850}^{2000} X_{abs}(n, month) \tag{3.2}$$

2.) To examine volcanic signals the second method is use. It aims at removing long-term trends and oscillations to allow for a direct comparison of the years after a volcanic eruption at the beginning and an eruption at the end of the 150 years of the historical simulation. A 9-year window centered on the eruptions is used as reference time and the anomaly is the difference from the 9-year running average:

...

$$X_{anom}(year, month) = X_{abs}(year, month) - \frac{1}{9} \sum_{n=year-4}^{year+4} X_{abs}(n, month) \tag{3.3}$$

The temporal length of the data set is reduced by this approach, with 4 years less at the beginning as well as at the end of the time series.

To calculate the daily anomalies, the second method is used, comparing the particular day with the same days in the 9 years around that date.

Since this approach includes the years of the volcanic eruptions in the reference time period, possible volcanic signals could be weaker than in a study as Stenchikov et al. (2006), where a "clear" atmosphere is used as reference. But such a method might overestimate anomalies due to long-term trends, which is avoided by the method used in this study.

3.3.2 EOF-based SAM index

One approach to define a SAM-index is the empirical orthogonal functions (EOF) analysis. This definition was introduced by Thompson and Wallace (2000) as the SH equivalent to the NAM index.

The EOF analysis is a statistical method developed to represent the variability in a data set more efficiently with a reduced amount of data. Following the description of Dommenget (2008), the data set (here the monthly anomalies) D of spatial resolution S and temporal resolution T is decomposed into N spatial patterns of variability (modes) ψ, that are uncorrelated to each other. Each pattern is related to a time series Π, called principal component (PC):

$$\mathrm{D(T \times S)} = \psi\mathrm{(T \times N)} \cdot \Pi\mathrm{(N \times S)} \tag{3.4}$$

The most interesting modes are the ones which explain the highest variance in the time series. Therefore it is normally enough to consider only the first few EOF modes. In the case of the annular mode detection only the first mode is of interest, since it is defined as the dominant pattern of variability in the extra-tropical regions. The EOF analysis is based on the covariance between the data points. Covariance is a measure of the common variability of two variables or in this case between two data points. To calculate the modes and PCs of a data set, the eigenvalue problem for the covariance matrix $\sum$ has to be solved:

$$det(\sum - \lambda \cdot I_S) = 0 \tag{3.5}$$

$$(\sum - \lambda * I_S)\pi = 0 \tag{3.6}$$

I_S is the identity matrix of size $\mathrm{S \times S}$. The eigenvalue λ gives information about how much variance of the data set is explained by the corresponding mode, which is expressed in the eigenvector π. Following equation (3.4), the time series related to the spatial pattern can be determined. Since the data for this study is provided on a regular lat-lon grid, the varying size of the grid boxes has to be considered. Therefore an area weighting is applied to the data before applying the EOF analysis.

The SAM index is defined as the normalized PC of the first mode of SLP (or GPH) variability in the region south of 20°S. The EOF analysis is based on the whole available time series and all calendar months following the definition of the NOAA/National Weather Service Climate Prediction Center (CPC, 2012). This could affect the SAM index, because it has been shown that variability and the amplitude of the leading EOF mode is higher in seasons of high wave activity (Thompson and Wallace, 2000).

The advantage of this method is its applicability to all levels, since the index always describes the dominant pattern of variability. It is also the most common way to define the NAM-index.

Chapter 4

Results

4.1 General performance of MPI-ESM

When working with model data it is necessary to compare the simulated climate system with observations. Only when the unforced climatology and variability in the model is realistic, one can expect a realistic response to external forcing. In this chapter the climatological conditions of the model atmosphere and the model's ability to simulate a realistic SAM are evaluated. The model results are shown as the ensemble mean of the three MPI-ESM CMIP5 historical experiment runs.

4.1.1 Temperature climatology

Since the most direct impact of a volcanic forcing is on temperature via radiative changes, systematic errors in the simulation of temperature should be considered when discussing the volcanic impact on climate. Figure 4.1 (right panel) shows the vertical profile of globally and annually averaged temperature from MPI-ESM. The time period from 1979 to 1996 and levels up to 1 hPa have been chosen for a direct comparison with the GCM-Reality Intercomparison Project for SPARC (GRIPS) climatology (Pawson et al. 2000), which compares 13 middle atmosphere climate models (CMAM) of different resolutions and satellite-based observational data (figure 4.1, left panel). The observational profile (black line, left panel) shows the highest temperature of approximately 288 K at the surface. The temperature decreases with height until 100 hPa pressure level (approximately 16 km altitude, tropopause level), with a minimum temperature of about 210 K, and an increase above that. Overall, the MPI-ESM temperature profile agrees well with the observation and the GRIPS models' profiles. The GRIPS models exhibit a lower spread of about 5 Kelvin between 1000 hPa and 300 hPa, which increases with height to maximal differences of approximately 20 K. The MPI-ESM profile lies within that spread in all levels. In comparison to observations, all models have a cold bias in the troposphere and most have a cold bias in the stratosphere. Only around 3 hPa (upper stratosphere) the MPI-ESM profile shows higher temperatures than observed. Overall the MPI-ESM lies well within the range of the GRIPS models and agrees reasonably with observations, but no obvious improvement in comparison to the CMAM can be found.

Figure 4.2 shows zonal mean temperatures for January and July as a function of latitude and pressure for the ERA-40 reanalysis (left panels) and the model (right panels). Due to the

availability of the ERA-40 data and the examined time period from the model simulations, only the years from 1958 to 2000 up to 1 hPa (stratopause) are included in these climatologies for both data sets. The overall distribution of the climatological temperatures show a very good agreement between the model simulation and the reanalysis.

In the reanalysis data there is a cold tropical tropopause (∼100 hPa), that reaches temperatures below 195 K in January and below 200 K July. The summer polar tropopause is warmer in the NH compared to the SH, temperatures of more than 230 K, while in the SH the polar tropopause in January displays temperatures around 225 K. In the winter months the polar atmosphere shows a pronounced temperature minimum in the lower to middle stratosphere of the respective hemisphere, the center of the polar vortex. The vortex is much colder in the SH with temperatures below 185 K than in the NH, where temperatures stay around 200 K. The highest temperatures in the stratosphere can be found near the summer stratopause with approximately 290 K in the NH and more than 285 K in the SH.

The model simulates a slightly colder tropical tropopause than the reanalysis data in both months, but the seasonal differences are of similar amplitude. The summer polar tropopause levels are also simulated to be slightly too cold, with biases in the range of 5 K. In contrast to the negative bias above the winter pole, that was a common problem of coupled troposphere–middle atmosphere models (Pawson, 2000), the MPI-ESM simulates temperatures within the NH polar vortex slightly too warm (bias of less than 5 K). This has already been found in for a L31 version of ECHAM5, the precursor of ECHAM6, and was attributed to an overestimated gravity wave drag in the winter hemisphere (Roeckner, 2006). This wave drag would lead to increased subsidence in the polar regions and result in too strong adiabatic heating. The summer polar stratopause temperatures show a negative bias in both hemisphere in the order of more than 10K.

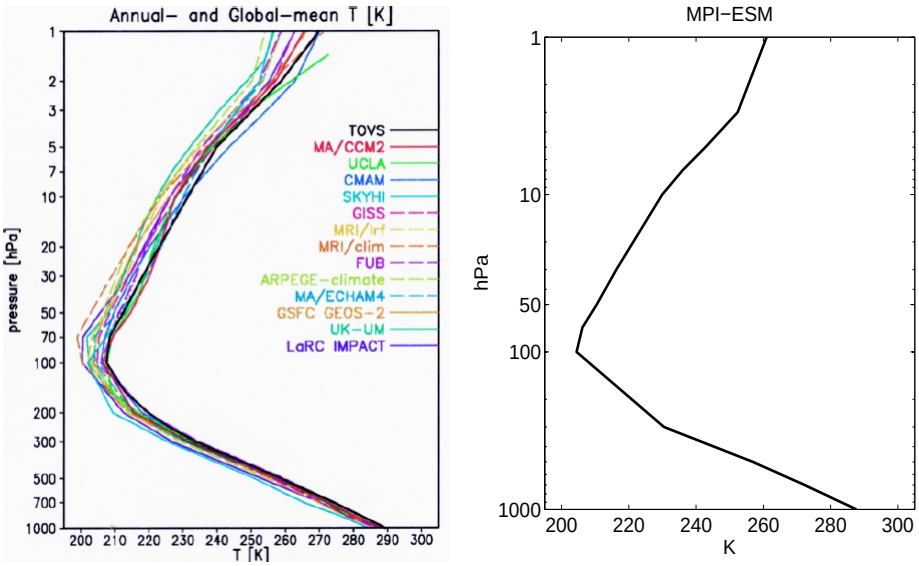

Figure 4.1: Vertical structure of the annual mean global mean temperature (K) from 1979 to 1996. The left panel is from GRIPS (Pawson et al., 2000) with observations (thick black line) and 13 CMAM models (thin colored lines). The right panel shows the ensemble mean of the MPI-ESM CMIP5 historical experiment based on monthly data.

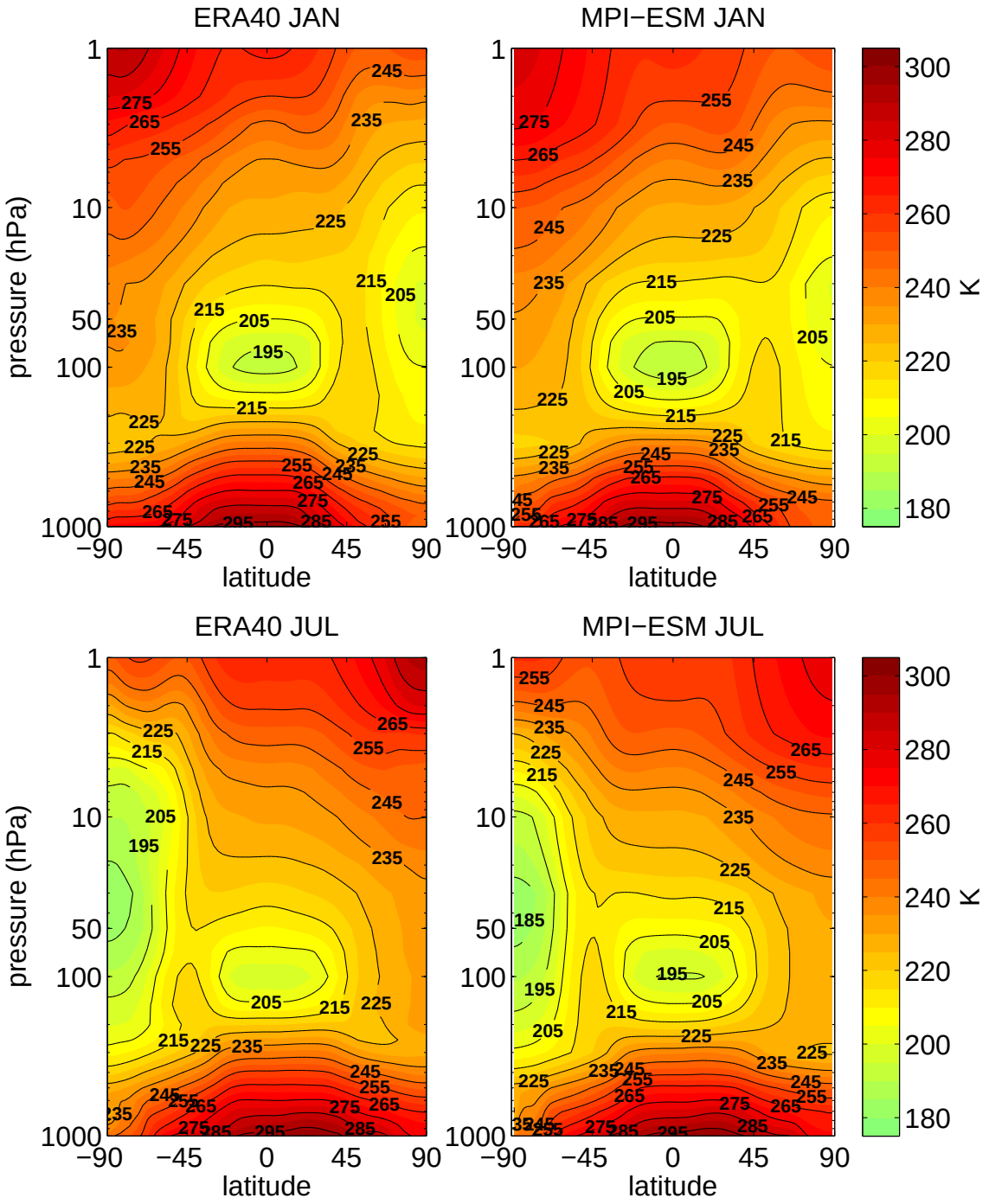

Figure 4.2: Zonal mean January (upper panels) and July (lower panels) temperature (K) climatologies from 1958 to 2000 based on monthly data. The left panels show the the ERA-40 reanalysis, the right panels ensemble mean of the MPI-ESM CMIP5 historical experiment, with color contour intervals of 5 K and black contours with intervals of 10 K.

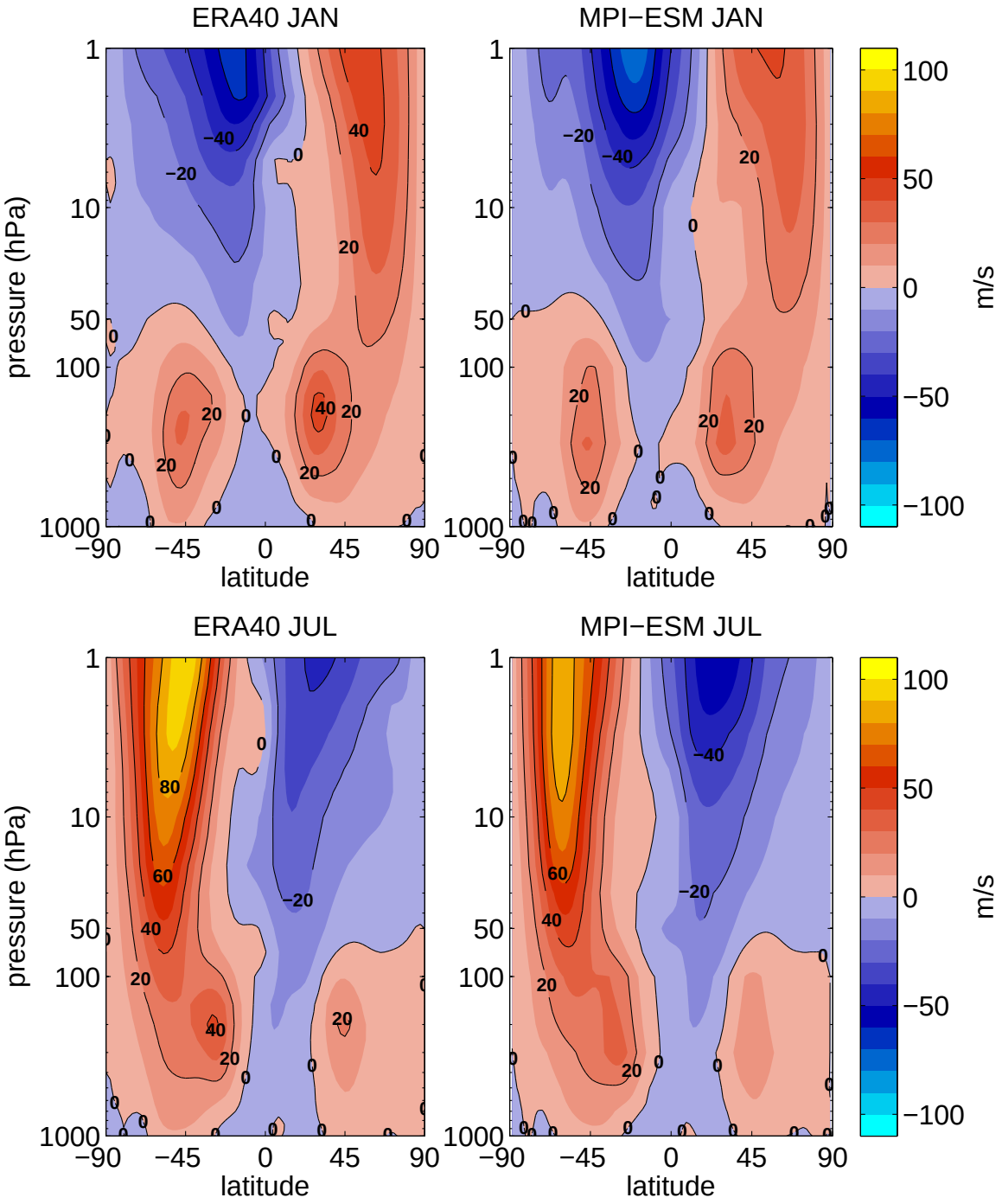

Figure 4.3: Zonal mean zonal wind ($\frac{\mathrm{m}}{s}$) for January (upper panels) and July (lower panels) climatologies from 1958 to 2000 based on monthly data. The left panels show the ERA-40 reanalysis, the right panels the ensemble mean of the MPI-ESM CMIP5 historical experiment result, with color contour intervals of 10 $\frac{\mathrm{m}}{s}$ and black contours with intervals of 20 $\frac{\mathrm{m}}{s}$.

4.1.2 Wind climatology

Figure 4.3 shows the zonally averaged zonal wind in January and July as represented in the model and the reanalysis data.

In the ERA-40 data in January (upper left panel), the subtropical jets can be found at 45°S and 30°N with maximum westerly wind speeds of 25 $\frac{m}{s}$ and 40 $\frac{m}{s}$ respectively. In the winter hemisphere, westerlies are present at all heights. The NH polar night jet, which forms the edge of the polar vortex, displays maximum wind speeds of 40 to 50 $\frac{m}{s}$ in the upper stratosphere and lower mesosphere. In ERA-40, the easterlies on the summer hemisphere can be found throughout the stratosphere and lower mesosphere. The easterly winds increase with height and reach maximum values of 70-80 $\frac{m}{s}$ at levels around 1 hPa.

The model captures the climatological January zonal mean winds well (upper right panel). The wind speeds of the subtropical tropospheric jet in the NH are underestimated up to 5$\frac{m}{s}$ by the model with maximum values between 30 and 40 $\frac{m}{s}$, but the position of the subtropical jets is simulated realistically. Wind speeds in the polar night jet are slightly underestimated in comparison to ERA-40, which is related to the warm bias in the winter stratosphere. The equator-ward tilt of the NH polar night jet is captured well in the model. Pawson et al. (2000) showed that it is a frequent problem of middle atmosphere models to show a clear separation between the polar night jet and the tropospheric subtropical jet, but there is a clear distinction at approximately 100 hPa in the MPI-ESM January climatology. In contrast to the westerlies, the easterly wind speeds in the SH are simulated approximately 10 $\frac{m}{s}$ too strong. Therefore there is an easterly bias in wind speeds at most levels and latitudes.

In July, the observed subtropical jets are shifted northward by approximately 10° on both hemispheres compared to January (lower left panel). The SH polar night jet is about twice as strong as in the NH. These features are also found in the MPI-ESM climatologies (lower right panel). As in January the easterlies in the stratosphere of the summer hemisphere are simulated too strong and the wind speeds of the polar night jet are simulated slightly too weak in comparison with the reanalysis. The model polar night jet does not display the equator-ward tilt that can be found in the ERA-40 climatology, therefore the core of the jet is located south of the reanalysis core. In contrast to January, the subtropical jet in the winter hemisphere appears like an extension of the stratospheric westerlies instead of showing a distinct maximum in the troposphere.

Since the zonal flow anomalies after volcanic eruptions on 50 hPa are analyzed in this study, the climatological wind speed on this level are examined in more detail. Figure 4.4 shows the seasonal evolution of the monthly mean zonal wind speeds at 50 hPa as a function of latitude and calendar day. In the NH, the ERA-40 data (left panel) shows westerlies from August to June. The highest NH westerly wind speeds in the reanalysis are present in December and January, reaching values above 20 $\frac{m}{s}$. In the SH, the westerlies last throughout most of the year, only around the turn of the year weak easterlies can be found south of 60°S, which means a complete reversal of the zonal circulation during this time. The strongest westerlies of 55 $\frac{m}{s}$ appear in August and September. The lower-latitudes are dominated by easterlies with the highest wind speeds in the respective summer hemispheres.

The MPI-ESM (right panel) simulates the seasonality of the westerlies very well on both hemispheres. Only a slightly smaller northward extent of the very weak (less than 5 $\frac{m}{s}$) NH summer easterlies can be found in the model in comparison with the ERA-40 data. However,

the timing of maximal vortex strength in the NH is shifted between model and reanalysis. The peak in the model is of similar amplitude as in the reanalysis but delayed by 1-2 months. In the SH the simulated and observed seasonality of the westerlies agrees much better. The only visible difference between model and reanalysis is the underestimation of the wind speeds. In lower latitudes the model also captures the seasonality of the average easterlies very well, but simulates too strong wind speeds. The easterly bias of the model zonal wind at 50 hPa in the tropics is related to the lack of a QBO.

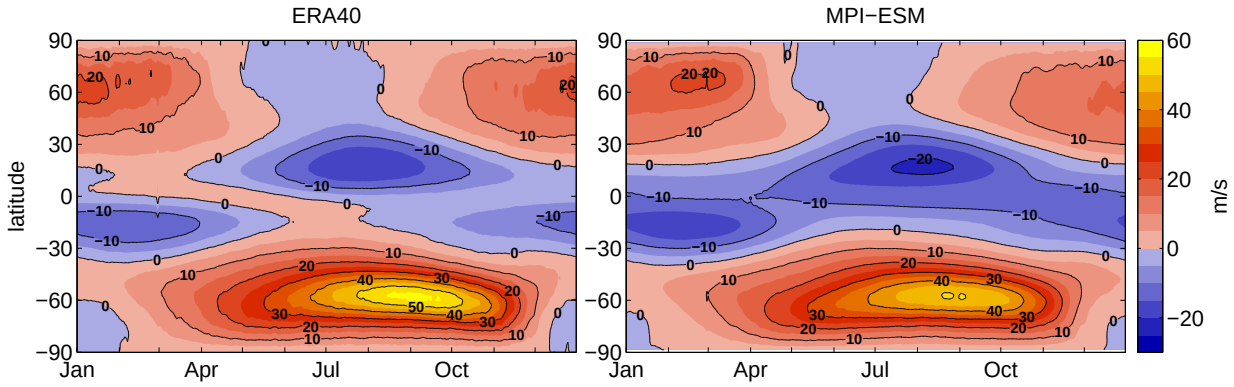

Figure 4.4: Seasonal cycle of daily zonal mean zonal wind speeds ($\frac{\mathrm{m}}{s}$) at 50 hPa in the MPI-ESM CMIP5 runs (left panel) and in the ERA-40 data set (right panel) with color contour intervals of 5 $\frac{\mathrm{m}}{s}$ and black contours with intervals of 10 $\frac{\mathrm{m}}{s}$.

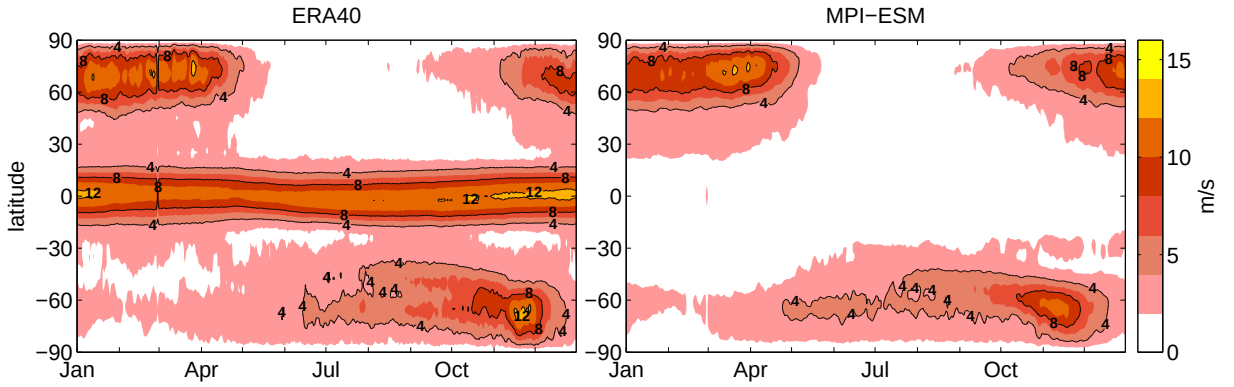

Figure 4.5: Standard deviation of daily zonal mean zonal wind ($\frac{\mathrm{m}}{s}$) at 50 hPa from 1958 to 2000. The left panels show the MPI-ESM CMIP5 results, the right panels the ERA-40 reanalysis with color contour intervals of 2 $\frac{\mathrm{m}}{s}$ and black contours with intervals at 4 $\frac{\mathrm{m}}{s}$, 8 $\frac{\mathrm{m}}{s}$ and 12$\frac{\mathrm{m}}{s}$.

4.1.3 Inter-annual variability of zonal wind

The MPI-ESM simulates a realistic climatological circulation at the surface and at 50 hPa, but quality of the simulation of seasonal variability is also of interest. As a measure for inter-annual variability, figure 4.5 shows the standard deviation of the zonally averaged monthly zonal wind at 50 hPa as a function of latitude and calendar day.

Strong inter-annual variability in 50 hPa zonal mean zonal wind in ERA-40 data (left panel) is located at high latitudes around 70°N and 70°S. There is high variability in the winters of both hemispheres, which represents the variability of the strong westerlies of the polar vortex. In the NH, highest variability can be found in April, with standard deviations of more than 12 $\frac{\mathrm{m}}{s}$. In April the polar vortex breaks up on average and is followed by a reversed stratospheric circulation (easterlies). The high variability during this time describes the inter-annual differences in the timing of that break up. In the NH summer months, during easterly winds, the standard deviation is lower than 2 $\frac{\mathrm{m}}{s}$ in the extra-tropical NH. This is due to the fact that Rossby waves cannot propagate into the stratosphere and cause disturbances during easterlies (section 2.3.4). In the SH the seasonality is similar, with highest standard deviations in November, when the SH polar vortex breaks down. Maximum SH variability is slightly lower than in the NH, the standard deviations does not exceed 12 $\frac{\mathrm{m}}{s}$. The zonal wind variability in the SH high latitudes is slightly higher than in the NH during the hemisphere's respective summer seasons, since the duration of the easterlies in the SH is very short in comparison to the NH. In the tropics variability is higher than 10 $\frac{\mathrm{m}}{s}$ throughout the year with maximal values of more than 12$\frac{\mathrm{m}}{s}$ in November and December. This variability describes the change in sign in the zonal wind speed in the stratosphere above the equator, the QBO.

Model zonal wind standard deviations (figure 4.5, right panel) show good agreement with ERA-40 at high latitudes. In the NH the MPI-ESM variability ist lower in the beginning of the year, but higher at the end of the year and during the season of the vortex breakup. However, differences are only in the range of 2 $\frac{\mathrm{m}}{s}$. The model does not show standard deviations higher than 2 $\frac{\mathrm{m}}{s}$ in the low latitudes, since the QBO is not simulated by the model.

To further investigate the model's ability to simulate a realistic SH circulation, the daily, zonally averaged zonal wind speed at 10 hPa and 60°S between 1958 and 2000 is shown in figure 4.6. Wind speeds at this level and latitude are a good indicator for the evolution of the SH polar vortex. In this figure all ensemble members are displayed, rather than the ensemble mean, to capture the full variability of these wind speeds within the model.

The average observed climatological daily wind speeds (green line, left panel) show easterly winds of -15 $\frac{\mathrm{m}}{s}$ at the 1. January, which become weaker with time. The transition from easterlies to westerlies takes place in the middle of February. Maximal westerlies of 85 $\frac{\mathrm{m}}{s}$ can be found in the SH winter months. In September the wind speeds decrease and on average the transition from westerlies to easterlies takes place in the middle of November. In comparison to the reanalysis, the simulated wind speeds (right panel) have a negative bias of approximately 5-10 $\frac{\mathrm{m}}{s}$ in the months of the strongest westerlies. In other seasons the agreement between the model and reanalysis average wind speed is very high. The timing of the transition between summer and winter circulation are captured extremely well in the MPI-ESM. The average model vortex breaks up only 5 days earlier than in the reanalysis data. This is in contrast to the majority of the chemistry climate models examined in the SPARC CCMVAL-2 report, which showed a delay of the vortex break up (SPARC CCMVal, 2010, figure 4.2).

The observed inter-annual variability, given by the spread of the single year wind speeds (left panel, blue lines) is comparatively small in the beginning of the year. The timing of the transition from summer to winter circulation in early February only shows a spread in the range of 20 days. The strongest variability is found during the months of maximal wind speeds, which occur during SH winter. In the reanalysis, the break up of the vortex takes place between early November and early December.

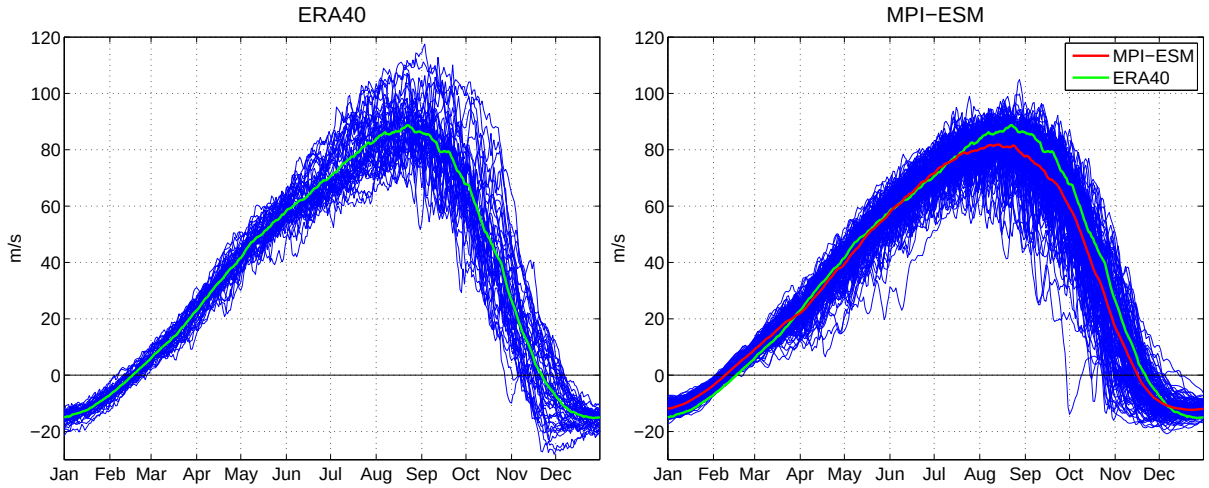

Figure 4.6: Daily zonal mean zonal wind speeds at 10 hPa and 60°S, from 1958 to 2000. The left panel show ERA-40 wind speeds, the right panel shows the MPI-ESM CMIP5 wind speeds. The red lines indicate the daily climatological mean wind speeds.

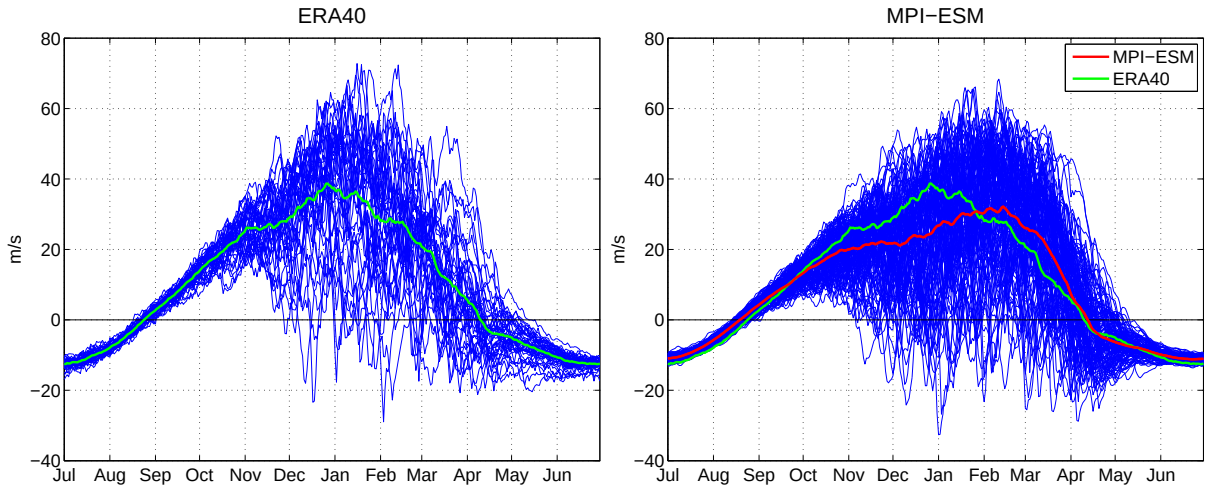

Figure 4.7: Daily zonal mean zonal wind speeds at 10 hPa and 60°N, from 1958 to 2000. The left panel shows the ERA-40 wind speeds, the right panel the MPI-ESM CMIP5 wind speeds. The red lines indicate the daily climatological mean wind speeds.

The model simulates a similar seasonality of the spread (right panel, blue lines), but the spread in the model is higher during the transition periods (spring and autumn), while the inter-annual variability in winter is higher in the ERA-40 data set. The spread during the season of the highest wind speeds in the MPI-ESM results shows differences of up to 60 $\frac{\mathrm{m}}{s}$ between the years, whereas the differences between the years in the reanalysis go up to 70 $\frac{\mathrm{m}}{s}$. The timing of the breakup of the polar vortex is more variable in the MPI-ESM runs. The earliest transitions from westerlies to easterlies are October, apart from one year when the reversal of the circulation already takes place in September. This is in good agreement with SH observations after 2000, which cover the first major stratospheric warming in the SH during September 2002 since regular stratospheric observations began (Krüger et al., 2005). The latest transitions to westerlies take place in December.

Figure 4.7 shows the equivalent zonal wind speed at 60 °N. As in the SH the model and reanalysis agree very well on the average timing of the changes between easterlies and westerlies in the NH. In both data sets the mean transition from summer to winter circulation at 60°N takes place in the middle of August. The vortex breakup can be found in the first half of April and MPI-ESM and ERA-40 only differ by three days on the exact timing. However, the model has a bias in the timing of maximum wind speeds. While the highest wind speeds at this level and latitude in ERA-40 data appear around the turn of the year, the model simulations show a delayed maximum in February.

The spread of the single years' zonal wind speeds shows that the model captures the inter-annual variability as found in the reanalysis data. While the simulated spread is in the range of 5-10 $\frac{\mathrm{m}}{s}$ during the peak of the summer circulation and around the change from easterlies to westerlies, differences between the years in the months of high westerly wind speed are much stronger. In contrast to the SH, for some years easterly wind speeds can be found in the winter months. These are the so-called major mid-winter warmings (Mclnturff, 1978). Therefore, the spread between the wind speeds of the different years goes up to 90 $\frac{\mathrm{m}}{s}$ in the model as well as in the reanalysis. The model simulates earliest major mid-winter warmings in November, whereas in the reanalysis easterlies only appear in the beginning of December.

4.1.4 Simulation of Southern Annular Mode

The MPI-ESM has been shown to produce a reasonable temperature and wind climatology as well as realistic inter-annual variability. Since the forthcoming analysis of the impact of volcanic eruptions focuses on SAM, the SAM climatology of the model is compared to ERA-40. The EOF analysis is applied to anomalies of GPH at 50 hPa and SLP. These first calculations are based on anomalies that include trends (equation 3.2).

Figure 4.8 shows the first EOF pattern in the SH stratosphere and at the SH surface for ERA-40 and MPI-ESM. In the stratosphere the first EOF pattern of simulated 50 hPa GPH anomalies explains 36 % of the variability, 5 % more than in the reanalysis data. Both patterns (figure 4.8, upper panels) exhibit a circular shape around the pole and are of similar amplitude. The first EOFs mainly show the variability of the polar vortex. While the area of high variability attributed to the first EOF extends to approximately 45 °S in the ERA-40 results, the pattern is restricted closer to the pole (around 55°S) in the model data. In the ERA-40 data, the first EOF does not include mid-latitude and subtropical variability. In contrast, the first EOF pattern in the MPI-ESM data includes variability between 20 and 40

°S, which is of the opposite sign to the polar variability and of much lower amplitude. This pattern indicates that the first EOF in the model does not only describe the variability of the SH polar vortex, but also a mass shift between high and mid-latitudes.

The EOF analysis of the surface pressure field in the SH extra-tropics results in a first mode that explains 27 % of the total variance of the monthly SLP anomalies of the ERA-40 data. The EOF pattern (figure 4.8, lower left panel) shows the typical surface SAM pattern, with strongest variability found in the polar regions. The polar variability pattern has an almost annular shape. Around the latitudes of 50-55°S and north of 30°S the first modes describes almost no variability at all. A wave-structured band of variability of the opposite sign between the latitudes 30° and 50°S surrounds the polar part. The centers of this mid-latitude variability are around 170 °W and 80 °E. However, values in this area are mostly less than a third of the maximal variability above the Antarctic continent. The annular rings of variability describe the latitudinal shift of atmospheric weight.

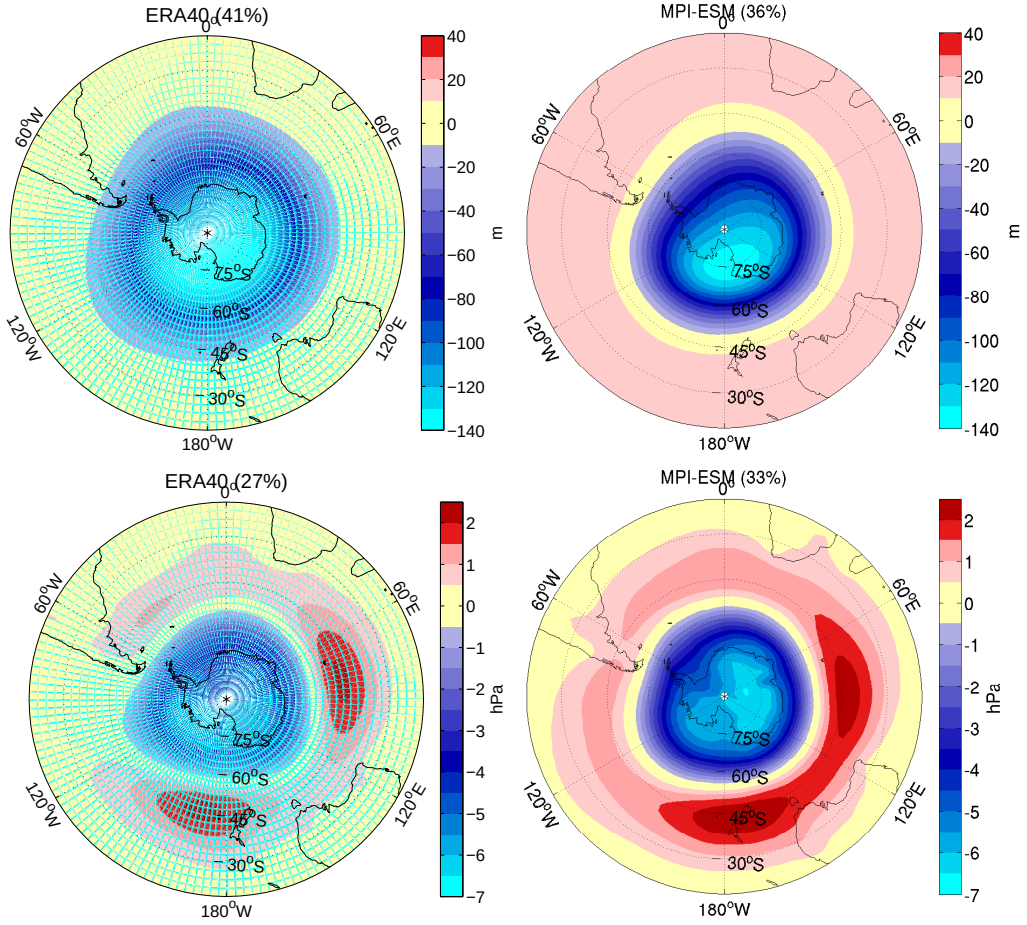

Figure 4.8: 1st EOF pattern of monthly mean GPH at 50 hPa (m) in the upper panels and monthly mean SLP (hPa) in the lower panels based on anomalies from the full time series mean (20°S-90°S). Left panels show the ERA-40 pattern (1958-2000), right panels the MPI-ESM CMIP5 historical experiment data (1850-2000). EOFs are scaled that the associated time series has unit variance.

The equivalent pattern of the MPI-ESM SLP anomalies is shown in 4.8 (lower right panel). Here the first EOF mode explains 33 % of the variability. The polar variability that is allocated to the first mode, has a similar shape as within the reanalysis results, but is of a stronger amplitude is (factor of approximately 0.2) than in the reanalysis. The wave structure of the mid-latitude ring of variability is captured well in the model, but zonally more symmetric than in the ERA-40 pattern.

Overall the first EOF pattern look similar in the model and reanalysis data. This suggests a realistic representation of the SAM index in the MPI-ESM. If the definition following equation (3.3) is used to calculate the anomalies of SLP and GPH, the pattern (not shown) are almost identical and also the variance explained by the first EOF pattern is of similar magnitude.

The normalized time series corresponding to the described MPI-ESM EOF pattern (the SAM indices) are shown as annual averages in figure 4.9. The simulated stratospheric SAM index varies between values of -0.7 to 0.7 and shows strong inter-annual variability. The single ensemble members don't agree too well, with a standard deviations among the runs (gray shading) of the same magnitude as the index itself, which had to be expected since the SAM describes mostly internal variability of the atmosphere (Thompson, 2007). The index shifts towards more positive values from the 1970s on, reaching a maximum of 1.23 in 1993. Figure 4.10 shows the seasonal average SAM index from 1850 to 2000 separated by seasons. It becomes obvious that the trend of the second half of the 20th century can mostly be attributed to the SH spring (SON) and summer (DJF). This agrees well with observational and previous model studies (Thompson et al., 2000; Gillett and Thompson, 2003; Thompson and Solomon, 2002). It is related to increased ozone depletion in SH spring (ozone hole), when sunlight returns to the polar regions after winter, which has a direct cooling impact on the polar stratosphere in spring and therefore causes a positive trend in spring SAM. The spring index also shows the highest inter-annual variability, which is related to the fact that it is the season of highest

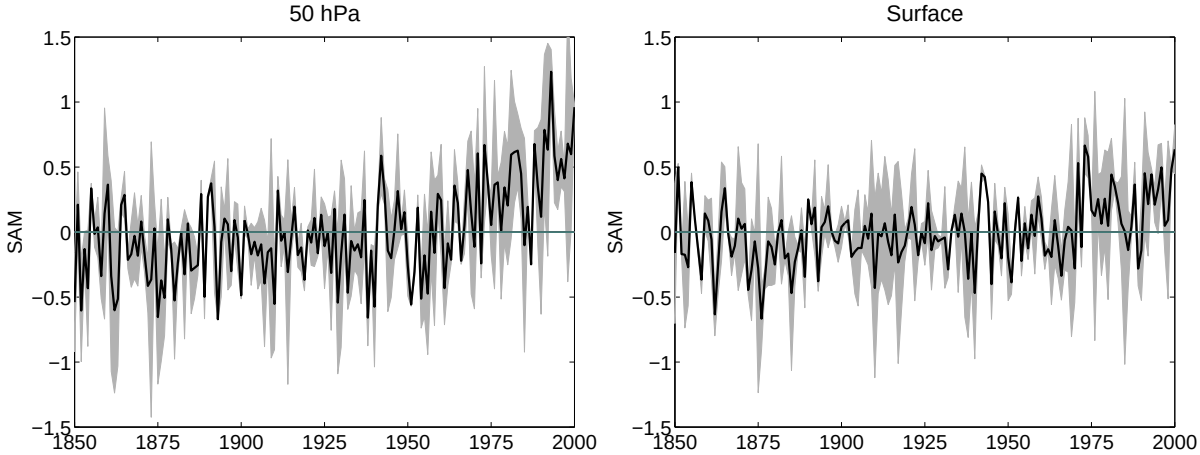

Figure 4.9: Time series of annual SAM at 50 hPa (left panel) and at the surface (right panel) based on monthly anomalies from the full time series mean as simulated by the MPI-ESM (black line is ensemble mean, gray shading indicates one standard deviation among the runs). Indices are calculated using the EOF-based version.

wave activity (Randel, 1988) and the variability in the timing of the break up of the polar vortex. A feedback between ozone induced cooling, polar vortex strengthening and weakened vertical wave propagation was suggested by Thompson et al. (2000) to be the reason for the summer trend. As CMIP5 historical runs include the GHG and ozone trends, volcanic and solar forcing in phase with observations, the model seems to be capable of simulating a realistic response to anthropogenic and naturally induced climate changes. However, the model does not simulate the autumn (MAM) trend, that was reported by Thompson and Solomon (2002). This trend is linked to increased ozone depletion in summer, which also affects the following autumns, and it is not clear why the model does not capture this feature.

The simulated tropospheric index (figure 4.9, left panel, black line) shows similar variability and ensemble spread as in the stratosphere. The most striking difference between the layers is the less pronounced trend. There is no season where the simulated surface SAM trend is

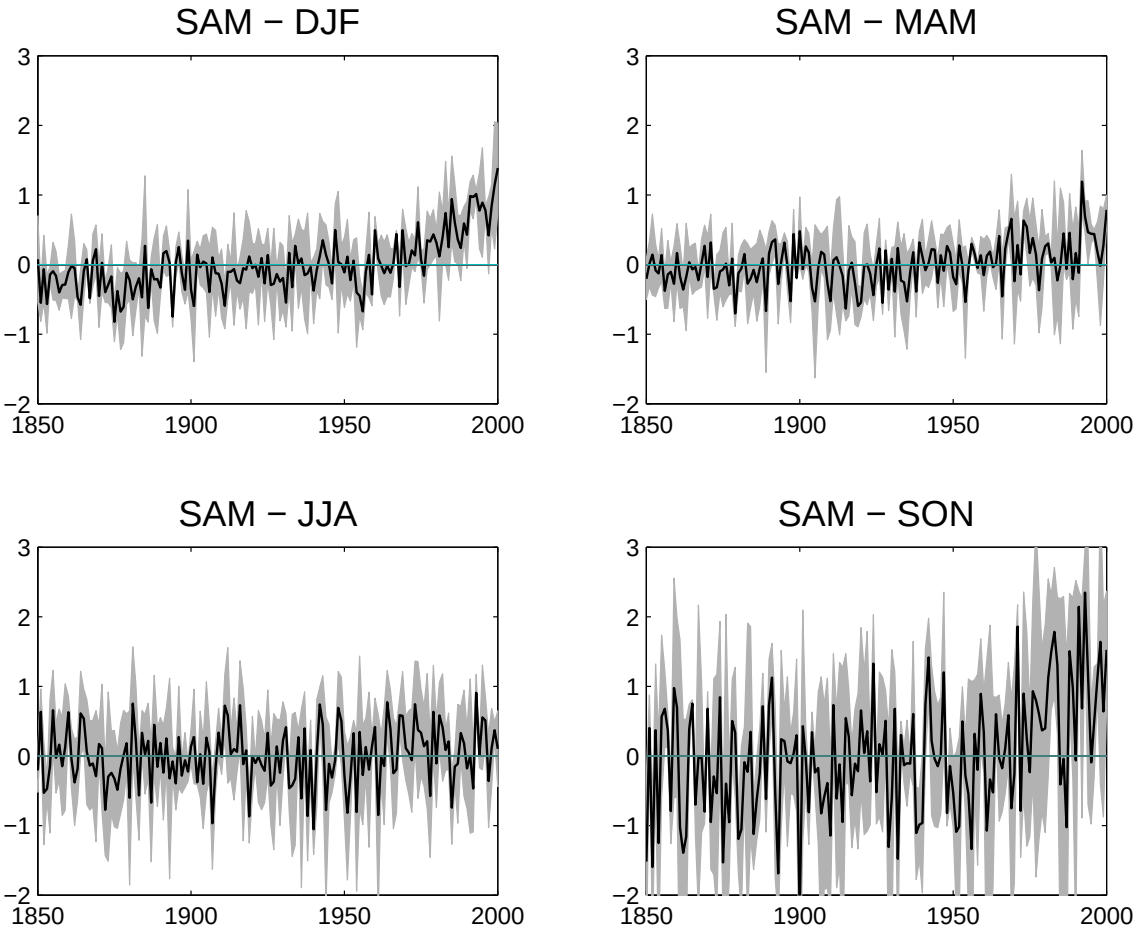

Figure 4.10: Time series of SAM at 50 hPa in the 4 seasons based on monthly anomalies from the full time series mean as simulated by the MPI-ESM CMIP5 historical experiment (black line is ensemble mean, gray shading indicates one standard deviation among the runs). Indices are calculated using the EOF-based version.

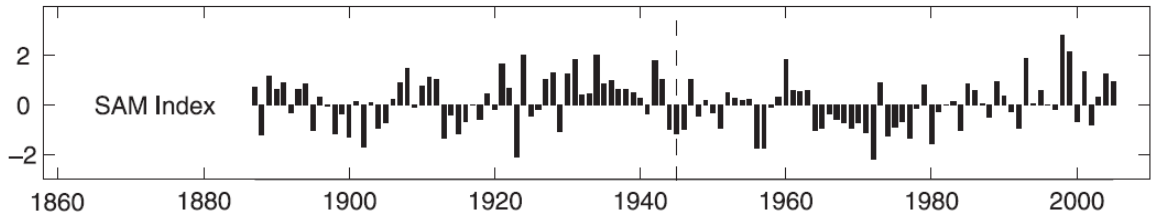

Figure 4.11: Annually averaged, station-based surface SAM index based on monthly SLP anomalies from 1884 to 2005, from Visbeck (2009)

more pronounced (see appendix, figure A4), which is in agreement with findings of Thompson et al. (2000), who examined NCEP/NCAR reanalysis data for the time period from 1968 to 1997. The comparison with ERA-40 data (A2) shows that the values are realistic. An observational station-based index from Visbeck (2009) is shown in figure 4.11. This time series shows a similar shift from positive to negative values in the last third 20^{th} as found in the MPI-ESM and ERA-40 results. The amplitude of the index in generally larger for the station-based index by Visbeck (2009). The model results do not display the striking decadal variability seen in the Visbeck index, but rather shows the trend in the late 20^{th} century to be beyond the natural variability.

For the analysis of the SAM index after volcanic eruptions, not these time series are used, but the detrended ones (not shown) based on anomalies following equation (3.3). Those detrended time series show very similar inter-annual variability of the SAM index, although the trend is removed.

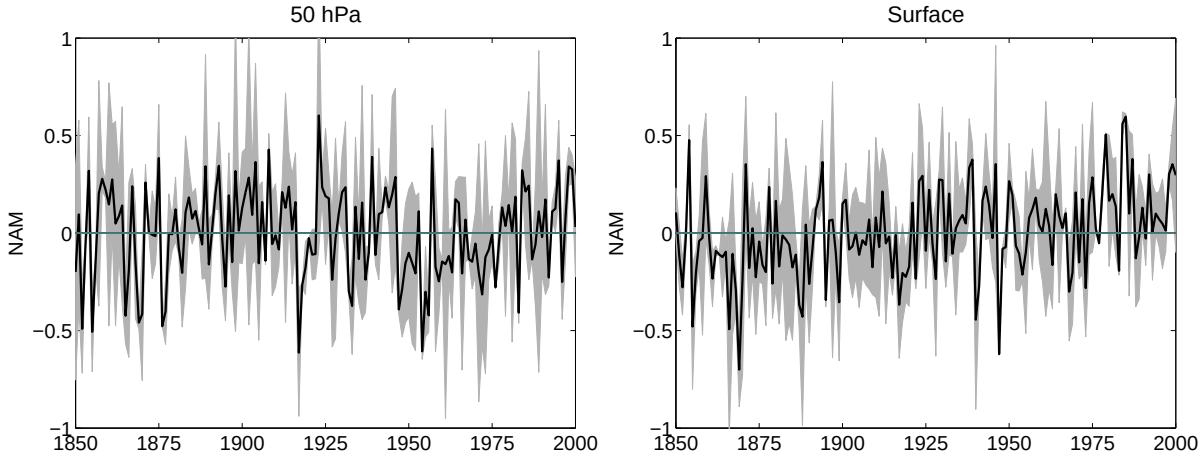

Figure 4.12: Time series of annual stratospheric NAM at 50 hPa (left panel) and the surface NAM (right panel) based on monthly anomalies that include long-term trends as simulated by the MPI-ESM (black line is ensemble mean, gray shading indicates one standard deviation among the runs) and in the ERA-40 reanalysis (red line). Indices are calculated using the EOF-based version.

4.1.5 Simulation of Northern Annular Mode

Figure 4.12 shows the annual averages of the simulated NAM indices for the stratosphere and at the surface. These time series are based on anomalies calculated by equation (3.2) and include possible trends.

In the stratosphere a slight increase in the annual SAM index can be found in MPI-ESM towards the late 20thcentury, which agrees with ERA-40 (appendix, figure A6). When differentiating between the different seasons (figure 4.13) it becomes obvious that the increase of the simulated NAM at 50 hPa since the 1980s can be found in all seasons except NH spring (MAM). This is in sharp contrast to observational findings of Thompson et al. (2000), who showed the most pronounced shift towards negative 50 hPa GPH anomalies and therefore a positive NAM in NH spring. This may be due to the fact that the NH winter seasonality in the model is shifted towards spring compared to observations, as the seasonality of the zonal wind at 60°N and 10 hPa shown (figure 4.7).

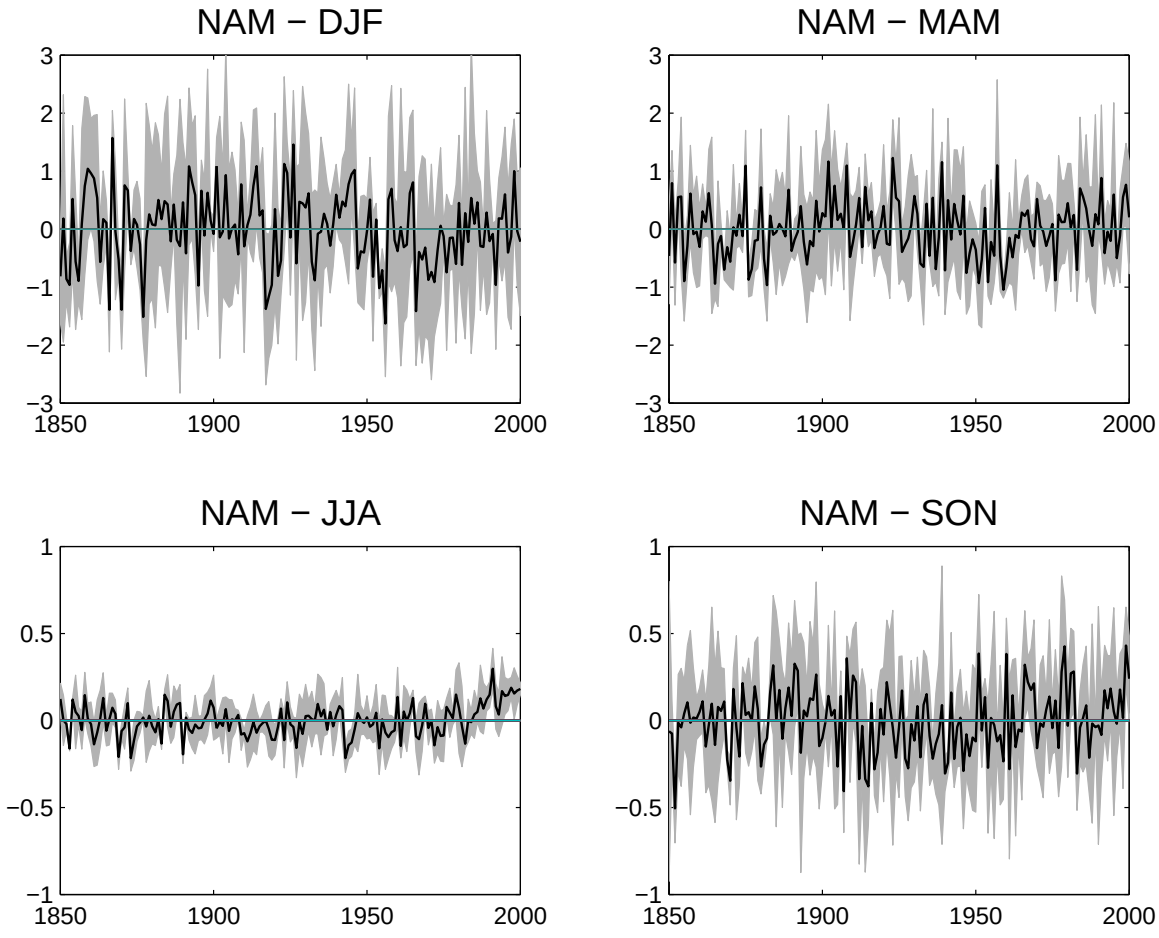

Figure 4.13: As figure 4.10 for the NAM index.

In figure 4.13 is also becomes clear that the amplitude of the stratospheric NAM variability in the MPI-ESM varies strongly between the different seasons. The NH winter NAM shows values between -1.5 and 1.5, while the summer variability is only in the range of a quarter of the winter variability. These differences in amplitude show, that the definition for the NAM as used in this study is not the most appropriate. A more suitable approach would be the application of the EOF analysis separated by seasons. However, the EOF-based definition of the SAM index includes all seasons and the main focus of this study is the SH. For comparability between the hemispheres and following the definition of the SAM index by CPC (2012), identical methods for calculating NAM and SAM are used here. Using this method an overestimation of NAM signals in the post-volcanic winters has to be expected, since the amplitude of the winter NAM is large in comparison to the other seasons.

No obvious trend is found in the simulated annual surface NAM. The seasonal surface NAM indices (appendix, figure A8) show a positive trend in the MPI-ESM surface NAM in NH autumn. This is in contrast to results of Thompson et al. (2000), who found the strongest positive trend within the NCEP/NCAR reanalysis data in NH winter.

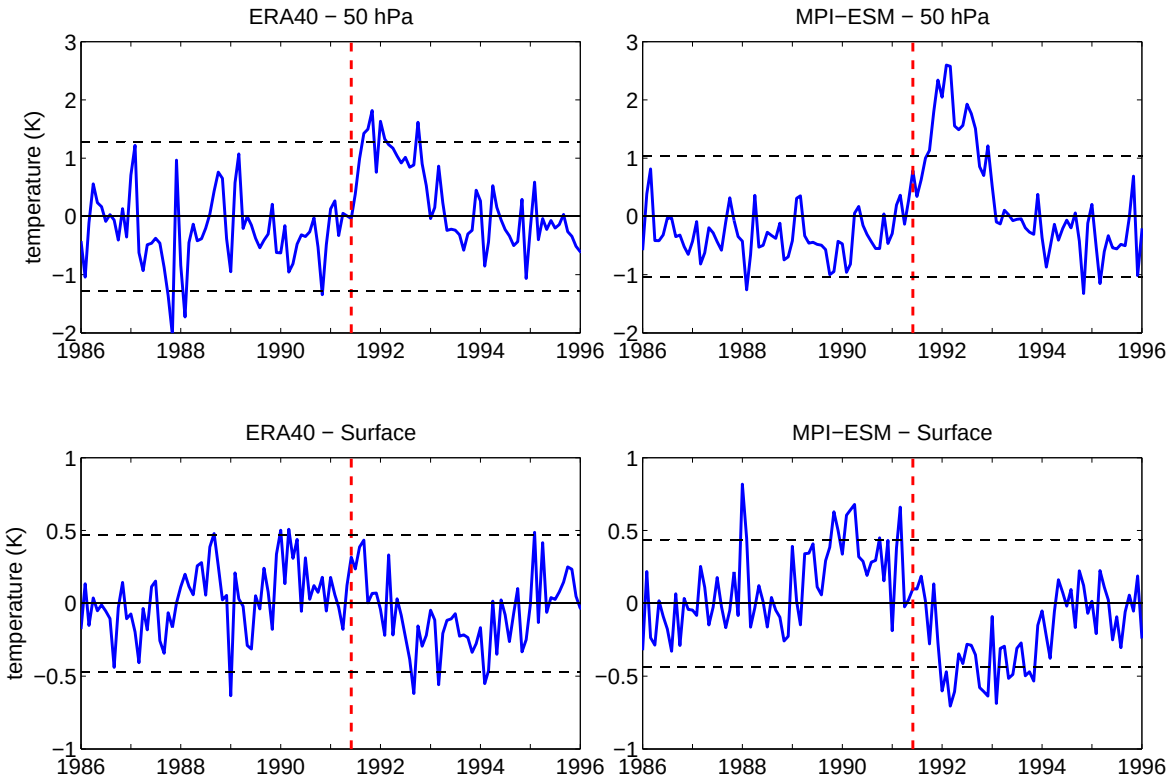

Figure 4.14: Global mean monthly temperature anomalies at 50 hPa (upper panels) and at the surface (lower panels) from 1986 to 1996 in ERA-40 (left panels) and MPI-ESM CMIP5 historical runs (right panels). Anomalies are calculated excluding long-term trends. Red line marks the eruption of Mount Pinatubo in June 1991. Dashed black line marks the significance line on 95% level (two times the standard deviation of the full time series).

4.2 Response to volcanic eruptions

In the following sections anomalies in temperature and the annular modes after the volcanic eruptions are analyzed. All anomalies are calculated following equation (3.3) in order to exclude long-term trends.

4.2.1 Case study: Mount Pinatubo eruption (June 1991)

The indirect dynamical response of the atmosphere to volcanic eruptions is the product of direct radiative perturbations. Therefore, the model has to be able to simulate realistically the temperature response to allow for a realistic SAM response to volcanic eruptions. As Pinatubo in 1991 displays the strongest AOD forcing in the time period covered by ERA-40, it is used as a case study to examine the model's temperature response to the prescribed aerosol forcing.

Stratosphere Figure 4.14 (upper panels) shows the monthly temperature anomalies at 50 hPa around the eruption of Mount Pinatubo. In the ERA-40 data (figure 4.14, upper left panel), there are positive anomalies of up to 1.8 K following the eruption of Pinatubo until 1993. Only a fraction of these anomalies crosses the significance line. These ERA-40 values are slightly higher than the results from microwave sounding unit satellite observations, that showed a maximal warming of the lower global stratosphere of 1.5 °C in August 1991 (see figure 5, Robock, 2000). In the MPI-ESM simulations (figure 4.14,upper right panel) the positive stratospheric global temperature anomalies last for approximately the same time period as in ERA-40 but the anomalies are higher (up to 2.6 K) and significant throughout most of 1992.

To investigate these stratospheric temperature anomalies in more detail, the horizontal distribution of the monthly temperature anomalies is examined. A direct radiative effect of the volcanic aerosols can mainly be seen in the lower-latitude temperature anomalies, where aerosol concentrations are higher than in high latitudes (see section 2.5). Temperature changes at high latitudes are considered to be primarily the result of dynamical changes or ozone effects. Therefore the analysis of temperature responses to the eruption of Mount Pinatubo in the lower stratosphere and at the surface is concentrated on low latitudes.

Figure 4.15 shows 50 hPa zonal mean temperature anomalies following the eruption of Mount Pinatubo. In the stratosphere the reanalysis data (upper left panel) shows a warming of the subtropical regions after 1- 2 months, while the strongest signal in the tropics appears during NH winter 1992/93 with a significant maximal amplitude of approximately 5 K. In the first months after the eruption there is even a slight cooling in the tropical stratosphere. The reason for this counter intuitive result can be found equatorial zonal winds. Mount Pinatubo erupted during the easterly phase of the QBO, which is related to a cooling of the lower and middle stratosphere (Baldwin et al., 2001). After August of 1992, when the QBO above the equator changed sign, the volcanically induced warming of the stratosphere appears in the ERA-40 temperature anomalies. In the NH polar regions, a stratospheric cooling at the beginning of NH winter, followed by a warming, is present in the two first NH winters, but only in the late first winter the warming of sub-polar areas is significant with amplitudes of up to 7 K. In the SH polar stratosphere significant warm anomalies of up to 8 K are found in SH spring of the first two years after the eruption. Crooks and Gray (2004) examined the ERA-40 data set with respect to temperature anomalies after volcanic eruptions and found a

cooling of the upper tropical stratosphere in addition to warm anomalies in the polar lower stratosphere. They suggest these signals to be linked to a strengthening of the BDC, which might be driven by modified equatorial upwelling.

The model (figure 4.15, upper right panel) also shows significant warming of the middle stratosphere in the tropics and subtropics. Instead of the initial cooling of the tropical stratosphere, the warm anomalies in this regions exist throughout the first 2 years, since the QBO is not simulated by the model. A significant maximal amplitude of more than 4 K is found at the equator in May 1992, 11 months after the initial AOD signal. In the NH high latitudes the warming in the first NH winter after the eruption is reproduced by the model with values up to 9 K.

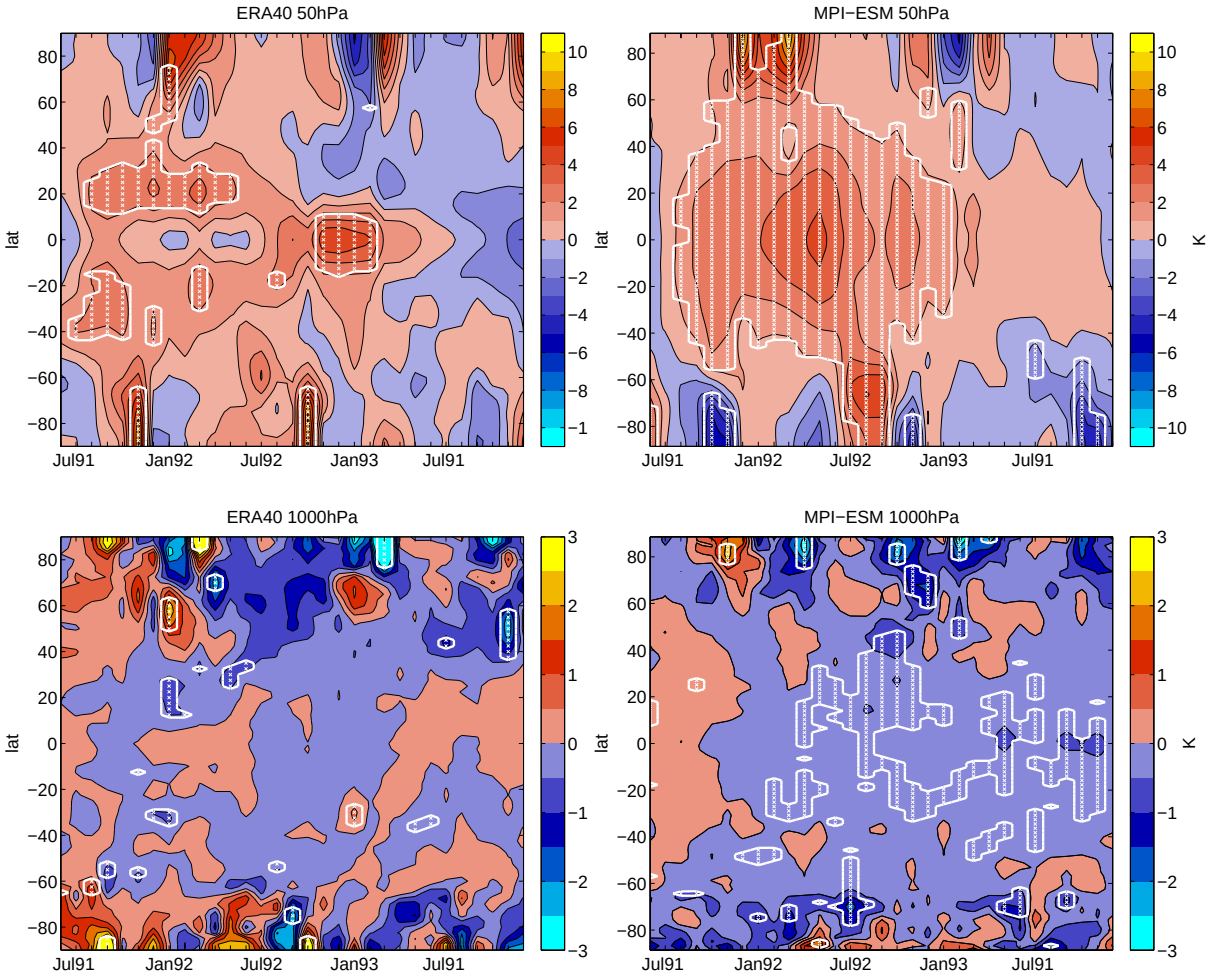

Figure 4.15: Monthly zonal mean temperature anomalies (K) at 50 hPa (upper panels) and 1000 hPa (lower panels) in ERA-40 (left panels) and the MPI-ESM CMIP5 historical runs as ensemble mean (right panels) in the 2.5 years following the eruption of Mount Pinatubo in June 1991. Grey hatching marks anomalies larger than two times the standard deviation of the full time series (significant on 95% level).

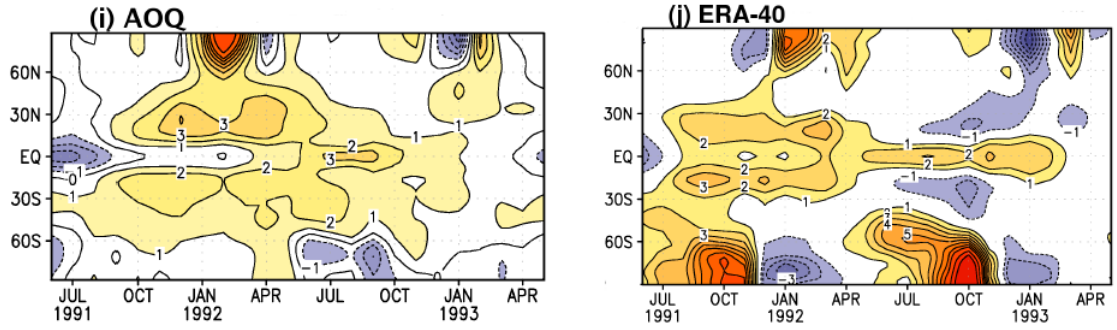

Figure 4.16: Lower stratospheric temperature anomalies at 30 hPa (K) for ECHAM5 with combined aerosol, ocean and QBO forcing (AOQ) and ERA-40. Contours are at 1K intervals. The anomalies in the latitudinal belt of 50N-50S are statistically significant at 99% level from Aug1991 to Apr1993. From Thomas et al. (2009a).

In the SH high latitudes model and reanalysis show less agreement. Instead of the spring warming found in the ERA-40 results, MPI-ESM simulates a significant cooling of 5-6 K in SH summer and spring, which starts in July 1991 and lasts for 3 months. Such a cooling in the model data is present in all three SH springs after the eruptions and with a smaller amplitude (not significant) also in the first autumn. A positive stratospheric temperature signal is found in the SH winter of 1992, when the whole of the SH exhibits significant positive temperature anomalies, with a maximum of ~5 K around 65°S. These differences between MPI-ESM and ERA-40 suggest that the stratospheric SAM response to the eruption of Pinatubo differ in the model and the reanalysis. Figure 4.16 shows the stratospheric temperature response at 30 hPa to the eruption of Mount Pinatubo as simulated by the ECHAM5 models with boundary conditions that include observed SST and observed QBO in comparison with ERA-40 data. It becomes clear that a realistic QBO and SST forcing is necessary to simulate the observed spatial temperature pattern in the tropical stratosphere. However, even with these effects included the model does not capture the warming of the polar lower stratosphere in SH spring of 1991 and 1992 that is found in the ERA-40 data.

Surface The global mean monthly surface temperature anomalies in the ERA-40 data (figure 4.14,lower left panel) surface temperature anomalies are negative for about two years from early 1992 and to early 1994. The monthly values within this time period vary between -0.1 and -0.6 K and are hardly significant, the annual average (not shown) gives a maximal negative anomaly of -0.21 K in 1993. These finding slightly overestimate the global surface cooling after Pinatubo in comparison to the results of Thompson et al. (2009), who analyzed the Hadley Centre's Sea Surface Temperature data set and found global surface cooling up to -0.3. In the MPI-ESM data (figure 4.14,lower right panel) the global surface cooling is more pronounced, showing negative temperature anomalies from 1992 to 1994, that reach maximal and significant values up to -0.7.

The meridional distribution of the zonal mean surface temperature anomalies after the eruption of Mount Pinatubo is shown in figure 4.15 (lower panels). At the tropical surface neither the MPI nor the reanalysis data show strong temperature signals. In the reanalysis the cooling is limited to the subtropics and only significant in the first NH winter. This lack

of response in the surface temperature at the equator is most likely due to the fact that the reanalysis data includes the warming effect of the 1991/1992 El Niño. The El Niño signal is strongest in the tropical west Pacific SST and therefore suppresses a possible cold signal in the average of the lower latitudes. On a global scale the El Niño effect on surface temperature has been shown to mask the volcanic cooling signal (Robock and Mao, 1995). In the January 1992, there is a NH a significant warm anomaly of 2.5 K around 60 °N in the reanalysis data. This warming is the zonally averaged signal of positive temperature anomalies over the North American continent, Scandinavia and Siberia (appendix, figure A11). The continental warming pattern has been found after the eruption of Mount Pinatubo as well as other volcanic eruptions in previous studies (Robock and Mao, 1992; Robock, 2000; Thomas et al., 2009a).

The MPI-ESM simulates a small, but persistent tropical and subtropical cooling, starting 3 months after the Mount Pinatubo eruption and lasting for more than 2.5 years. Since here the ensemble mean is shown, possible ENSO signals are most likely evened out and a stronger temperature response than in the reanalysis data has to be expected. However, anomalies do not exceed 1 Kelvin in these regions and are hardly significant. The small tropical surface temperature signals already suggests that the effect of a weakened horizontal surface temperature gradient might not be of strong influence in either the MPI-ESM simulations or the ERA-40 reanalysis. The signal of the zonally averaged winter warming pattern in the NH mid-latitudes can not be found in the MPI-ESM simulations.

4.2.2 Southern Annular Mode response

The SH extra-tropical circulation response to all 10 eruptions in the MPI-ESM and all 5 eruptions in ERA-40 are shown in figure 4.17 as monthly SAM indices. The SAM responses to volcanic forcing are considered significant at the 95% confidence level when the ensemble mean SAM index is greater than two times the standard deviations of the full ensemble mean SAM index time series. A similar significance threshold is defined for composite means by dividing the two standard deviations of the ensemble mean SAM variability by the square root of the number of composite members. However, the significance of the results has to be regarded with caution. A 5% false discovery rate has to be expected for values that cross these significance lines. Since the figures showing post-volcanic anomalies all contain at least 50 data points, it has to be expected that a handful of anomalies which exceed the 95% level are simply outliers due to natural variability, not because of anomalous post-volcanic dynamics. This holds especially for peaks that are not persistent but only show for one time step.

4.2.2.1 Stratospheric SAM

Monthly index Figure 4.17 shows the monthly mean stratospheric SAM indices as a function of month after eruption. The eruptions are given by the legends and differ for the MPI-ESM and ERA-40 due to the shorter available time series of ERA-40.

The monthly stratospheric SAM in ERA-40 (4.17 upper left panel) shows no consistent signal after all eruptions, but the majority of the post-volcanic SAM indices are negative during months 5 to 12 after the eruptions, indicating a weakening of the SH polar vortex. The strongest stratospheric responses can be found 5 months after the eruptions of Fernandina and Pinatubo, with a significant SAM index of -3.4 and -2.7 respectively. However, since the eruption of Fernandina only displayed a weak AOD signal (figure 3.1) the strong negative

signal after this eruption is unlikely to be due to volcanic forcing alone. Also after the eruption of Fuego, which only showed a weak AOD signal (figure 3.1), there is a significant negative SAM of -2.6 after 10 months. The eruption of El Chichon does not produce a significant negative SAM index, but there is a sharp drop in the index after 5 months. The composite of all 5 eruptions shows a barely significant negative SAM of -1 6 months after the eruptions.

In the MPI-ESM the response of the stratospheric SAM is even less clear (figure 4.17, upper right panel). In the model atmosphere there is a high positive SAM 4 and 5 months after the eruption of Mount Pinatubo (values around 1.7). These are SH spring months. Also 6 months after El Chichon (October 1982) a significant positive index of 1.3 is reached and after another year there is an even stronger signal of 1.7. However, there are also significant negative anomalies. 14 months after the Pinatubo eruption (August/September 1992) the MPI-ESM simulates a significant negative stratospheric SAM of -1.5.

Seasonally averaged index Since there seems to be a strong seasonality to the simulated stratospheric impacts, the seasonally averaged SAM indices are composited by season after the eruption.

The seasonally averaged stratospheric SAM in ERA-40 is shown in figure 4.18 (upper left panel). The stratospheric seasonal SAM indices show no clear seasonality in the negative SAM anomalies, but rather a drop in the index soon after the eruption. While the negative stratospheric SAM anomaly in the first spring after the Pinatubo eruption is obvious in the seasonal average with a SON index of -1.7, the SAM index after Fernandina does not show a significant signal when seasonally averaged. Instead a persistent negative stratospheric SAM index is found after the eruption of Fuego, with values around -1 throughout most of the year following this eruption. Despite of the theoretical concept of the impact of volcanic eruptions on the extra-tropical circulation (see section 2.3.2), there is no significant positive stratospheric SAM, indicating a strengthening of the polar vortex, after any of the eruptions in the reanalysis data. The only significant signal in the composite of the 5 eruptions, which crosses the significance line, is a negative SAM of -0.75 in the first SH summer (DJF).

The stratospheric SAM index after the three strongest eruptions (Krakatau, El Chichon, Pinatubo) in the model are shown in figure 4.18 (upper right panel). It becomes clear that the strongest positive SAM responses at 50 hPa can be found in SH spring. After Pinatubo the index peaks significantly in the springs of the first and third year after the eruption with a maximal SON (September-October-November mean) value of 1.5. A weaker positive signal (index of 0.9) can be found in the first autumn after the Pinatubo eruption. The strongest response after El Chichon takes place in spring of the second year after the eruption (index of 1.4). These findings support the results of Karpechko et al. (2010), who analyzed the SH circulation response to the eruptions of El Chichon and Mount Pinatubo in the climate models of the CMIP3 project. They found a strengthening of the 50 hPa westerlies in spring after the El Chichon eruption and in SH spring and autumn after the eruption of Mount Pinatubo. Although the timing of the positive stratospheric SAM after these two eruptions does not completely agree with the MPI-ESM results, which show the strongest El Chichon related positive index only in second spring after the eruption, the seasonality of the simulated volcanic impact is confirmed by the results of this study.

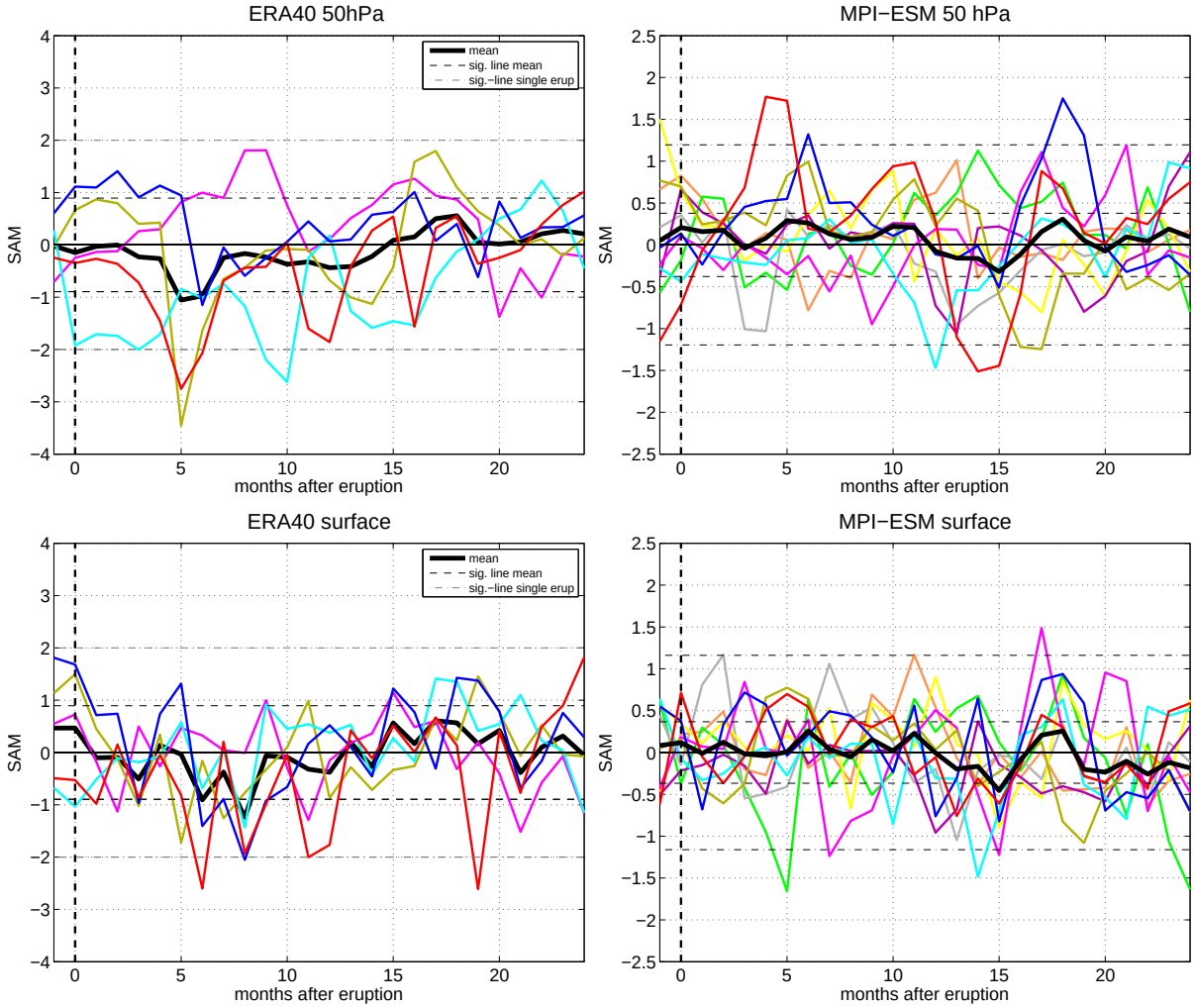

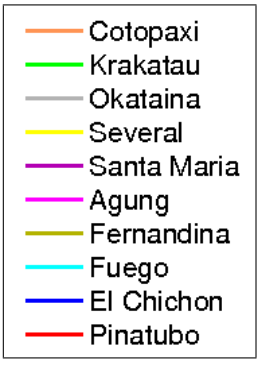

Figure 4.17: Monthly SAM index at 50 hPa (upper panel) and at the surface (lower panels) in the two years following 5 volcanic eruptions in the ERA-40 data (left panels) and 10 volcanic eruptions in the MPI-ESM historical simulation ensemble mean (right panels).

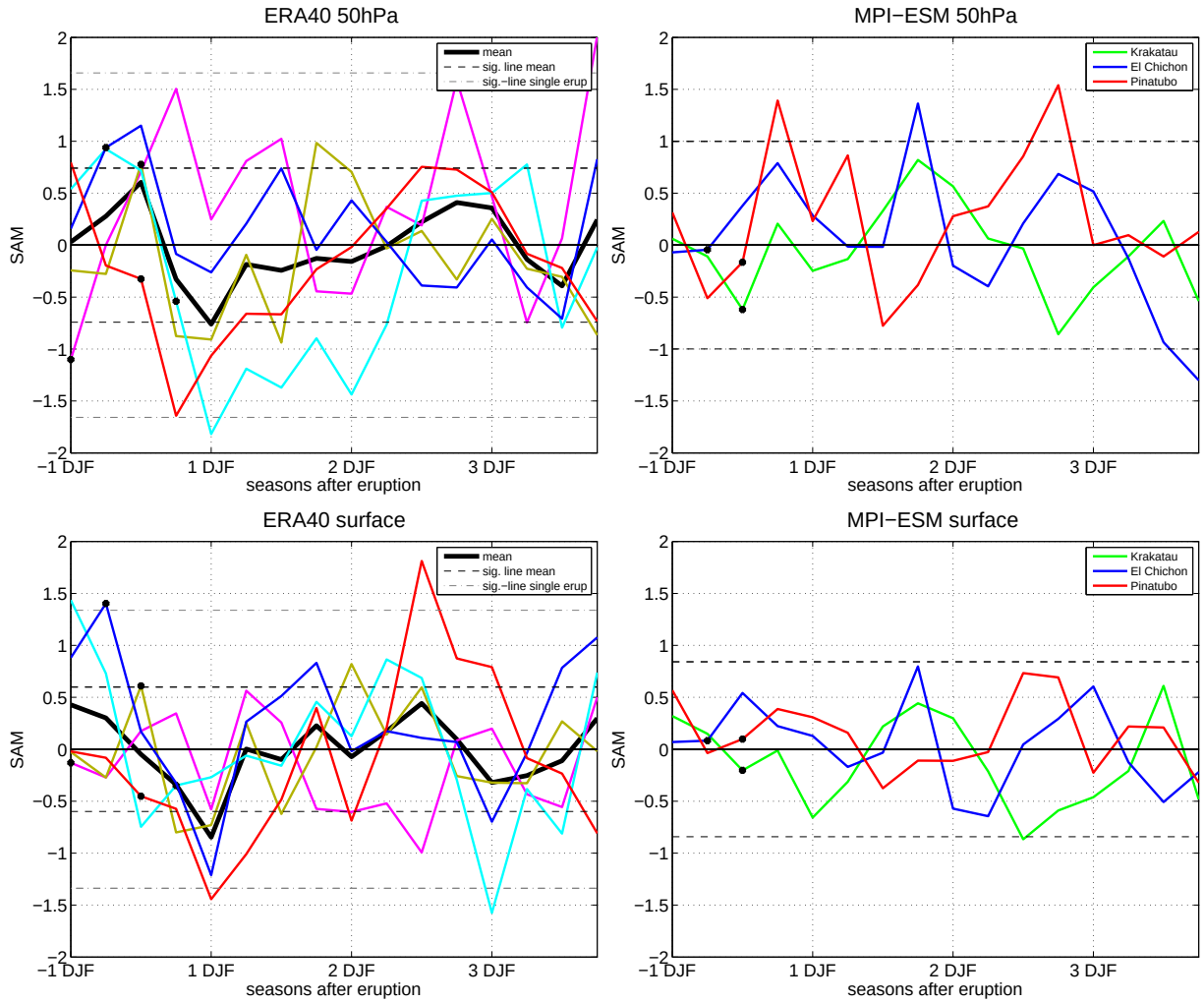

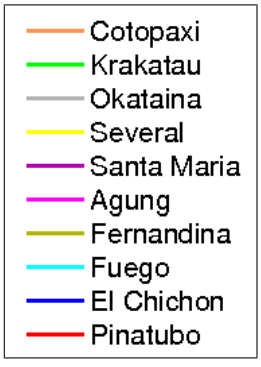

Figure 4.18: Seasonally averaged SAM index at 50 hPa (upper panels) and at the surface (lower panels) in the three years following all 5 covered eruptions in the ERA-40 data (left panels) and the three strongest volcanic eruptions for the MPI-ESM CMIP5 historical simulations ensemble mean (right panels), dashed line marks the 95% significance line, black dots mark the season of eruption

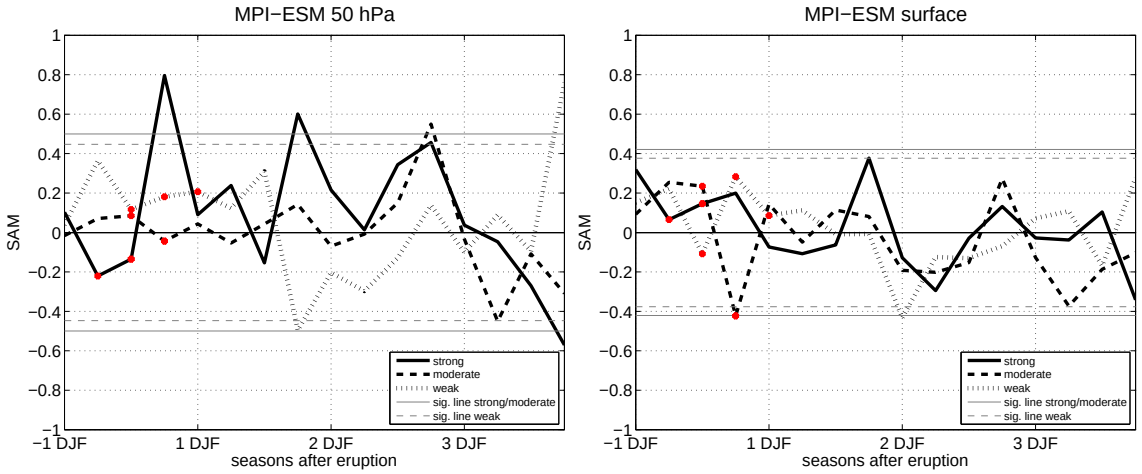

Figure 4.19: Composites of different strength of the volcanic eruption for the seasonally averaged SAM index in the three years following the 10 volcanic eruptions in the ensemble mean of the MPI-ESM CMIP historical experiment. The time series are composited with respect to the weak (4 composite members), moderate (3 composite members) and strong (3 composite members) volcanic signals. The left panel shows the SAM at 50 hPa, the right panel the surface SAM.

To examine whether the seasonality of a simulated response is linked to the strength of the AOD signal after the eruption, composites of the SAM after the eruptions are produced with respect to their magnitude category (weak, moderate and strong as defined in section 3.1.4). Figure 4.19 (left panel) shows these composites the stratospheric SAM for three years following the eruptions. A significant positive SAM anomaly of 0.8 in the first spring after the strong eruptions is most striking. In the second spring after the strong eruptions there is a weaker, but still significant SAM of 0.6 and even in the third spring the SAM index reaches a SAM index of 0.45. The SAM index after moderate eruptions is close to zero for the first 7 seasons after the eruptions and only reaches a significant value after more than two years, which is not assumed to be of volcanic forcing. The weak eruptions are followed by a significant negative SAM index of 0.5 in the second spring after the eruptions. This signal is the opposite sign to the strong eruptions and unlikely to be of volcanic origin. These results highlight the MPI-ESM only shows a stratospheric circulation response in the SH to volcanic eruptions that are followed by a strong AOD signal in comparison to average volcanic AOD signals in the examined time series.

4.2.2.2 Surface SAM

Monthly index In the reanalysis data (figure 4.17 lower left panel) there are no positive SAM indices for the months 6 to 8 after all eruptions except Agung. This is in contrast to findings of Marshall et al. (2003), who used a station based SAM index and found a negative spike in the surface SAM after the eruption of Agung. In the following chapter reasons for such differences between reanalysis results in this study and in previous publications are discussed. The only significant signals in the ERA-40 surface SAM can be found after the eruptions of El Chichon and Mount Pinatubo. While after El Chichon there is a positive peak of 1.2 in

SAM after 5 months (September 1982), before the significant minimum of -2 after 8 months (December 1983), there is a fast and strong negative SAM response of -2.5 6 months after Pinatubo (December 1991). Also 11 and 19 months after the Pinatubo eruption (May 1992 and January 1993) significant negative anomalies are observed. The negative surface SAM anomalies after the eruption of Pinatubo mostly appear simultaneously or slightly shifted to a drop in the stratospheric SAM indices, indicating a coupling of surface and stratosphere. The composite mean of the 5 eruptions within the time period covered by ERA-40 shows a significant negative SAM at the surface after 6 and 8 months.

In the MPI-ESM there is no clear common signal for the different eruptions at the surface (figure 4.17, lower right panel). After the majority of the eruptions, no significant anomaly appears. The strongest SAM signal is a negative SAM of -1.6 5 months after the eruption of Krakatau, which agrees with the fact that it showed the strongest signal in the global AOD. Another eruption after which strong anomalies in the zonal circulation appear is Agung in 1963. 7 months and 15 months after the eruption there are significant negative SAM indices of -1.2, while 17 months after the eruption the index peaks with a positive value of 1.5. This positive signal is also found in the stratosphere, only with a smaller amplitude (SAM index of 1.1). 14 months after the eruption of Fuego significant negative index of 1.5 is present at the surface as well as in the stratosphere. Therefore most of the volcanic responses tend to be negative values, which is also visible in the average of all 10 eruptions with a significant SAM index of -0.5 after 15 months. However, due to the 5 % false discovery rate and the fact that the the signals short-lived, none of the SAM anomalies are considered to actually be significant, so if there is a surface response to volcanic eruptions in the MPI-ESM, it is too weak to clearly identify it in the noisy atmospheric conditions.

Seasonally averaged index In the seasonal averages (figure 4.18) the differences in surface signals to the volcanic eruptions in reanalysis and model simulations become even clearer. There are negative SAM indices in the first summer after all 5 eruptions in the reanalysis data (4.18, lower left panel), leading to a significant average index of -0.8. The strongest signal in the first summer is found after the eruption of Mount Pinatubo with a SAM index of -1.4. Another significant negative SAM index appears in the third SH summer after the eruption of Fuego (index of 1.5). However, there also appears a strong positive post-volcanic SAM signal. Two winters after the eruption of Mount Pinatubo there is a significant SAM index of 1.8. Since there is no concurrent in the stratosphere, this signal is probably not related to volcanic-induces changes of the SH dynamics. While the amplitudes of the surface SAM in the reanalysis after the volcanic eruptions are weak and hardly significant, the negative SH summer SAM is in agreement with the findings of Roscoe et al. (2007), who found a significant negative correlation between volcanic forcing and SAM in SLP station data from 1957 to 2005. Another fact that supports the volcanic origin of those anomalies is that the strongest negative SAM indices can be found after El Chichon and Pinatubo, which are the strongest eruptions in the time period covered by the ERA-40 data. Also the timing of the negative surface SAM supports the assumption that these dynamical changes can be attributed to radiative forcing (and therefore possibly volcanic forcing), since solar input is the strongest in summer and radiative forcing can be expected to be most effective during this season. The corresponding negative SAM indices in the stratosphere and at the surface in the ERA-40 data indicate a downward propagation of zonal anomalies.

No significant SAM signal can be found after any of the three strong eruptions in the MPI-ESM results (4.18, lower right panel). Therefore no obvious connection between stratospheric signals and the surface is found in the MPI-ESM results. In general, the variability of surface and stratospheric SAM seems to be more similar in the reanalysis than in the model, supporting the findings of Miller et al. (2006), that troposphere stratosphere coupling tends to be underestimated in climate models. Nevertheless, a weak coupling effect might explain the fact that there are no simulated surface SAM responses after El Chichon and Pinatubo, while a negative SAM signal of -0.8 is present after the eruption of Krakatau. This might be related to the positive stratospheric SAM after EL Chichon and Pinatubo. If these stratospheric anomalies propagate downward, possible stratospheric and tropospheric effects might cancel each other out. In general, the variability of surface and stratospheric SAM seems to be more similar in the reanalysis than in the model, supporting the findings of Miller et al. (2006), that troposphere stratosphere coupling tends to be underestimated in climate models.

The composites by the strength of the AOD forcing also do not show a clear surface SAM responses to the volcanic forcing in the MPI-ESM simulations (figure 4.19, right panel). The only post-volcanic SAM index value that is just defined as significant is SAM index of 0.4 in the summer of the year after the weak eruptions. This surface signal is present one season after the equivalent negative signal in the stratospheric SAM. There is no significant positive stratospheric SAM after strong eruptions at the surface, but there surface SAM seems like a very damped signal of the stratospheric SAM. This may suggest a weak coupling of stratosphere and troposphere in the MPI-ESM.

4.2.3 Northern Annular Mode response

Since the NH circulation response to volcanic eruptions has been studied in more detail than changes in the SH circulation, it is convenient to examine the simulated NAM index after volcanic eruptions to further investigate the MPI-ESM's ability to capture physical mechanisms of volcanic forcing. In addition, it is of interest to see whether the responses differ between the hemispheres to get a better idea of hemispheric dependencies.

Due to the application of the EOF-analysis to the whole monthly time series and the resulting differences in variability between the seasons (see section 4.1.5), the highest NAM indices are expected in NH winter. Also the significance line is calculated in regard of the standard deviation of the deseasonalized monthly mean anomalies from the whole year. Therefore, anomalies during the seasons of high wave activity (winter) might show large values, which exceed the 95% significance lines based on the variability of all months, even though they are not particularly strong in comparison to the seasonal average. Figure 4.20 shows the seasonally averaged NAM indices after the 10 volcanic eruptions.

4.2.3.1 Stratospheric NAM

In the reanalysis data the stratospheric NAM index (4.20, upper left panel) shows in general a stronger variability than in the model. While the standard deviation of the ERA-40 stratospheric NAM time series is approximately 0.75, in the model it is only 0.4. Therefore the anomalies following the eruptions are higher in ERA-40, but not necessarily more significant. The sign of the index does vary after the different eruptions. The stratospheric NAM shows a significant positive anomaly in the first winter after the eruption of Agung (index of 1.8).

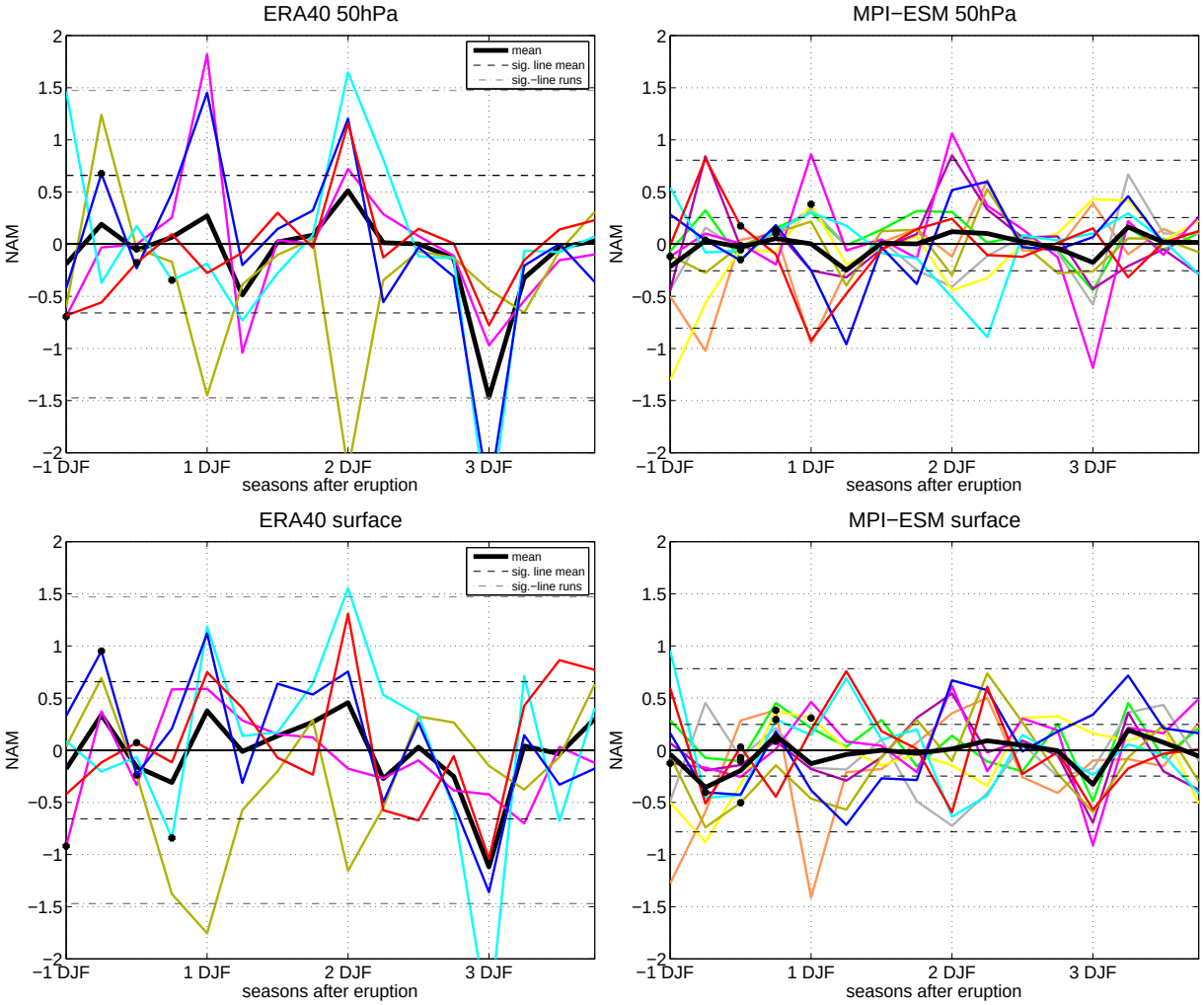

Figure 4.20: Seasonally averaged NAM index at the surface (lower panels) and at 50 hPa (upper panel) in the three years following 5 eruptions in the ERA-40 data (left panels) an 10 volcanic eruption in the MPI-ESM CMIP5 historical simulations (right panels)

For El Chichon the stratospheric NAM index is positive but not significant the first two winters after the eruption. Except for Fernandina, after all eruptions a positive index appears in the second winter, but only the index of 1.7 after the eruption of Fuego is significant. In the second NH winter after the eruption of Fernandina, the negative NAM is also significant with an index of -2.1. Noticeable is the third NH winter after the eruptions, in which no positive NAM index is present. In the third winter after Fuego and El Chichon, the index is comparatively strong with significant values of -2.7 and -2.4 respectively. Also the composite mean of all 5 eruptions shows a significant negative index of -1.5.

The sign of the stratospheric NAM index in the first winter after the eruptions in the reanalysis is in agreement with previous studies, but does not display a similar amplitude (Perlwitz and Graf, 1995; Kodera and Koide, 1997; Graf et al., 2007). Especially the lack of a positive stratospheric NAM in the winter after the eruption of Mount Pinatubo is surprising in regard of previous studies. E. g. Stenchikov et al. (2002) presented a significant GPH pattern at 50 hPa that corresponds to a positive NAM in the winter of 1991/92 in the NCEP/NCAR reanalysis data, which is completely missing in the ERA-40 results of this study. The reasons for this discrepancy will be discussed in the following chapter.

The MPI-ESM simulated stratospheric NAM at 50 hPa (4.20, upper right panel) does not follow a pattern after the eruptions. Spikes in the index mostly appear in NH winter, but there is no agreement on the sign. While the eruptions of Cotopaxi, El Chichon and Pinatubo are followed by significant negative NAM values of almost -1, there are significant positive NAM in the first two winters after Agung reaching values above 1. Because of the already discussed difficulties with the big differences in the amplitude of the inter-annual variability between NH winter and NH summer NAM, the high indices in the simulated stratospheric NAM modes in winter are no surprise and even though some of them cross the significance line, they are unlikely to really be significant. Therefore there is basically no response to the aerosol induced volcanic forcing in the MPI-ESM results. The fact that there is no strong positive stratospheric NAM in the NH winters, which would indicate an intensified polar vortex, after the eruption of Mount Pinatubo in the model simulations explains the absence of a continental winter warming pattern (Graf et al., 1993, Stenchikov et al., 2002). The composited NAM after all 10 eruptions in the MPI-ESM data does not reach significant values. The composites by the strength of the AOD signal (figure 4.21) show the strongest signal in the simulated, seasonal stratospheric NAM in the first autumn after the strong eruptions, but even this negative signal just crosses the significance line and seems to lie within the unforced variability.

4.2.3.2 Surface NAM

The post-volcanic surface NAM in the ERA-40 data (4.20, lower left panel) displays significant anomalies of both sign. In the first winter following the eruptions, all eruptions but Fernandina show a positive surface NAM. However, the positive signal after Fernandina is so strong (value of -1.7), that there is no significant signal in the composite mean. While the sign of the post-volcanic surface NAM winter signal, calculated and shown in this study, agrees with previous studies, the response shows much weaker amplitude than found in other studies (Stenchikov et al., 2006; Graf et al., 2007; Christiansen, 2008). The composite mean shows the significant negative anomaly in the third NH winter after the eruptions, that was already found at 50 hPa. In this season the index is negative after all eruptions, but only after Fuego (index of -2.6) the anomaly is significant for a single eruption. It is likely that the lack of a strong, significantly

positive surface NAM response in the winter following the eruptions in the ERA-40 results is a product of the weak stratospheric NAM signals. The curious consensual negative stratospheric NAM in the third winter after all 5 eruptions in the ERA-40 data, is also accompanied by a weaker negative surface NAM in the same winters. This result supports the theory of zonal wind anomalies propagating downward, as shown in previous studies (Baldwin and Dunkerton, 2001; Christiansen, 2001). Christiansen (2008) analyzed composites of the Arctic Oscillation around 13 volcanic eruptions using NCEP reanalysis data and only found a very weak and not significant negative signal in the third winter after the eruptions. Considering the lack of a significant positive response in the first two winters, there seems a general shift to negative NAM values in this study's ERA-40 results, which probably contributes to an overestimation of the third winter's signal.

The spread of the simulated surface NAM (4.20, lower right panel) is also large between the eruptions and hardly any anomalies are significant. An exception is the negative NAM index in the first NH winter after the eruption of Cotopaxi. This anomaly of -1.4 appears strong in comparison of the variability after the other eruptions. In contrast to the stratospheric NAM, the simulated surface NAM shows a significant negative value of 0.25 in the average of the 10 eruptions in the third NH winter. Composited by strength of the AOD forcing (figure 4.21), the simulated surface NAM also shows the most striking signal in the third winter after the eruptions in all three categories.

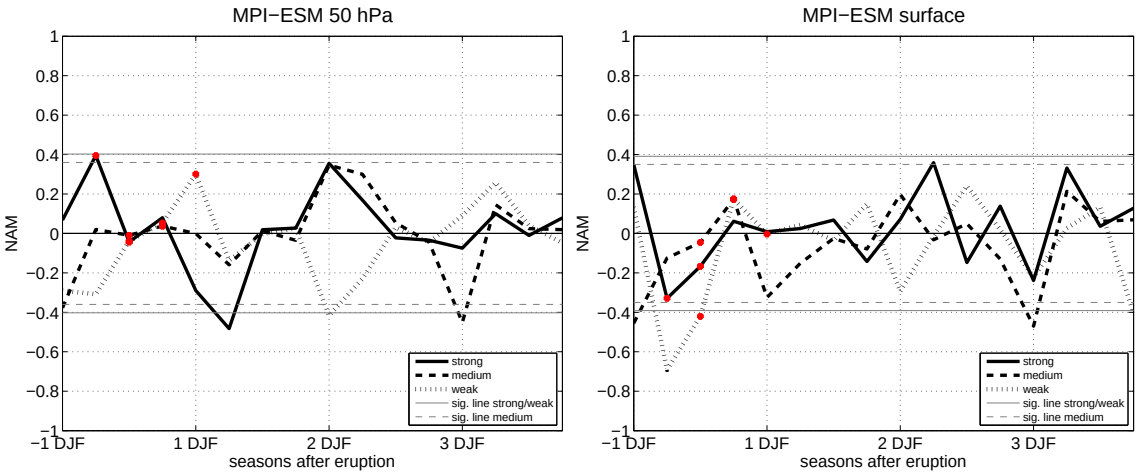

Figure 4.21: Composites of the seasonally averaged SAM index in the three years following the 10 volcanic eruptions in the ensemble mean of the MPI-ESM CMIP historical experiment. The time series are composited with respect to the strength of the eruptions AOD signals. The left panel shows the stratospheric SAM at 50 hPa, the right panel the surface SAM.

Chapter 5

Discussion

In this chapter the most important results of this study are discussed. In the methodology section mainly the reasons for discrepancies between this study's results and previous publications is discussed. In section 5.2. important mechanism, that may explain the results at hand, are named and section 5.3. covers non-volcanic influences, which are likely to be the reasons for differences between the MPI-ESM and ERA-40 results of this study.

5.1 Methodology

The comparison of this study's reanalysis results to earlier studies show a strong sensitivity of the analysis of the volcanic impact on annular modes to the index construction. The most striking example is the lack of a positive stratospheric NAM after the eruption of Mount Pinatubo in the ERA-40 results in this study. A strengthening of the NH polar vortex after the eruption of Mount Pinatubo in the ERA-40 and NCEP/NCAR reanalysis data has been shown in several publications (Stenchikov et al., 2002; Graf et al., 2007; Thomas et. al, 2009a). One reason for this underestimation in a volcanic response in the ERA-40 results of this study may lie in the calculation of the SLP and GPH anomalies, on which the EOF-analysis is based. When using a reference period previous to the volcanic eruption to calculate anomalies (e.g. Stenchikov et al., 2002) the increase of the horizontal GPH gradient at 50 hPa might be overestimated, since the positive trend during the end of the 20^{th} century could be included. In this study on the other hand, the volcanic years are included in the reference period for the anomalies, which would dampen a signal in the calculated anomalies. When considering the example of Pinatubo, the strong positive SAM in the ERA-40 in the year 1990 is also included in the reference period, that is short in comparison to other studies. Thus the volcanic signal after this eruption is probably even more underestimated than others.

When comparing composites of several volcanic eruptions, the choice of the eruptions is of importance. Stenchikov et al. (2006) found a significant strengthening of the NH polar vortex and a positive NAM phase at the surface in the composite mean of 9 post-volcanic winters. However, this composite did not include the eruption of Fernandina, after which the strongest negative winter NAM can be found in the ERA-40 data. If this eruption would be excluded in this study, the composited ERA-40 NAM would show a significantly stronger positive NAM in the first two winters.

5.2 Possible mechanisms

A variety of mechanisms and effects might have a possible influence on the annular response to volcanic eruptions. A few of these mechanism and their relevance for the results of this study are discussed in the following.

A detailed model study with the GFDL SKYHI general circulation model of the NH circulation after the Pinatubo eruption in 1991 (Stenchikov et al., 2002) showed that three factors contribute to a strengthening of the NH polar vortex and due to the stratosphere-troposphere coupling to a positive surface NAM signal. 1. The observed ozone loss after the eruption of Mount Pinatubo and the related cooling of the polar stratosphere. 2. The tropospheric weakened temperature gradient, which reduced wave activity flux into the stratosphere. 3. The warming of the mid-latitude lower stratosphere, that strengthens the horizontal temperature gradient and the polar vortex. In their experiments all of these effects would produce a positive winter NAM on their own, and the combination of all three shows a significant positive NAM. Since the volcanic effect on ozone is not included in the prescribed ozone forcing of the MPI-ESM CMIP5 historical runs, the ozone induced cooling of the stratospheric polar cap can not be expected to have a negative impact on the simulated annular mode in both hemispheres. The examined surface temperature anomalies after the Pinatubo eruption showed that this aspect of the radiative forcing is small in comparison to higher levels. Although the warming of the tropical stratosphere in the MPI-ESM could be found, there is no positive stratospheric NAM, which would indicate a strong polar vortex in the model after Pinatubo. Therefore, it has to be assumed that the eruptions considered in this study are too weak to induce circulation changes in the MPI-ESM in the NH strong enough to be identified, since the unforced variability in the NH is high in comparison to the SH.

The same three aspects may in principle hold for the SH and as in the NH in the MPI-ESM it is mostly the stratospheric temperature gradient, that can be expected to have an effect on the SH stratospheric circulation. In contrast to the NH, in the SH the model simulates a positive stratospheric annular mode response after the eruptions of Pinatubo and El Chichon. Since unforced variability in the SH is generally lower than in the NH, a volcanic signal after these two eruptions, that showed a high AOD in comparison to the other analyzed eruptions, can be identified. The seasonality of these positive stratospheric SAM indices suggests that wave-zonal flow interactions are a substantial contributor to possible response mechanisms. Karpechko et al. (2010) found a weakened wave activity flux into the SH stratosphere in spring after the eruptions in their model results, which supports this theory. Since no positive spring SAM response in the stratosphere is found in the ERA-40 data, it is possible that the effect is overestimated in the model simulations. The simulated stratospheric SAM changes do not show an echo at the surface. As wave-activity in the SH is lower than in the NH due to the land-sea distribution, the wave-induced coupling between stratosphere and troposphere can be expected to be lower.

Surprisingly the model does not show a SAM response to the eruption of Krakatau, which was followed by the strongest signal in global AOD (figure 3.1) and was also followed by the strongest warming of the lower stratosphere (see appendix, figure A9). This suggests a preconditioning of stratospheric circulation to volcanic effects by the atmosphere's composition. Due to the lack of ozone depletion during spring months in the times of the eruption of Krakatau

in comparison to modern times, the vortex is likely to have been of weaker strength during these years. A change in sensitivity to radiative forcing due to increasing westerly wind speeds in the 20th century might be a reason for the stronger responses to volcanic eruptions in the 1980s and 1990s. Detecting whether the state of the background flow has such an impact on reactions to volcanic forcing requires idealized sensitivity experiments.

While the post-volcanic stratospheric SAM changes in the MPI-ESM are reasonable in the light of the discussed mechanisms, they are of the opposite sign as the observed SAM changes. Since there is a negative SAM in the stratosphere after all eruptions but Agung and negative SAM at the surface after all eruptions in the first SH summer, it is possible that surface effects dominate stratospheric changes. A pure surface response could lead to a weakening of the surface mid-latitude westerlies and the surface SAM, due to the weakened temperature gradient, that is produced because the surface cooling after volcanic eruptions is strongest in tropical latitudes. The seasonality of the surface SAM response in the ERA-40 data supports this theory, as a cooling effect in the SH tropics and subtropics would be strongest in SH summer due to the seasonal cycle of the incoming solar radiation.

5.3 Non-volcanic contributions to annular mode signals

More importantly, the ERA-40 reanalysis data includes effects and non-volcanic forcing terms that may mask a volcanic response and are not necessarily represented in the model simulations. In the following section the possible contributions for such interfering with volcanic signals are discussed.

5.3.1 ENSO influence

Agung	0.05	0.21	0.52	0.78	1.00	1.19	1.351	1.40	1.36	1.30
Fernandina	0.44	0.60	0.752	0.84	1.00	1.25	1.36	1.24	1.18	1.03
Fuego	-0.77	-0.70	-0.59	-0.58	-0.80	-1.03	-1.21	-1.44	-1.62	-1.79
El Chichon	1.01	1.26	1.61	1.95	2.26	2.70	3.13	3.34	3.28	3.01
Pinatubo	0.99	1.08	1.194	1.44	1.78	2.15	2.34	2.42	2.38	2.10

Table 5.1: Monthly Niño 3.4 index in the first 10 months following the 5 eruptions covered by the ERA-40 data. The index is based on SST from NCEP reanalysis data and obtained from the website CGD website (CGD, 2012). Red and blue highlighted indices represent warm and cold ENSO phases (El Niño and La Niña) based on a 0.5°C threshold.

One possible explanation for the contradicting extra-tropical anomalies after volcanic eruptions in model and reanalysis could be the remote influence of the ENSO. Since the MPI-ESM historical simulations do not use prescribed SST, El Niño events are determined by the model's internal variability and do not coincide with observed El Niño years. Moreover, the fact that an ensemble mean of three simulations has been shown, the effect of ENSO is dampened in comparison to a single realization. This is in sharp contrast to the ERA-40 data, which includes possible ENSO effects.

Table 5.1 gives an overview over ENSO conditions after the 5 eruptions that are included in the ERA-40 results. It lists the SST Niño 3.4 index in the first 10 months after the eruptions

as found in NCEP reanalysis. After the eruptions of El Chichon and Pinatubo there are high positive indices with values up to 3.34 and 2.42 respectively. These values mark strong warm ENSO phase (El Niño). While ENSO is in weak warm phases after Agung and Fernandina, the Niño 3.4 index is slightly negative after the eruption of Fuego. Therefore a possible impact of ENSO is most likely to be included after the eruptions of El Chichon and Pinatubo and the composite mean ENSO of the post-volcanic months in ERA-40 is skewed towards warm ENSO.

Southern Hemisphere Robock et al. (2007) examined GPH anomalies in the first three winters following the eruption of Mount Pinatubo in reanalysis data and linked the GPH in the first winter after the eruption to El Niño instead of a volcanic impact. However, in this study the strongest negative surface SAM after Pinatubo in the ERA-40 reanalysis is found in SH spring and therefore not covered by Robock et al. (2007). The winter SAM in ERA-40 does not show unusual behavior after the Pinatubo eruption in this study.

The strong negative summer surface SAM indices after the eruptions of El Chichon and Pinatubo, during El Niños, confirm the negative effect of EL Niño on the surface SAM that has been found in several studies (section 2.4.3.1). Also the weak positive Niño 3.4 indices after Fernandina and Agung are also accompanied by a negative surface SAM in summer, while the summer SAM after Fuego, which is followed by negative Niño 3.4 indices, is closest to zero.

The wave-related mechanisms that Gong et al. (2010) suggest to have a weakening effect of El Niños on the the SH polar vortex (section 2.4.3) do not explain the negative stratospheric SAM in the ERA-40 reanalysis, since the strongest negative stratospheric SAM signals in ERA-40 after the volcanic eruptions are found in SH summer, a season of low wave activity.

Karpechko et al. (2010) dismissed the influence of El Niño as an explanation for the differences in SH circulation responses to volcanic eruptions between model and reanalysis. According to their results, only 2% of the variability of the GPH at 50 hPa in ERA-40 can be explained by the remote effect of the ENSO. The lack of knowledge about an actual connection between ENSO and SAM makes it difficult to impossible to quantify a possible contribution of the ENSO to the results of this study. Model simulations with prescribed SST would be helpful for this purpose.

Northern Hemisphere Since the influence of El Niños on the NH extra-tropical circulation has been found to be weak (section 2.4.3.1), ENSO related signals are may mask volcanic signals in the reanalysis. In model studies, El Niños have been shown to have a weakening and warming effect on the NH polar vortex due to increased vertical wave propagation (Hamilton, 1993; L'Heureux and Thompson, 2006; Manzini et al., 2006; Metzner, 2008). A possible overestimation of such an ENSO influence in the MPI-ESM could influence the NAM variability possibly masking volcanic signals. Christiansen (2008) found the simulated NH surface circulation responses to volcanic eruptions to be independent on the phase of the ENSO in observation data.

5.3.2 QBO

Another important factor that might mask volcanic influences is the modulation of extra-tropical circulation by the QBO. As figure 4.15 showed, the QBO has a strong influence on

the spacial structure of the volcanically induced temperature gradient in the stratosphere. Since the forcing of the MPI-ESM CMIP5 historical simulations does not include the QBO, only the reanalysis results could include such effects.

Kuroda et Yamazaki (2010) found a significant impact of the QBO on the SAM in reanalysis data, but the results of this study do not show a consistent QBO effect. As already mentioned, the QBO was in an easterly phase after the eruption of Pinatubo, which might be a contributor to the negative SAM response in the first SH spring in the ERA-40 data. However, this theory does not hold for the eruption of El Chichon, which was followed by a westerly QBO phase (Baldwin et al. 2001). Detailed studies of the sensitivity of the SAM influence of volcanic eruptions to the QBO phase are necessary to better understand the mechanisms that lead to the observed SAM responses.

Such a study has been conducted for the NH response to the eruption of Mount Pinatubo using the MA-ECHAM5 model (Thomas et al., 2009b). In the first winter after the eruption they found the GPH response at 30 hPa to be independent of the QBO phase, while the second winter the QBO influence becomes more obvious. Stenchikov et al. (2004) did similar experiments with the SKYHI GCM and found the inclusion of a QBO following observations to be necessary for a realistic NAM response to the Pinatubo eruption in the model. These results support the assumption that differences between observed and simulated annular mode responses to the volcanic eruptions might partly differ due to the lack of a realistic QBO forcing in the MPI-ESM results.

5.3.3 Ozone

Since the prescribed ozone climatology for the MPI-ESM CMIP5 historical runs does not include inter-annual variability, but just the seasonal cycle and observed trends, neither volcanically induced ozone changes and their effect on the annular modes (section 2.2.2) nor the unforced variability is included in model simulations.

Marshall et al. (2009) dismissed an ozone related influence of volcanic aerosols on the NAM, since they observed pre-industrial eruptions to be followed by positive NAM signals of similar amplitudes as El Chichon and Pinatubo. Kuroda et Yamazaki (2010) mentioned a ozone memory response, that might explain some persistence of a negative temperature anomaly in the polar lower stratosphere after volcanic eruptions.

Nevertheless, non-volcanic ozone changes in the stratosphere represent a strong forcing term on the annular modes in general and in both hemispheres the annular mode variability in the ERA-40 data includes ozone variability. This is likely to be one reason for the differences between the MPI-ESM and ERA-40 results.

Overall, large discrepancies between the model simulations and the reanalysis data had to be expected, considering the differences in non-volcanic forcing terms.

Chapter 6

Conclusions and outlook

In this study the indirect dynamical influence of volcanic eruptions on the extra-tropical circulation was examined. Annular mode indices were used to quantify those circulation changes. Since stratospheric mechanisms have been suggested to be of importance for volcanic effects on climate in the NH (Perlwitz and Graf, 1995, Kodera and Koide, 1997), post-volcanic annular mode changes in the coupled ocean-atmosphere model MPI-ESM with a high vertical resolution in the stratosphere were investigated and compared with ERA-40 reanalysis data in both hemispheres. 10 volcanic eruptions with global AOD stronger than 0.02 since 1850 were included in the model analysis. ERA-40 data covers 5 of these eruptions. To distinguish between stratospheric and surface responses to the volcanic eruptions, a stratospheric SAM/NAM at 50 hPa and a surface SAM/NAM was defined.

Before analyzing the annular mode changes, the general performance of the model was validated by comparing temperature and wind climatologies and the seasonal variability, as well as the simulated SAM patterns, with ERA-40 data. To check whether the MPI-ESM reproduces a realistic temperature response to volcanic eruptions in comparison to ERA-40, the eruption of Mount Pinatubo in June 1991 was used as case study. The findings can be summarized as followed:

- The MPI-ESM shows good agreement with ERA-40 data in terms of climatological temperature and wind distributions. An easterly bias in the model zonal wind is found throughout all latitudes and considered pressure levels. Stratospheric winter variability is captured well in the model in comparison to ERA-40, only at the NH a delay of the maximal strength of the polar vortex by approximately one month is found.

- The spatial pattern of the SAM as found in ERA-40, is captured reasonably well by the MPI-ESM, at the surface as well as in the stratosphere and the observed stratospheric SAM trend, shown in previous studies (Hurrell and van Loon, 1994; Zhou et al. 2000), was capture by the model.

- In the ERA-40 data, there was significant warming of the lower stratosphere in low latitudes after the eruption of Mount Pinatubo, above the equator this warming was delayed by approximately one year due to the effect of the QBO. The MPI-ESM simulated similar temperature changes in the low latitude stratosphere, but did not include the QBO effect. In the SH high latitudes, MPI-ESM and ERA-40 temperature changes show opposite signals in the SH spring seasons following the Pinatubo eruption. In the NH

high latitudes agreement model and reanalysis show a warming of the lower stratosphere in the first winter. At the surface a cooling in tropical regions was found to be more pronounced and significant in the MPI-ESM than in ERA-40 and variability in the high latitudes does generally not agree between model and reanalysis.

- In the ERA-40 data a shift to a negative stratospheric SAM is found after all 5 eruptions except for Agung, but only after Fuego and Pinatubo the signal is significant. At the surface the SAM is negative in the first summer after all eruptions, leading to a significantly negative surface SAM in the composite mean of the observed eruptions.

- In contrast, a significant positive SAM in the stratosphere is found in the spring seasons after the eruptions of El Chichon and Mount Pinatubo in the MPI-ESM simulations. These signals can not be found at the surface. Also no volcanic SAM signal was found after the other eruptions in the model simulations.

- Composites of the simulated post-volcanic SAM indices with respect to the strength of their AOD signal emphasize that the only significant SAM signals can be found in the stratosphere in the composite mean of the strongest of the simulated 10 eruptions.

- Observed changes in the NH extra-tropical stratospheric circulation after large volcanic eruptions show the opposite sign of the SH changes. Except for the eruption of Fernandina in 1968, which is followed by a strong significantly negative stratospheric NAM, there is a shift to more positive stratospheric NAM indices after all eruptions. However, only the positive stratospheric SAM after Agung is significant. In contrast to the SH, the stratospheric signals mostly show a weaker, but equivalent signal at the surface.

- The MPI-ESM results show no significant changes in the NH circulation after the volcanic eruptions. The volcanic eruptions appear to be too weak to evoke circulation changes stronger than the interannual natural variability.

The findings are in good agreement with results of the previous generation of coupled climate models that are included in the CMIP3 project (Stenchikov et al. 2006; Karpechko et al., 2010). This shows that the increase of the vertical resolution of the stratosphere alone does not lead to the simulation of observed post-volcanic circulation anomalies. Recent comparisons of high-top and low-top models with the full CMIP5 model ensemble also showed no consistent SH circulation response to volcanic forcing with regard to the representation of the stratosphere (Toohey, M., personal communication, 2012). Also post-volcanic changes in the NH were not simulated successfully by the full CMIP5 model ensemble (Driscoll et al., 2012).

To investigate the ability of MPI-ESM to simulate extra-tropical circulation responses to volcanic eruptions further, it would be of interest to simulate stronger volcanic explosions. Eruptions like Tambora in 1815, which was 3 times the size of the Pinatubo eruption in regard of sulfur emissions, have been shown to have a substantially stronger temperature effect than a Pinatubo-sized eruption in the previous MPI-ESM version, that includes ECHAM5 (Timmreck et al., 2011). Therefore such an eruption can be expected to lead to a stronger response in the annular modes.

In order to identify the reasons for the differences in post-volcanic annular mode changes in the MPI-ESM CMIP5 historical experiments and ERA-40 data, it would be helpful to analyze

ENSO and volcanic impacts. Large variations in the Pacific SST may also explain high latitude variations between the three ensemble members. To test the non-volcanic influences in observations, sensitivity runs with respect to ENSO phases or QBO phases should be considered. Atmosphere-only sensitivity simulations with the MA-ECHAM5 model emphasized the effect of ENSO and QBO on the NH circulation response to the eruption of Mount Pinatubo (Thomas et al., 2009b).

In general, it might be helpful to extend this study by looking at the single ensemble members of the MPI-ESM simulations instead of only considering the ensemble mean. Strong differences among the ensemble members would suggest that the simulated signals are not of volcanic origin. Since the volcanic signals may be too weak in comparison to the internal variability of the atmosphere, it would also be helpful to run more simulations and increase the number of ensemble members. A larger ensemble of model simulations would increase the signal-to-noise ratio and be useful to detect volcanic effects.

The results of this study basically confirmed the need for further research on the volcanic impact on the extra-tropical circulation both in observations and in model data.

Acknowledgments

This work could not have been done without the professional and moral support of my advisers, colleagues, friends and family.

First I want to thank Dr. Kirstin Krüger, who gave me this assignment and the opportunity to do research on such an interesting topic. I am very grateful for her advise and suggestions throughout the whole working process, the effort and time she spent on correcting my thesis and especially her always encouraging words.

I especially want to express my thanks to Dr. Matt Toohey. He was a great adviser, constantly motivating, providing counsel and offering constructive criticism. He was also very patient with discussing and explaining the most insignificant details with me. Moreover I appreciate the time and effort he spent on acquiring data for me.

In addition, I would like to thank the 'Middle and Upper Atmosphere' - group of the Max Planck Institute for Meteorology, Hamburg, and in particular Dr. Hauke Schmidt, for providing the MPI-ESM CMIP5 historical experiment data.

Furthermore I want to express my gratitude to Prof. Dr. Douglas Maraun for taking the time to read and evaluate my thesis.

Another big thank you goes to Tobias Bayr, who answered all my questions about the EOF-analysis and provided me with helpful details about the application of the EOF-analysis on geographical data.

I am also very grateful to Jennifer Mecking, who solved all my Matlab-problems within 5 minutes and answered my numerous questions about colorbars and the English language.

Last but not least I would like to extend my thanks to all my friends and my family for their proof-reading, open ears, endless patience and general support.

References

- Arblaster, J. M. and G. A. Meehl (2007): *Contributions of External Forcings to Southern Annular Mode Trends. Journal of Climate*, 19, 12, 2896.
- Archambault, H. M., L. F. Bosart, D. Keyser, A. R. Aiyyer (2008): *Influence of Large-Scale Flow Regimes on Cool-Season Precipitation in the Northeastern United States.* Mon. Wea. Rev., 136, 2945–2963.
- Baldwin, M.P. (2001): *Annular modes in global daily surface pressure.* Geophys. Res. Lett., 28, 4115–4118.
- Baldwin, M. P., and T. J. Dunkerton (1998): *Quasibiennial modulation of the southern hemisphere stratospheric polar vortex.* Geophys. Res. Lett., 25,17, 3343–3346.
- Baldwin, M. P., and T. J. Dunkerton (1999): *Propagation of the Arctic Oscillation from the stratosphere to the troposphere.* J. Geophys. Res., 104(D24), 30,937–30.
- Baldwin, M.P., and T. J. Dunkerton (2001): *Stratospheric Harbingers of Anomalous Weather Regimes.* Science, 294, 5542, 581-584.
- Baldwin, M. P. and D. O'Sullivan (1995): *Stratospheric Effects of ENSO-Related Tropospheric Circulation Anomalies.* Journal of Climate, 8, 4, 649-667.
- Baldwin, M.P., L.J. Gray, T.J. Dunkerton, K. Hamilton, P.H. Haynes, W.J. Randel, J.R. Holton, M.J. Alexander, I. Hirota, T. Horinouchi, D.B.A. Jones, J.S. Kinnersley, C. Marquardt, K. Sato, and M. Takahashi (2001): *The Quasi-Biennial Oscillation*, Reviews of Geophysics, 39, 179-229.
- de Beurs, K. M. and G. M. Henebry (2008): *Northern Annular Mode Effects on the Land Surface Phenologies of Northern Eurasia.* J. Climate, 21, 4257–4279.
- Bluth, G. J. S., S. D. Doiron, S. C. Schnetzler, A. J. Krueger, and L. S. Walter (1992): *Global tracking of the SO2 clouds from the June 1991 Mount Pinatubo eruptions.* Geophys. Res. Lett., 19, 151–154.
- CGD (2012): <http://www.cgd.ucar.edu/cas/catalog/climind/TNI_N34/index.html#Sec5>, accessed on 05.02.2012.
- CPC (2012): <http://www.cpc.ncep.noaa.gov/>, accessed on 14.02.2012.

- Charney, J. G. und P. G. Drazin (1961): *Propagation of planetary-scale disturbances from the lower into the upper atmosphere.* Journal of Geophysical Research, 66, 83–109.
- Chen G. and L. Sun (2011): *Mechanisms of the Tropical Upwelling Branch of the Brewer–Dobson Circulation: The Role of Extratropical Waves.* Journal of the Atmospheric Sciences, 68:12, 2878-2892.
- Christiansen, B. (2001): *Downward propagation of zonal mean zonal wind anomalies from the stratosphere to the troposphere: Model and reanalysis.* J. Geophys. Res., 106, 27,307–27.
- Christiansen, B. (2008): *Volcanic eruptions, large-scale modes in the northern hemisphere, and the el niño–southern oscillation.* J. Climate, 21, 910–922.
- Cionni, I., V. Eyring, J. F. Lamarque, W. J. Randel, D. S. Stevenson, F. Wu, G. E. Bodeker, T. G. Shepherd, D. T. Shindell, and D. W. Waugh (2011): *Ozone database in support of CMIP5 simulations: results and corresponding radiative forcing.* Atmos. Chem. Phys., 11, 11267-11292.
- Crooks, S. A. and L. J. Gray (2005): *Characterization of the 11-Year Solar Signal Using a Multiple Regression Analysis of the ERA-40 Dataset.* J. Climate, 18, 996–1015.
- Dommenget, D. (2008): *An Introduction to Statistical Analysis in Climate Research*, unfinished script for the statistic lecture. Version summer term 2008.
- Driscoll, S., A. Bozzo, L. J. Gray, A. Robock and G. Stenchikov (2012): *Coupled Model Intercomparison Project 5 (CMIP5) simulations of climate following volcanic eruptions.* Submitted to J. Geophys. Res.
- Duggen, S., P. Croot, U. Schacht, and L. Hoffmann (2007): *Subduction zone volcanic ash can fertilize the surface ocean and stimulate phytoplankton growth: Evidence from biogeochemical experiments and satellite data.* Geophys. Res. Lett., 34, L01612.
- Enquete-Kommission "Schutz der Erdatmosphäre" des Deutschen Bundestages (Editor) (1992): *Klimaänderung gefährdet globale Entwicklung.* Economia Verlag, Bonn.
- Fischer, E. M., J. Luterbacher, E. Zorita, S. F. B. Tett, C. Casty, and H. Wanner (2007): *European climate response to tropical volcanic eruptions over the last half millennium.* Geophys. Res. Lett., 34, L05707.
- Fogt, R. L., D. H. Bromwich, K. M. Hines (2011): *Understanding the SAM influence on the South Pacific ENSO teleconnection.* Climate Dynamics, 36, 7-8, 1555-1576.
- Forsyth, P. Y. (1988): *In the wake of Etna, 44 B.C.* Classical Antiquity 7, 49-57.
- Fortuin, J. P. F. and H. Kelder (1998): *An ozone climatology based on ozonesonde and satellite measurements.* J. Geophys. Res., 103, 31709-31734.
- Gillett, N. P. and D. W. J. Thompson (2003): *Simulation of Recent Southern Hemisphere Climate Change.* Science, 302,5643, 273-275.

- Giorgetta, M. (2011): *German contribution to CMIP5.* Presentation at WGCM15, Boulder, October, 2011.
- Gong, D. and S. Wang (1999): *Definition of Antarctic oscillation index.* Geophysical Research Letters, 26 (4), 459-462.
- Gong, T., S. B. Feldstein, D. Luo (2010): *The Impact of ENSO on Wave Breaking and Southern Annular Mode Events.* J. Atmos. Sci., 67, 2854–2870.
- Goosse H., P.Y. Barriat, W. Lefebvre, M.F. Loutre and V. Zunz (2012): *Introduction to climate dynamics and climate modeling.* Online textbook available at <http://www.climate.be/textbook>, accessed on 05.01.2012.
- Gordon, A. L., M. Visbeck and J. C. Comis (2007): *A possible link between the Weddell Polynya and the Southern Annular Mode.* Journal of Climate, 20, 11, 2558-2571.
- Graf, H.-F., Q. Li, and M.A. Giorgetta (2007): *Volcanic effects on climate: Revisiting the mechanisms.* Atmos. Chem. Phys., 7, 4503-4511.
- Graf, H.-F. and D. Zanchettin (2012): *Central Pacific El Niño, the "subtropical bridge," and Eurasian climate.* J. Geophys. Res., 117, D01102.
- Graf, H.-F., I. Kirchner, A. Robock and I. Schult (1993): *Pinatubo eruption winter climate effects: model versus observations.* Clim. Dyn., 9, 81–93.
- Graversen, R. G., and B. Christiansen (2003): *Downward propagation from the stratosphere to the troposphere: A comparison of the two hemispheres.* J. Geophys. Res., 108, D24, 4780.
- Groisman, P. Ya. (1992): *Possible regional climate consequences of the Pinatubo eruption: An empirical approach.* Geophys. Res. Lett., 19(15), 1603–1606.
- Guo, S., G. J. S. Bluth, W. I. Rose, I. M. Watson, and A. J. Prata (2004): *Re-evaluation of SO2 release of the 15 June 1991 Pinatubo eruption using ultraviolet and infrared satellite sensors.* Geochem. Geophys. Geosyst., 5, Q04001.
- Haigh J.D. and H. K. Roscoe (2006): *Solar influences on polar modes of variability.* Meteorol. Z., 15, 371–378.
- Hamilton, K. (1993): *An Examination of Observed Southern Oscillation Effects in the Northern Hemisphere Stratosphere.* J. Atmos. Sci., 50, 3468–3474.
- Harangozo, S. (2000): *A search for ENSO teleconnections in the west Antarctic Peninsula climate in austral winter.* International Journal of Climatology, 20, 663–679.
- Hartmann, D. L. and F. Lo (1998): *Wave-Driven Zonal Flow Vacillation in the Southern Hemisphere.* J. Atmos. Sci., 55, 1303–131.
- Haynes, P. H., C. Marks, M. E. McIntyre, T. Shepherd und K. Shine (1991): *" Downward control" of extratropical diabatic circulations by eddy-induced mean zonal forces.* Journal of the Atmospheric Sciences, 48, 651–679.

- Hegerl, G. C., T. J. Crowley, S. K. Baum, K.-Y. Kim, and W. T. Hyde (2003): *Detection of volcanic, solar and greenhouse gas signals in paleo-reconstructions of Northern Hemispheric temperature.* Geophys. Res. Lett., 30, 5, 1242.

- Hendon, H. H., D. W. J. Thompson, M. C. Wheeler (2007): *Australian Rainfall and Surface Temperature Variations Associated with the Southern Hemisphere Annular Mode.* J. Climate, 20, 2452–2467.

- Holton, J. R. and H.-C. Tan (1980): *The Influence of the Equatorial Quasi-Biennial Oscillation on the Global Circulation at 50 mb.* J. Atmos. Sci., 37, 2200–2208.

- Holton, J. R., P. H. Haynes, E. M. McIntyre, A. R. Douglass, R. B. Rood, and L. Pfister (1995): *Stratosphere-troposphere exchange, Rev. Geophys.*, 33, 403–439.

- Hurrell, J. W. and H. van Loon (1994): *A modulation of the atmospheric annual cycle in the Southern Hemisphere.* Tellus A, 46, 3, 325.

- Jungclaus, J.H., M. Botzet, H. Haak, N. Keenlyside, J.-J. Luo, M. Latif, J. Marotzke, U. Mikolajewicz and E. Roeckner (2006): *Ocean circulation and tropical variability in the coupled model ECHAM5/MPI-OM.* Journal of Climate, 19, 3952-3972.

- Kalnay, E. and 21 others (1996): *The NCEP/NCAR 40-year reanalysis project.* Bull. Amer. Meteor. Soc., 77, 437-471.

- Karoly, D. J. (1990): *The role of transient eddies in low-frequency zonal variations of the Southern Hemisphere circulation.* Tellus A, 42: 41–50.

- Karpechko, A. Y., N. P. Gillett, M. Dall'Amico and L. J. Gray (2010): *Southern Hemisphere atmospheric circulation response to the El Chichón and Pinatubo eruptions in coupled climate models.* Quarterly Journal of the Royal Meteorological Society, 136, 1813–1822.

- Kelly, P. M., P. D. Jones and P. Q. Jia (1996): T*he spatial response of the climate system to explosive volcanic eruptions, Int. J. Climatol.*, 16, 5, 537–550.

- Kidson, J. W. (1988): *Indices of the Southern Hemisphere Zonal Wind.* J. Climate, 1, 183–194.

- Kidson, J. W. and I. G. Watterson (1999): *The Structure and Predictability of the "High-Latitude Mode" in the CSIRO9 General Circulation Model.* J. Atmos. Sci., 56, 3859–3873.

- Kodera, K., and H. Koide (1997): *Spatial and seasonal characteristics of recent decadal trends in the northern hemispheric troposphere and stratosphere.* J. Geophys. Res., 102, D16, 19, 433–19.

- Krüger, K., B. Naujokat, and K. Labitzke (2005): T*he unusual midwinter warming in the southern hemisphere stratosphere 2002: a comparison to northern hemisphere phenomena.* J. Atmos. Soc., 62 (3), 603-613.

- Kuroda, Y., and K. Yamazaki (2010): *Influence of the solar cycle and QBO modulation on the Southern Annular Mode.* Geophys. Res. Lett., 37, L12703

- Kushnir, Y. (2000): *The Climate System*, EESC 2100, Spring 2007, available at: <http://eesc.columbia.edu/courses/ees/climate/lectures/gen_circ/>, accessed on 09.02.2012.

- Labitzke, K. (1987): *Sunspots, the QBO, and the stratospheric temperature in the north polar region.* Geophys. Res. Lett., 14, 5, 535–537.

- Labitzke, K. G. (2004): *On the signal of the 11-year sunspot cycle in the stratosphere over the Antarctic and its modulation by the Quasi-Biennial Oscillation (QBO).* Meteorol. Z. 13, 263– 270.

- Labitzke, K. G., and H. van Loon (1999): *The Stratosphere: Phenomena, History, and Relevance.* Springer, New York.

- Lamarque, J.-F., T. C. Bond, V. Eyring, C. Granier, A. Heil, Z. Klimont, D. Lee, C. Liousse, A. Mieville, B. Owen, M. G. Schultz, D. Shindell, S. J. Smith, E. Stehfest, J. Van Aardenne, O. R. Cooper, M. Kainuma, N. Mahowald, J. R. McConnell, V. Naik, K. Riahi and D. P. van Vuuren (2010): *Historical (1850–2000) gridded anthropogenic and biomass burning emissions of reactive gases and aerosols: methodology and application.* Atmos. Chem. Phys., 10, 7017–7039.

- Lamb, H. H. (1970): *Volcanic dust in the atmosphere, with a chronology and assessment of its meteorological significance.* Philos. Trans. R. Soc. London, Ser. A, 266, 425–533.

- Langematz, U., M. Kunze, K. Krüger, K. Labitzke, and G. L. Roff (2003): *Thermal and dynamical changes of the stratosphere since 1979 and their link to ozone and CO2 changes.* J. Geophys. Res., 108(D1), 4027.

- Lean, J. (2009): *Calculations of Solar Irradiance: monthly means from 1882 to 2008, annual means from 1610 to 2008.* available on: <http://www.geo.fu-berlin.de/en/met/ag/strat/forschung/SOLARIS/Input_data/CMIP5_solar_irradiance.html>, accessed on 06.01.2012.

- L'Heureux, M. L. and D. W. J. Thompson (2006): *Observed Relationships between the El Niño–Southern Oscillation and the Extratropical Zonal-Mean Circulation.* J. Climate, 19, 276–287.

- Lovenduski, N., and N. Gruber (2005): *Impact of the Southern Annular Mode on Southern Ocean circulation and biology.* Geophys. Res. Lett., 32, L11603.

- Manzini, E., M.A. Giorgetta, M. Esch, L. Kornblueh and E. Roeckner (2006): *The influence of sea surface temperatures on the northern winter stratosphere: ensemble simulations with the MAECHAM5 model.* J. Climate, 19, 3863-3881.

- Marsland, S.J., H. Haak, J.H. Jungclaus, M. Latif, and F. Röske (2003): *The Max-Planck- Institute global ocean/sea ice model with orthogonal curvilinear coordinates.* Ocean Modelling, 5, 91-127.

- Marshall G. J. (2003): *Trends in the Southern Annular Mode from observations and reanalyses.* Journal of Climate, 16, 4134-4143.
- Marshall, G. J., P. A. Stott, J. Turner, W. M. Connolley, J. C. King, and T. A. Lachlan-Cope (2004): *Causes of exceptional atmospheric circulation changes in the Southern Hemisphere.* Geophys. Res. Lett., 31, L14205.
- Marshall, A. G., A. A. Scaife, and S. Ineson (2009): *Enhanced seasonal prediction of european winter warming following volcanic eruptions.* Journal of Climate, 22, 23, 6168–517, 6180.
- McInturff, R. (1978): *Stratospheric warmings: Synoptic, dynamic and general circulation aspects.* NASA Ref Publ., 1017, 166.
- Metzner, D. (2008): *Der Einfluss von ENSO auf den NH Winter im ECHAM5 Modell und die Rolle der Stratosphaere.* Diploma Thesis at IFM-Geomar, 127.
- Miller, R. L., G. A. Schmidt, and D. T. Shindell (2006): *Forced annular variations in the 20th century Intergovernmental Panel on Climate Change Fourth Assessment Report models.* J. Geophys. Res., 111, D18101.
- Nakamura, H., T. Sampe, A. Goto, W. Ohfuchi, and S.-P. Xie (2008): *On the importance of mid-latitude oceanic frontal zones for the mean state and dominant variability in the tropospheric circulation.* Geophysical Research Letters 35, L15709.
- NASA (Last updated in May 2011): *Solar System Exploration.* Available at <http://solarsystem.nasa.gov>, accessed on 09.02.2012.
- Newhall, C. G. and S. Self (1982): *The Volcanic Explosivity Index (VEI) An Estimate of Explosive Magnitude for Historical Volcanism.* J. Geophys. Res., 87(C2), 1231–1238.
- Nikulin, G. and F. Lott (2010): *On the time-scales of the downward propagation and of the tropospheric planetary wave response to the stratospheric circulation.* Ann. Geophys., 28, 339-351.
- Pawson, S., K. Labitzke, and S. Leder (1998): *Stepwise changes in stratospheric temperature.* Geophys. Res. Lett., 25, 12, 2157–2160.
- Pawson, S., K. Kodera, K. Hamilton, T. G. Shepherd, S. R. Beagley, B. A. Boville, J. D. Farrara, T. D. A. Fairlie, A. Kitoh, W. A. Lahoz, U. Langematz, E. Manzini, D. H. Rind, A. A. Scaife, K. Shibata, P. Simon, R. Swinbank, L. Takacs, R. J. Wilson, J. A. Al-Saadi, M. Amodei, M. Chiba, L. Coy, J. de Grandpré, R. S. Eckman, M. Fiorino, W. L. Grose, H. Koide, J. N. Koshyk, D. Li,k, J. Lerner, J. D. Mahlman, N. A. McFarlane, C. R. Mechoso, A. Molod, A. O'Neill, R. B. Pierce, W. J. Randel, R. B. Rood and F. Wuh (2000): *The GCM-Reality Intercomparison Project for SPARC (GRIPS): Scientific issues and initial results.* Bull. Amer. Meteorol. Soc., 81, 781-796.
- Perlwitz, J. and H.-F. Graf (1995): *The Statistical Connection between Tropospheric and Stratospheric Circulation of the Northern Hemisphere in Winter.* Journal of Climate, 8, 10, 2281-2295.

- Perlwitz, J., and N. Harnik (2003): *Observational Evidence of a Stratospheric Influence on the Troposphere by Planetary Wave Reflection.* J. Climate, 16, 3011–3026.
- Perlwitz, J. and N. Harnik (2004): *Downward Coupling between the Stratosphere and Troposphere: The Relative Roles of Wave and Zonal Mean Processes*.* J. Climate, 17, 4902–4909.
- Pilotfriend: *General global circulation.* available at: <http://www.pilotfriend.com/av_weather/meteo/prv_wnd.htm>, accessed on 09.02.2012.
- Polvani, L. M. and D. W. Waugh (2004): *Upward Wave Activity Flux as a Precursor to Extreme Stratospheric Events and Subsequent Anomalous Surface Weather Regimes.* J. Climate, 17, 3548–3554.
- Portmann, R. W., S. Solomon, R. R. Garcia, L. W. Thomason, L. R. Poole, and M. P. McCormick (1996): *Role of aerosol variations in anthropogenic ozone depletion in the polar regions.* J. Geophys. Res., 101, D17, 22,991–23.
- Randel, W.J. (1988): *The seasonal evolution of planetary waves in the Southern Hemisphere stratosphere and troposphere.* Quart. J. Roy. Meteorol. Soc., 114, 1385-1409.
- Randel, W. and F. Wu (1999): *Cooling of the Arctic and Antarctic Polar Stratospheres due to Ozone Depletion.* Journal of Climate, 12, 5, 1467-1479.
- Rampino, M. R., and S. Self (1984): *Sulphur-rich volcanic eruptions and stratospheric aerosols*, Nature, 310, 677–679.
- Rast, S. (2011): *Volcanic aerosols (data of G. Stenchikov).* Technical report.
- Ribera, P., and M. E. Mann (2003): *ENSO related variability in the Southern Hemisphere, 1948–2000.* Geophys. Res. Lett., 30, 1006.
- Robock, A. (1983): *Ice and snow feedbacks and the latitudinal and seasonal distribution of climate sensitivity.* J. Atmos. Sci., 40, 986-997.
- Robock, A., (2000): *Volcanic eruptions and climate.* Rev. Geophys., 38, 191-219.
- Robock, A. and J. Mao (1995): *The volcanic signal in surface temperature observations*, J. Clim., 8, 1086–1103.
- Robock, A., T. Adams, M. Moore, L. Oman, and G. Stenchikov (2007): *Southern Hemisphere atmospheric circulation effects of the 1991 Mount Pinatubo eruption.* Geophys. Res. Lett., 34, L23710.
- Roeckner, E., (2003):. *The atmospheric general circulation model ECHAM5 (Part I).* Technical Report 349, Max-Planck-Institut für Meteorologie.
- Roeckner, E., R. Brokopf, M. Esch, M. Giorgetta, S. Hagemann, and L. Kornblueh (2006): *Sensitivity of Simulated Climate to Horizontal and Vertical Resolution in the ECHAM5 Atmosphere Model.* J. Climate, 19, 3771–3791.

- Roeckner E., K. Arpe, L. Bengtsson, M. Christoph, M. Claussen, L. Dümenil, M. Esch, M. Giorgetta, U. Schlese, U. Schulzweida (1996): *The atmospheric general circulation model ECHAM-4: Model description and simulation of present-day climate.* Technical Report 218, Max-Planck-Institut für Meteorologie.
- Roscoe, H. K. and J. D. Haigh (2007): *Influences of ozone depletion, the solar cycle and the QBO on the Southern Annular Mode.* Quarterly Journal of the Royal Meteorological Society, 133, 1855–1864.
- Shindell, D. T., R. L. Miller, G. Schmidt, and L. Pandolfo (1999): *Simulation of the Arctic Oscillation trend by greenhouse forcing of a stratospheric model.* Nature, 399, 452–455.
- Shindell, D. T., and G. A. Schmidt (2004): *Southern Hemisphere climate response to ozone changes and greenhouse gas increases.* Geophys. Res. Lett., 31, L18209.
- Shindell, D. T., G. A. Schmidt, M. E. Mann, and G. Faluvegi (2004): *Dynamic winter climate response to large tropical volcanic eruptions since 1600.* J. Geophys. Res., 109, D05104.
- Sigmond, M, M. C. Reader, J. C. Fyfe and N.P. Gillett (2011): *Drivers of past and future Southern Ocean change: Stratospheric ozone versus greenhouse gas impacts.* Geophysical Research Letters, 38, L12601.
- Silvestri, G., and C. Vera (2009): *Nonstationary impacts of the southern annular mode on Southern Hemisphere climate* J. Climate, 22, 22, 6142-6148.
- Simmons, A. J. and D. M. Burridge (1981): *An energy and angular-momentum conserving vertical nite dierence scheme and hybrid vertical coordinates.* Mon. Wea. Rev., 109, 758-766.
- Smithonian (2011): *Global Volcanism Program.* <http://www.volcano.si.edu/index.cfm>, accessed on 12.02.2012.
- Solomon, S., R. W. Sanders, R. R. Garcia and J. G. Keys (1993): *Increased chlorine dioxide over Antarctica caused by volcanic aerosols from Mount Pinatubo.* Nature, 363, 245–248.
- Solomon, S. (1999): *Stratospheric ozone depletion: A review of concepts and history.* Rev. Geophys., 37, 275–316.
- Song, Y. and W. A. Robinson (2004): *Dynamical Mechanisms for Stratospheric Influences on the Troposphere. Journal of Atmospheric Sciences*, 61, 14, 1711-1725.
- SPARC CCMVal (2010), *SPARC Report on the Evaluation of Chemistry-Climate Models.* V. Eyring, T. G. Shepherd, D. W. Waugh (Eds.), SPARC Report No. 5, WCRP-132, WMO/TD-No. 1526.
- Stenchikov, G., A. Robock, V. Ramaswamy, M. D. Schwarzkopf, K. Hamilton, and S. Ramachandran (2002): *Arctic Oscillation response to the 1991 Mount Pinatubo eruption: Effects of volcanic aerosols and ozone depletion,* Journal of Geophysical Research, 107,4803.

- Stenchikov, G., K. Hamilton, A. Robock, V. Ramaswamy, and M. D. Schwarzkopf (2004): *Arctic Oscillation response to the 1991 Pinatubo Eruption in the SKYHI GCM with a realistic Quasi-Biennial Oscillation.* J. Geophys. Res., 109, D03112.

- Stenchikov, G., K. Hamilton, R. J. Stouffer, A. Robock, V. Ramaswamy, B. Santer, and H.-F. Graf (2006): *Arctic Oscillation response to volcanic eruptions in the IPCC AR4 climate models*, J. Geophys. Res., 111, D07107.

- Stier, P., Feichter, J., Kinne, S., Kloster, S., Vignati, E., Wilson, J., Ganzeveld, L., Tegen, I., Werner, M., Balkanski, Y., Schulz, M., Boucher, O., Minikin, A., and Petzold, A. (2005): *The aerosol-climate model ECHAM5-HAM*, Atmos. Chem. Phys., 5, 1125-1156.

- Taylor, K. E. , R. J. Stouffer and G. A. Meehl (2009, with updates/corrections made 2011): *A Summary of the CMIP5 Experiment Design*, Technical Report, available at: http://cmip-pcmdi.llnl.gov/cmip5/experiment_design.html, accessed on 11.01.2012.

- Thomas, M. A., C. Timmreck, M. A. Giorgetta, H.-F. Graf and G. Stenchikov (2009a): *Simulation of the climate impact of Mt. Pinatubo eruption using ECHAM5 – Part 1: Sensitivity to the modes of atmospheric circulation and boundary conditions.* Atmos. Chem. Phys., 9, 757–769.

- Thomas, M. A., M. A. Giorgetta, C. Timmreck, H.-F. Graf and G. Stenchikov (2009b): *Simulation of the climate impact of Mt. Pinatubo eruption using ECHAM5 – Part 2: Sensitivity to the phase of the QBO and ENSO*, Atmos. Chem. Phys., 9, 3001-3009.

- Thompson, D.W.J. (2007): *A Brief Introduction to the Annular Modes and Annular Mode Research.* David W. J. Thompson, available at: <http://www.atmos.colostate.edu/ao/introduction.html>, accessed on 11.01.2012.

- Thompson, D.W. J. and S. Solomon (2002): *Interpretation of recent Southern Hemisphere climate change.* Science, 296, 895–899.

- Thompson, D. W. J., and J. M. Wallace (1998): *The Arctic Oscillation signature in the wintertime geopotential height and temperature fields.* Geophys. Res. Lett., 25, 1297-1300.

- Thompson, D. W. J. and J. M. Wallace (2000): *Annular Modes in the Extratropical Circulation. Part I: Month-to-Month Variability*.* J. Climate, 13, 1000–1016.

- Thompson, D. W. J., J. M. Wallace, and G. C. Hegerl (2000): *Annular modes in the extratropical circulation. Part II: Trends.* J. Climate, 13, 1018-1036.

- Thompson, D.W.J, J.M. Wallace, P.D. Jones, and J.J. Kennedy (2009): *Identifying signatures of natural climate variability in time series of global-mean surface temperature: Methodology and Insights.* J. Climate, 22, 6120-6141.

- Timmreck C., H.-F. Graf, D. Zanchettin, S. Hagemann, T. Kleinen, K. Krüger (2011): *Climate response to the Toba super-eruption: Regional changes.* Quaternary International (published online), available at: <http://www.sciencedirect.com/science/article/pii/S1040618211005817>.

- Toohey, M., K. Krüger, U. Niemeier and C. Timmreck (2011): *The influence of eruption season on the global aerosol evolution and radiative impact of tropical volcanic eruptions.* Atmos. Chem. Phys., 11, 12351-12367.
- Trepte, C. R., R. E. Veiga, and M. P. McCormick (1993): *The Poleward Dispersal of Mount Pinatubo Volcanic Aerosol*, J. Geophys. Res., 98, D10, 18,563–18,573.
- Uppala S. , P. Kallberg, A. Hernandez, S. Saarinen, M. Fiorino, X. Li, K. Onogi, N. Sokka, U. Andrae, and V. Da Costa Bechthold (2004): *ERA-40: ECMWF 45-year reanalysis of the global atmosphere and surface conditions 1957-2002.* ECMWF Newsletter 101.
- Uppala, S. M., P. W. Kållberg, A. J. Simmons, U. Andrae, V. Da Costa Bechtold, M. Fiorino, J. K. Gibson, J. Haseler, A. Hernandez, G. A. Kelly, X. Li, K. Onogi, S. Saarinen, N. Sokka, R. P. Allan, E. Andersson, K. Arpe, M. A. Balmaseda, A. C. M. Beljaars, L. Van De Berg, J. Bidlot, N. Bormann, S. Caires, F. Chevallier, A. Dethof, M. Dragosavac, M. Fisher, M. Fuentes, S. Hagemann, E. Hólm, B. J. Hoskins, L. Isaksen, P. A. E. M. Janssen, R. Jenne, A. P. Mcnally, J.-F. Mahfouf, J.-J. Morcrette, N. A. Rayner, R. W. Saunders, P. Simon, A. Sterl, K. E. Trenberth, A. Untch, D. Vasiljevic, P. Viterbo, J. Woollen (2005): *The ERA-40 reanalysis.* Quarterly Journal of the Royal Meteorological Society, 131,612, 2961–3012.
- Valcke, S. (2006): *OASIS3 User Guide (prism_2-5).* PRISM Support Initiative Report No 3, 64.
- van Loon, H., and K. Labitzke (1987): *The Southern Oscillation. part V: The anomalies in the lower stratosphere of the Northern-Hemisphere in winter and a comparison with the Quasi-Biennial Oscillation.* Mon. Weather Rev., 115(2), 357– 369.
- van Noije, T. P. C., H. J. Eskes, M. van Weele und P. F. J. van Velthoven, (2004): *Implications of the enhanced Brewer-Dobson circulation in European centre for medium-range weather forecasts reanalysis ERA-40 for the stratosphere-troposphere exchange of ozone in global chemistry transport models.* Journal of Geophysical Research, 109, D19308.
- von Storch, H. and F.W. Zwiers (1999): *Statistical Analysis in Climate Research.* Cambridge University Press.
- Wang, S.-W. (1992): *Studies on the Atmosperic centers of Action.* Report in State University of New York at Stony Brooks, 32.
- Wild, M., and E. Roeckner (2006): *Radiative fluxes in the ECHAM5 general circulation model.* J. Climate, 19, 3792-3809.
- WMO (2006): *Scientific assessment of ozone depletion: 2006*, Chapter 4.
- Yuan, X., and C. Li (2008): *Climate modes in southern high latitudes and their impacts on Antarctic sea ice.* J. Geophys. Res., 113, C06S91.
- Zhou, S. T. , M. E. Gelman, A. J. Miller and J. P. McCormack (2000): *An Interhemisphere Comparison o f the Persistent Stratospheric Polar Vortex.* Geophys. Res. Lett. 27, 1123.

Abbreviations and variables

AOD:	Aerosol optical depth
AOI:	Antarctic Oscillation index
BDC:	Brewer-Dobson-Circulation
EP-flux:	Eliassen-Palm flux
GISS:	Goddard Institute for Space Studies
GPH:	Geopotential height
K:	Kelvin
NAM:	Northern annular mode
NH:	Northern hemisphere
SAM:	Southern annular mode
SH:	Southern hemisphere
SLP:	Sea level pressure
SST:	Sea surface temperature
TOA:	Top of the atmosphere
P:	Power emmitted by a body per surface unit [W]
$\sum$:	Covariance matrix, at position i,j one can find the covariance of the variable 1 (spatial point i) and variable 2 (spatial point j)
$P^*_{40°\mathrm{S}}$:	Standardized zonal mean sea level pressure at 40° South
σ :	Boltzmann constant
ε:	Emissivity
λ_{max}:	Wavelength of maximal power
b:	Wien's displacement constant

T:	Surface temperature
τ :	Optical depth
I_{surf} :	Solar radiation reaching the Earth's surface
I_S:	Identiy matrix of size SxS
toa_{surf} :	Solar radiation reaching TOA
u_{th}:	Thermal wind
R_L:	Gas constant for dry air
f:	Coriolis factor
$\frac{\partial T}{\partial n}$:	Temperature gradient perpendicular to isotherms
p_L:	Air pressure on lower isobaric surface
p_H:	Air pressure on upper isobaric surface

Appendix A

Figures

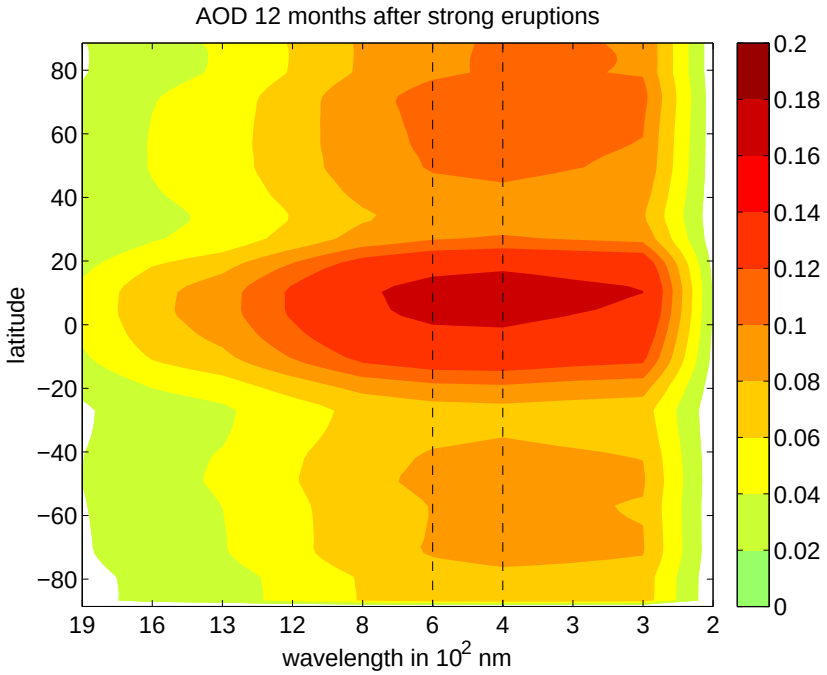

Figure A1: Composite of AOD 12 months after the eruptions of Krakatau, El Chichon and Mount Pinatubo as a function of latitude and wavelength as found in the aerosol forcing of MPI-ESM. Dashed lines mark the spectral band, that is used to classifying volcanic eruptions according to their maximal AOD signal in this study.

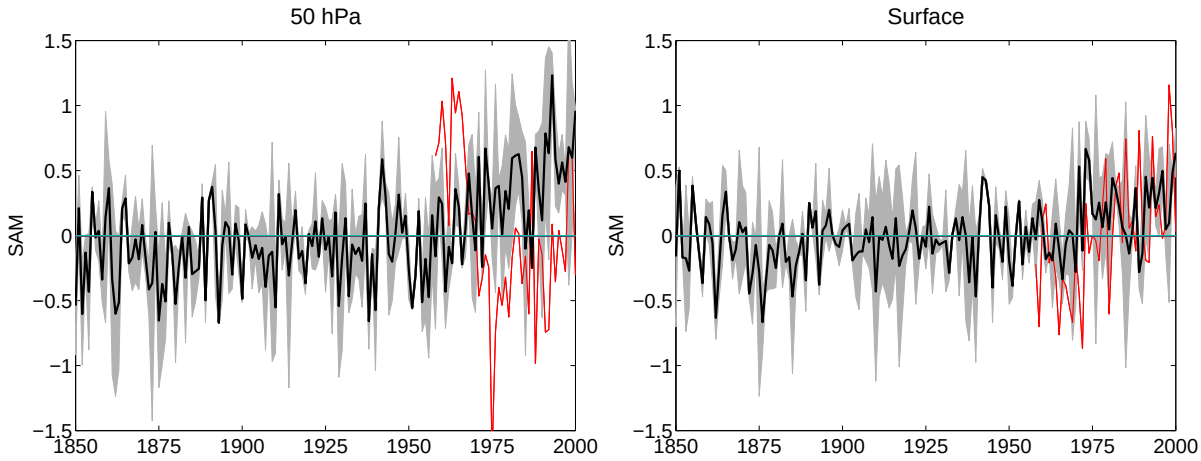

Figure A2: Time series of annual SAM at 50 hPa (right panel) and at the surface (right panel) based on monthly anomalies from the full time series mean as simulated by the MPI-ESM (black line is ensemble mean, grey shading indicates one standard deviation among the runs) and in the ERA-40 reanalysis (red line). Indices are calculated using the EOF-based version.

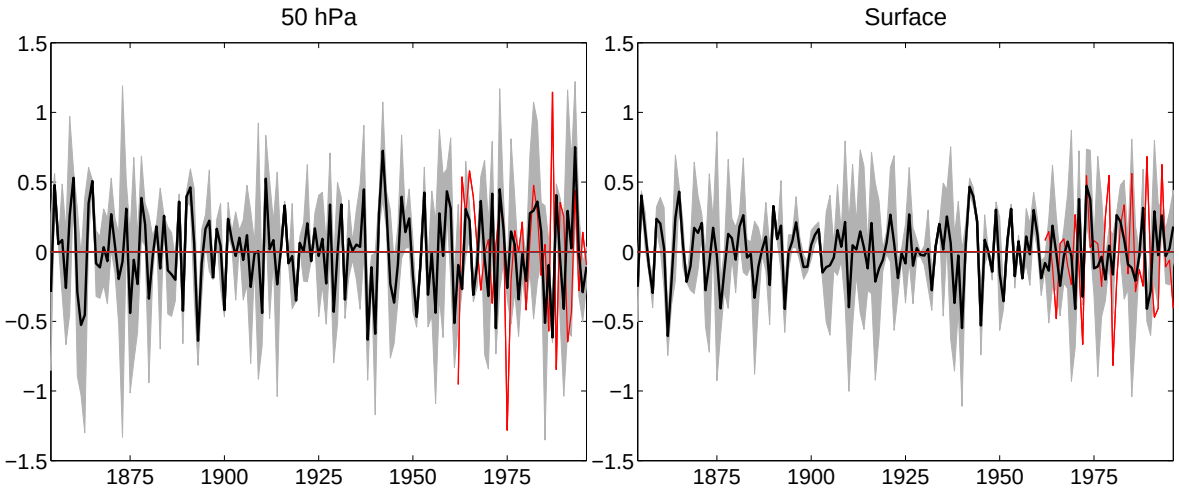

Figure A3: As figure A2 based on anomalies that exclude long-term trends

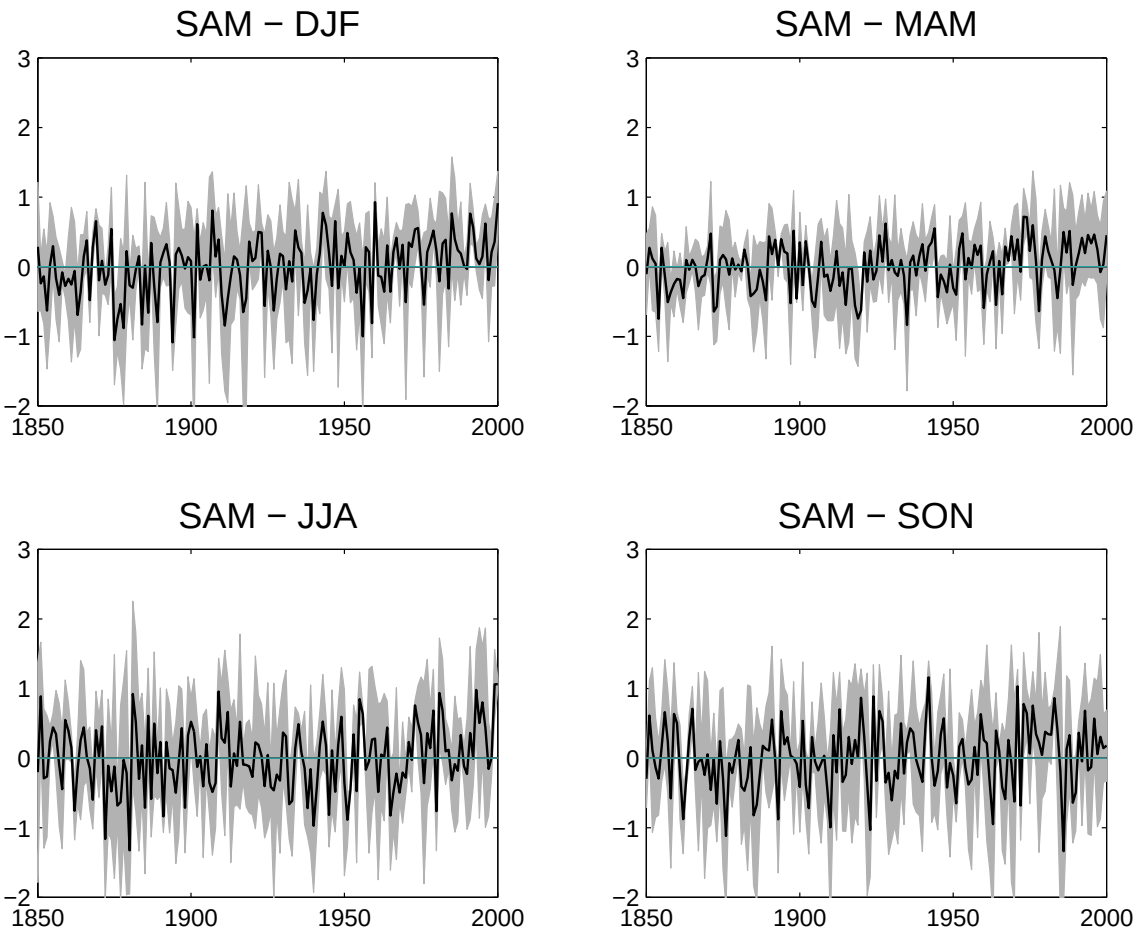

Figure A4: Time series of SAM at the surface in the 4 seasons based on monthly anomalies from the full time series mean as simulated by the MPI-ESM CMIP5 historical experiment (black line is ensemble mean, grey shading indicates one standard deviation among the runs). Indices are calculated using the EOF-based version.

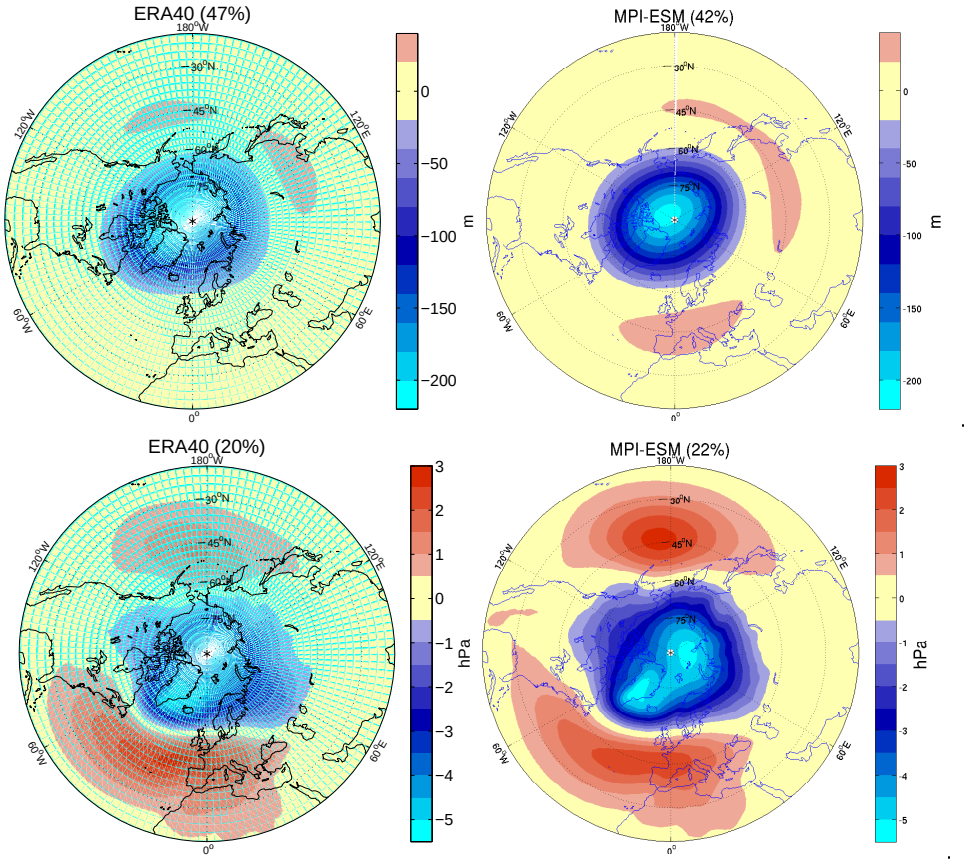

Figure A5: First EOF pattern of monthly mean SLP anomalies (hPa) in the lower levels and of monthly GPH anomalies at 50 hPa (m) in the upper levels between 20°N and 90°N. Left panels show the ERA-40 pattern (1958 to 2000), right panels the ensemble mean pattern of the MPI-ESM CMIP5 historical experiment data (1850 to 2000) based on anomalies that include long-term trends. The EOFs are scaled so that the associated PC has unit variance over this period.

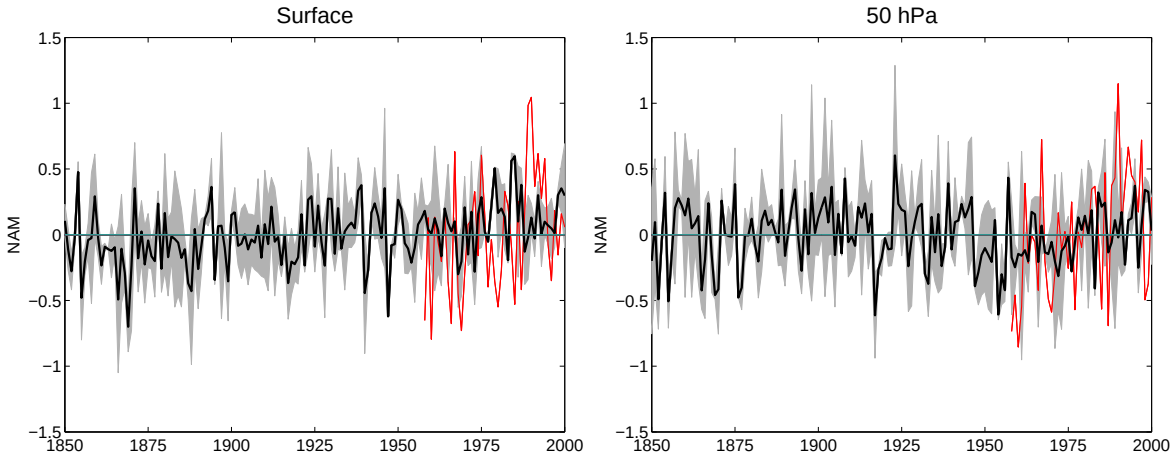

Figure A6: Time series of annual surface NAM(left panel) and NAM at 50 hPa (right panel) based on monthly anomalies that include long-term trends as simulated by the MPI-ESM (black line is ensemble mean, grey shading indicates one standard deviation among the runs) and in the ERA-40 reanalysis (red line). Indices are calculated using the EOF-based version.

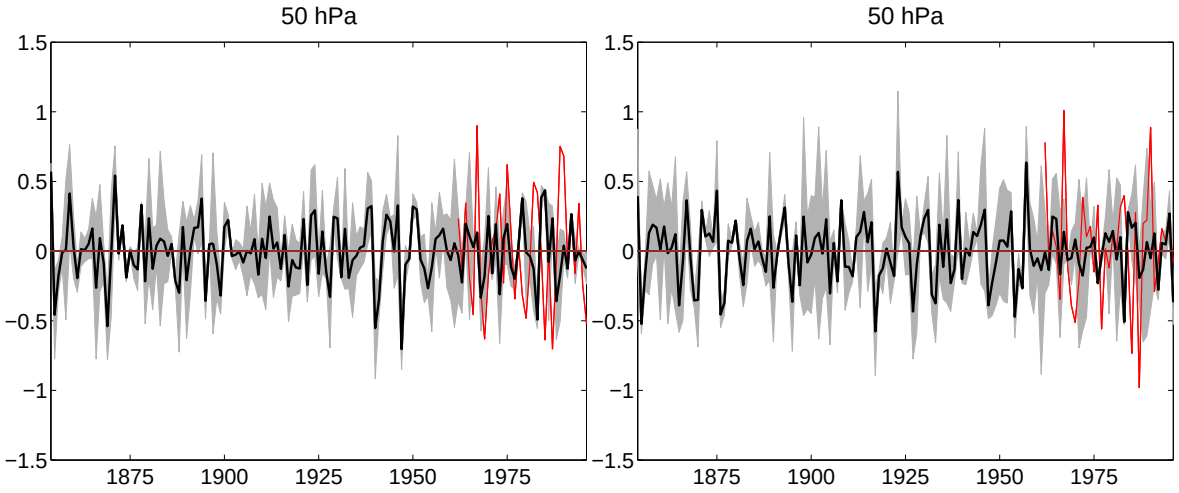

Figure A7: As figure A6 based on anomalies that exclude long-term trends

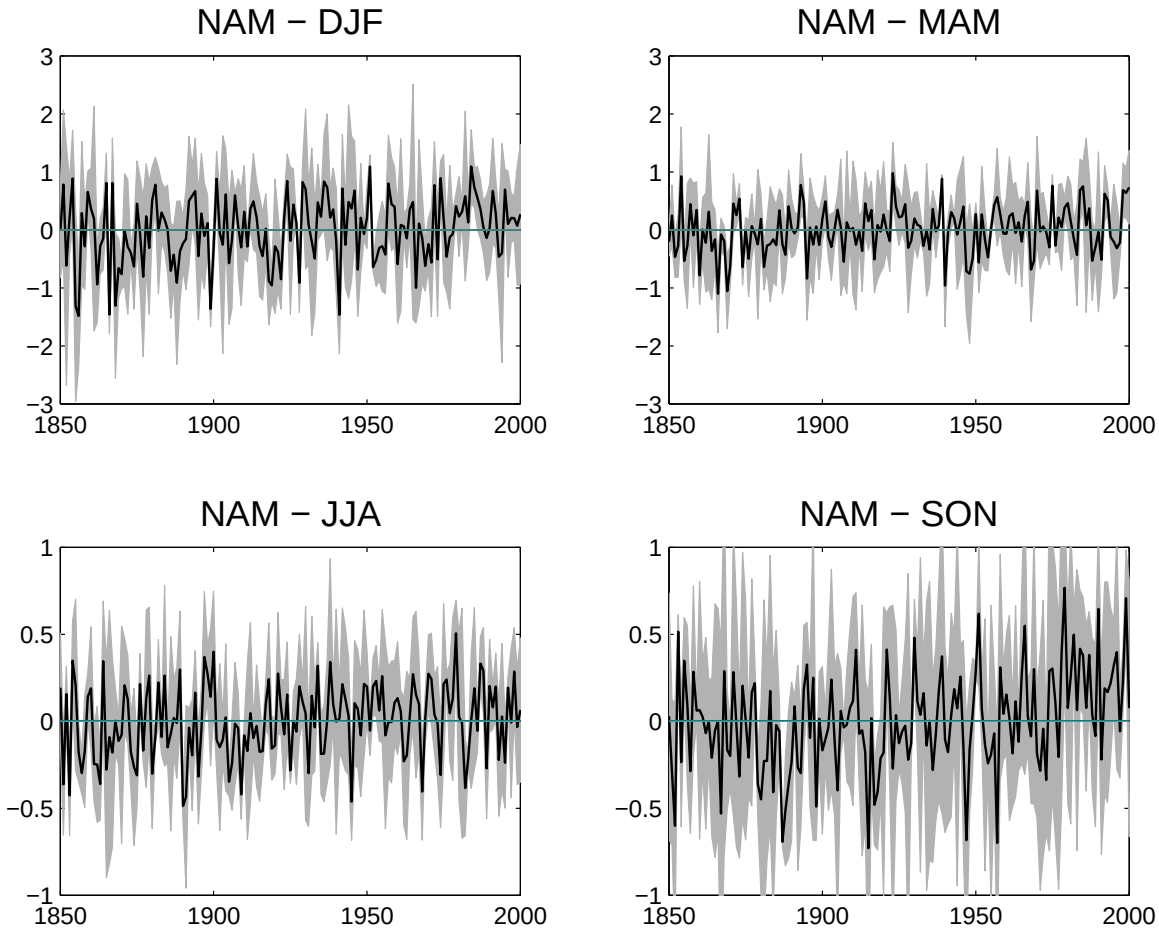

Figure A8: As figure A4, for the surface NAM

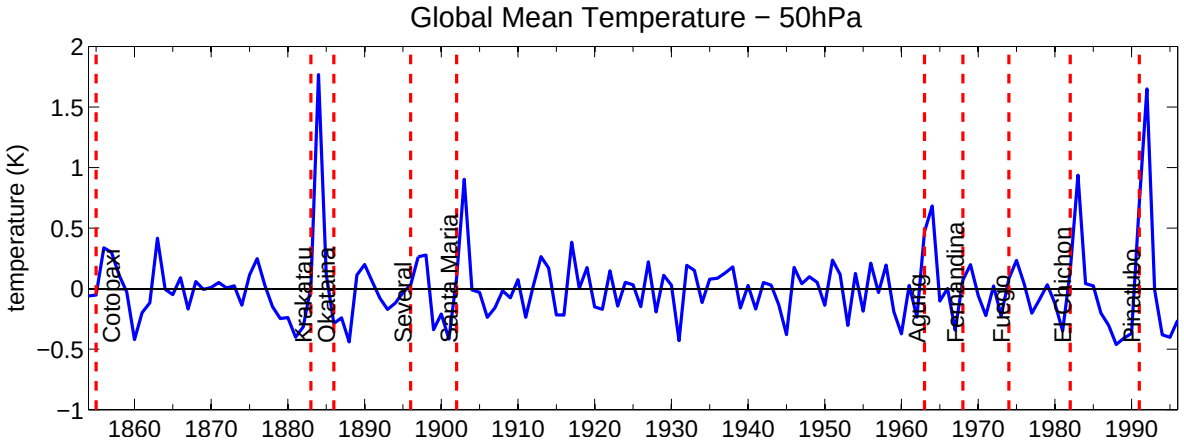

Figure A9: Annual mean global temperature anomalies at 50 hPa from 1854 to 1996 in the MPI-ESM CMIP5 historical experiment. Anomalies are calculated excluding long-term trend.

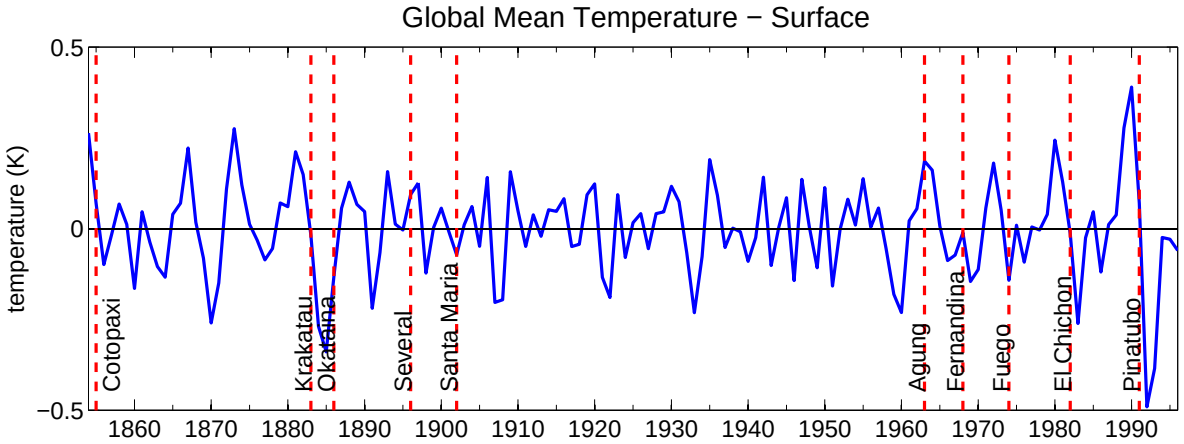

Figure A10: Annual mean global surface temperature anomalies from 1854 to 1996 in the MPI-ESM CMIP5 historical experiment. Anomalies are calculated excluding long-term trend.

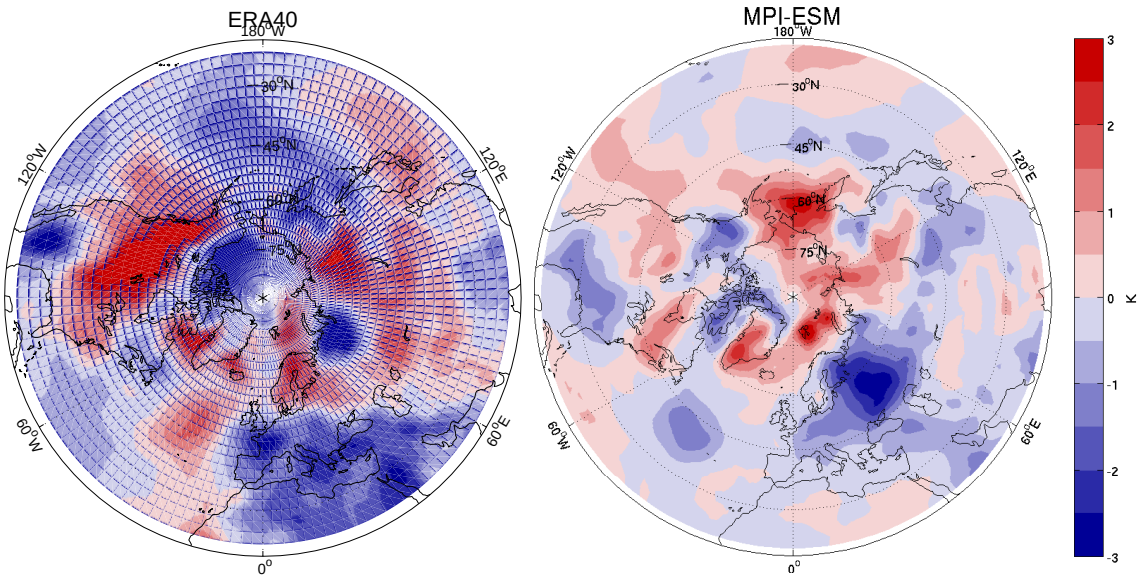

Figure A11: NH surface temperature anomalies in winter (DJF) of 1991/1992 in the ERA-40 reanalysis (lleft panel) and the MPI-ESM CMIP5 historical experiment simulations' ensemble mean (right panel). Anomalies are calculated excluding long-term trends.

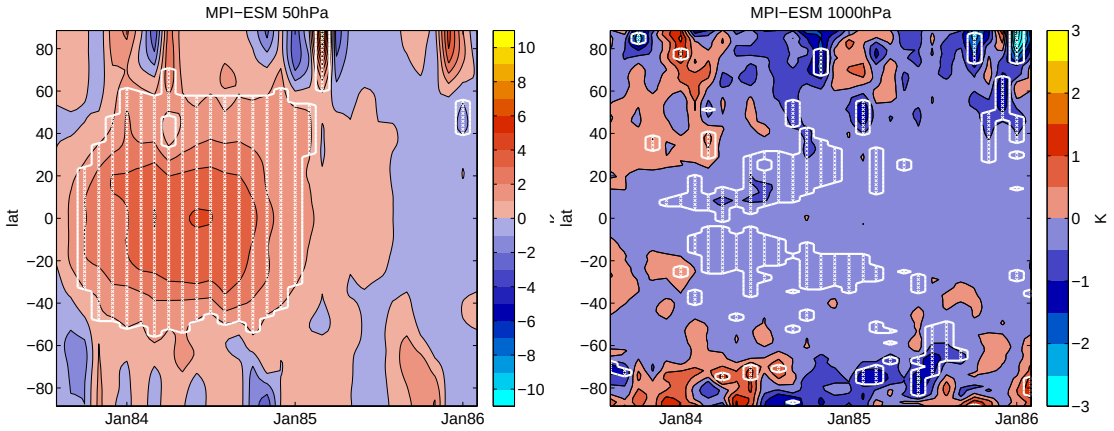

Figure A12: Monthly zonal mean temperature anomalies (K) at 50 hPa (left panel) and 1000 hPa (right panel) in the cmip5 runs in the 2.5 years following the eruption of Krakatau. Grey hatching marks anomalies larger than 2 standard deviations (significant on 95% level).

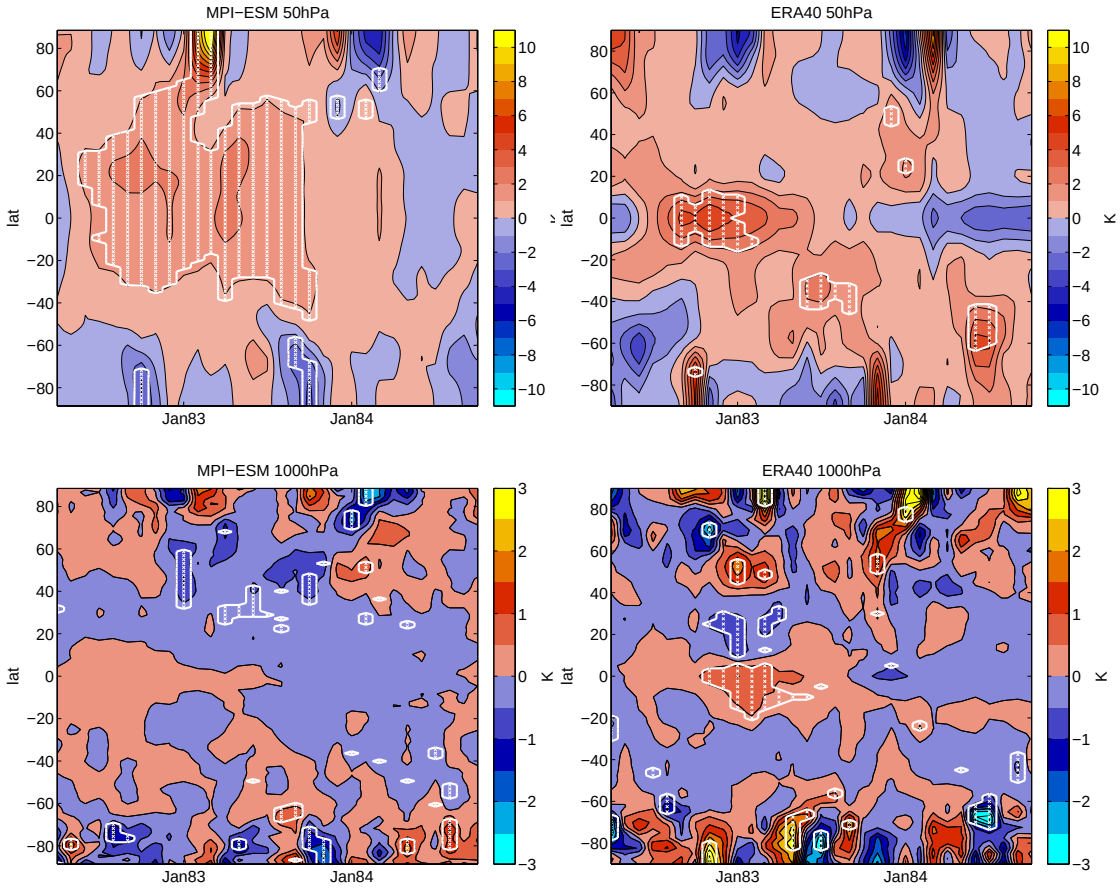

Figure A13: As figure 4.15 for the 2.5 years following the eruption of El Chichon.

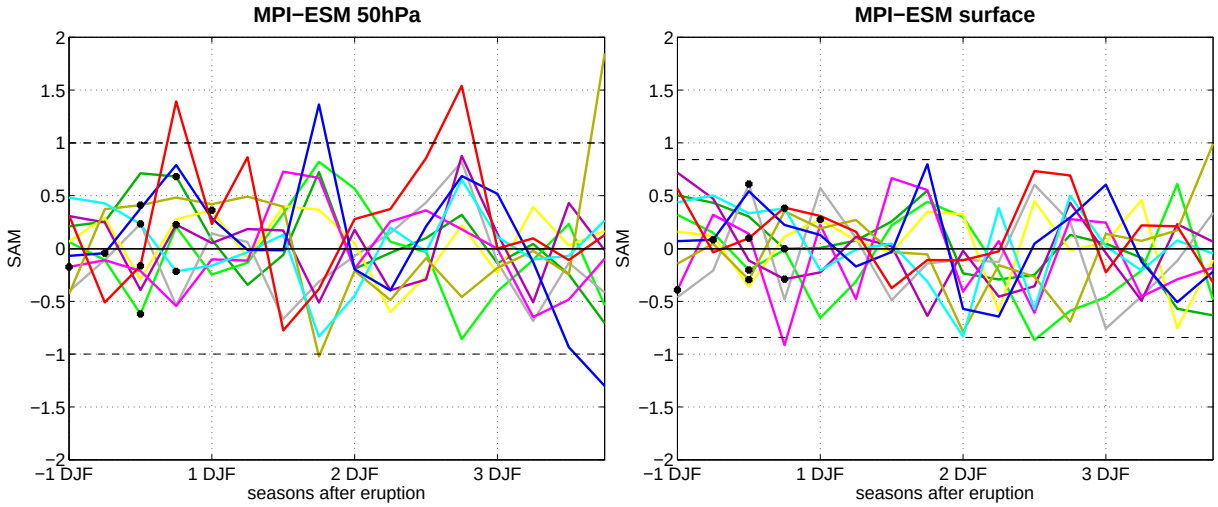

Figure A14: Seasonal SAM index at 50 hPa (left panel) and at the surface (right panel) in the three years following 10 volcanic eruptions in the MPI-ESM historical simulation ensemble mean. Index is calculated with EOF-analysis and is based on anomalies that do not include long-term trends.

Appendix B

Stratosphere-Troposphere Coupling

To examine a possible downward coupling from the stratosphere to the troposphere in the MPI-ESM in regard of the volcanic signal in the SH circulation, a daily SAM index in the first year following the eruption of Mount Pinatubo is examined. Since the computing time for the EOF-analysis with daily data is very high, a alternative index is used, the Antarctic Oscillation index (AOI) by Gong and Wang (1999). At the surface this index is highly correlated with the EOF-based SAM index, making use of the anti-correlation between the mid-latitude high pressure band and the sub-polar low pressure areas. Figure B1 shows their correlation analysis for the zonally averaged SLP of the different latitudes. The highest anti-correlation is found between 40°S and 60°S-70°S with a significant (99% confidence level) correlation coefficient of -0.59. Based on this analysis, Gong and Wang (1999) defined the AOI as the difference between the normalized, zonally averaged pressure anomalies P* at 40°S and 65°S:

$$AOI = P^*_{40^\circ\mathrm{S}} - P^*_{65^\circ\mathrm{S}} \tag{B.1}$$

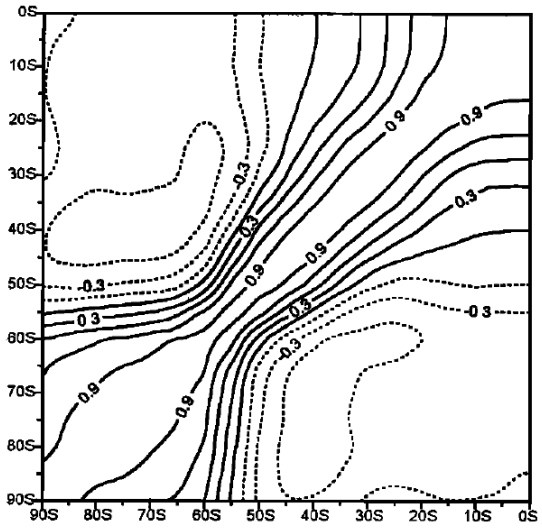

Figure B1: Correlation coefficients among zonally mean sea level pressure in the SH, from Gong and Wang (1999).

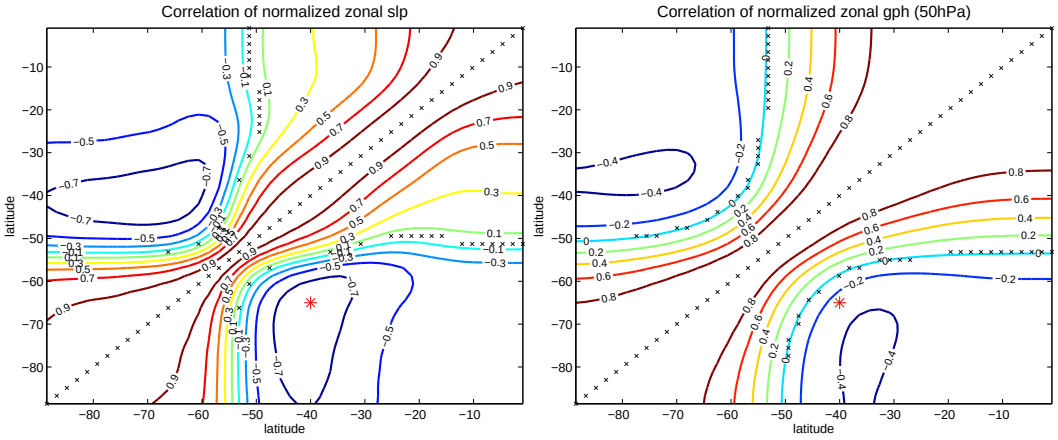

Figure B2: Correlation among zonal mean SLP anomalies (left panel) and GPH anomalies at 50 hPa (right panel) in MPI-ESM CMIP5 historical runs, monthly anomalies are calculated following equation (3.3). Grey crosses mark the values that are not significant on a 99% level.

To ensure the applicability of the AOI definition by Gong and Wang (1999), their correlation analysis was conducted with the MPI-ESM output, using Pearson's linear correlation coefficient. Although the Gong and Wang index is only used for the calculation of the daily AOI index, the correlation analysis is conducted here with monthly data for better comparison with the results of Gong and Wang (1999). The significance of the correlations has been calculated using a standard t-test. All correlation coefficients that differ from 0 have been found to be significant on a 99% confidence level. At the surface (figure B2, left panel) the anti-correlation of zonally averaged SLP anomalies is highest between the latitude of approximately 40 °S and latitudes from roughly 60°S to 85°S. Therefore, the differences of the SLP anomalies between 40°S and 65°S (red star), used by Gong and Wang (1999) to define their index and where correlation in the MPI-ESM exceeds -0.7, are suitable to define the surface AOI index. Figure B2 shows the same correlation analysis for GPH at 50 hPa. The anti-correlation of zonal mean GPH anomalies in this layer is generally lower (maximal anti-correlation of -0.44). The latitudes most anti-correlated with the polar cap are shifted equator-ward in comparison to the surface. Maximal negative correlation of more than -0.4 is found between latitudes of approximately 35-40 °S and 70-90 °S. This is in agreement with the results of the EOF analysis. In the surface EOF pattern the anti-correlation between SLP at 45°S and higher latitudes is represented by the regions of opposite sign in variability (figure 4.8, lower right panel). At 50 hPa the anti-correlated circumpolar pattern is very weak, but the pattern of polar cap GPH variability is more extended towards the equator, decreasing the anti-correlation between 45 °S and higher latitudes (figure 4.8, upper right panel). Therefore the latitudes chosen by Gong and Wang (1999) for their surface index only exhibit a correlation coefficient of -0.28 using the GPH MPI-ESM data at 50 hPa. Nevertheless, for consistency, these latitudes are kept the same for the calculation of the daily AOI indices throughout the whole troposphere and stratosphere.

Figure B3 shows the daily AOI in the first year following the eruption of Mount Pinatubo as simulated by the MPI-ESM as a function of calender day and pressure level between 1000 and 0.1 hPa. Striking are the strong positive daily AOI indices of up to 5 in October/November

of 1991 and April/May of 1992 in the upper stratosphere and lower mesosphere. The daily index at 50 hPa, where the significant positive monthyl SAM index was found, only reaches values below 3 and is just within the significance levels. These daily values suggest that the response to the eruption is strongest near the stratopause. The significance of those positive AOI anomalies does not extend to levels below 50 hPa. Instead the significant signal covers mesospheric levels. One would expect the strongest vertical gradient of the positive AOI signals near the tropopause, but the intense weakening already takes place in the lower stratosphere. In general there is no obvious decoupling of tropospheric and stratospheric variability near the tropopause layer.

This increase of the AOI index with altitude in spring of 1991, as found in the MPI-ESM results, might not be due to a strong signal in greater heights, but be a product of the index definition. While the chosen latitudes of 40°S and 65°S have been shown to be very good indicators of the extra-tropical pressure see-saw at the surface in the MPI-ESM simulations, already at 50 hPa the anti-correlation of the zonally averaged GPH at these latitudes is low. To test the correlation at higher levels, the correlation analysis by Gong and Wang (1999) was applied to the simulated monthly mean GPH at 1 hPa (figure B4). It becomes clear that there is no anti-correlation between any latitudes at 1 hPa. It seems that changes in GPH are a vertical movement of this layer spanning the whole hemisphere. Therefore the Gong and Wang index is not suited to describe a SAM-like circulation variability in the upper stratosphere.

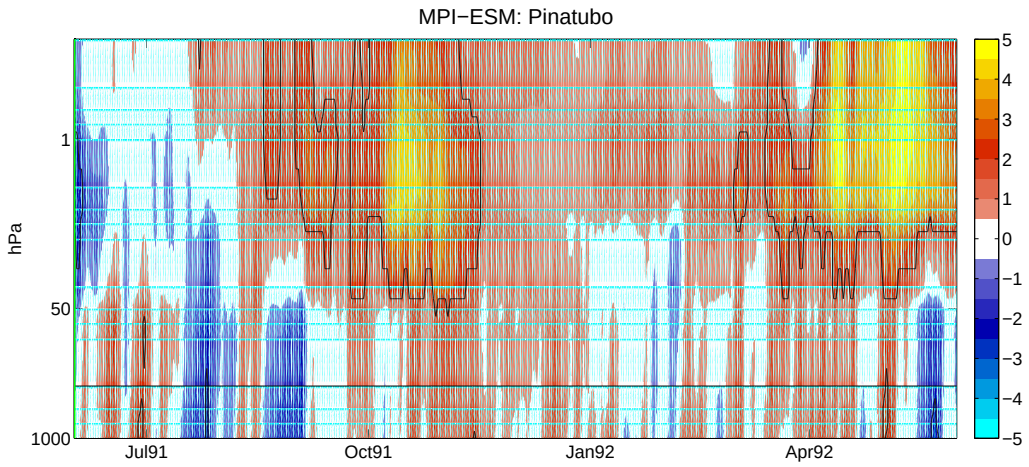

Figure B3: Daily AOI index in the first year after the eruption of Mount Pinatubo in June 1991 between 1000 and 0.1 hPa following the definition of Gong and Wang as simulated by the MPI-ESM CMIP5 historical experiment runs. The ensemble mean is shown and black line indicates approximate height of the tropopause.

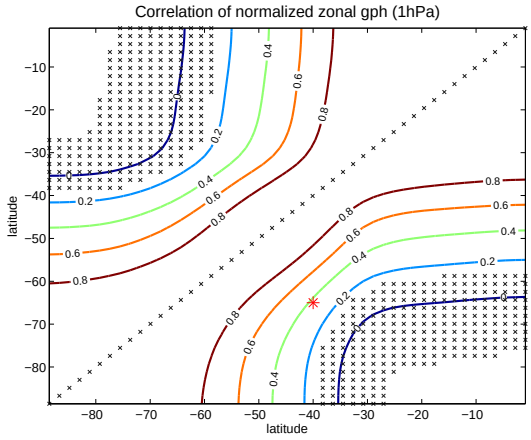

Figure B4: Correlation among zonal mean GPH anomalies at 1 hPa in MPI-ESM CMIP5 historical runs, anomalies are calculated following equation (3.3). Grey crosses mark the values that are not significant on a 99% level.